Observational constraints on upper tropospheric NO_x emissions, lifetime, and oxidative products

By

Benjamin Albert Nault

A dissertation submitted in partial satisfaction of the

requirements for the degree of

Doctor of Philosophy

in

Earth and Planetary Sciences

in the

Graduate Division

of the

University of California, Berkeley

Committee in charge:

Professor Ronald C. Cohen, Chair
Professor Inez Y. Fung
Professor Allen H. Goldstein

Fall 2015

Observational constraints on upper tropospheric NO_x emissions, lifetime, and oxidation products

by

Benjamin Albert Nault

Abstract

Observational constraints on upper tropospheric NO_x emissions, lifetime, and oxidation products

by

Benjamin Albert Nault

Doctor of Philosophy in Earth and Planetary Sciences

University of California, Berkeley

Professor Ronald C. Cohen, Chair

Nitrogen oxides ($NO_x \equiv NO + NO_2$) regulate tropospheric ozone (O_3) production rates. In the upper troposphere (~8 – 15 km above ground level), where O_3 is an important greenhouse gas, there are few detailed measurements of NO_x and its oxidation products. As a result, the chemical reactions that involve NO_x are poorly characterized under the low temperature conditions in this region of the atmosphere. For the reactions that have been studied under these conditions (e.g., daytime nitric acid, or HNO_3, and pernitric acid, or HO_2NO_2, production), the results from various experiments indicate a 20 – 50% disagreement for the rate constants, and the other important NO_x oxidation reactions (production of acyl peroxy nitrate, like PAN and PPN, and alkyl and multifunctional nitrates) have not been well characterized for the conditions characteristic of the upper troposphere. Besides the poorly understood NO_x oxidation rates, recent calculations have indicated there is an important upper tropospheric NO_x oxidation product (methyl peroxy nitrate, or $CH_3O_2NO_2$) that has not been measured in the atmosphere. These uncertainties in the products and oxidation rate constants affect the characterization of the input of NO_x from lightning.

In this dissertation, I report observations obtained during two airborne field campaigns, the Deep Convective Clouds and Chemistry (DC3, May – June, 2012) and the Studies of Emissions and Atmospheric Composition, Clouds, and Climate Coupling by Regional Surveys (SEAC4RS, August – September, 2013) experiments, and use these observations to investigate the reaction products and rate constants for the oxidation of NO_x to less reactive reservoirs. The observations focused on fresh lightning emissions in deep convective outflow, and the subsequent chemical aging of the outflow downwind.

First, I present the first ambient observations of $CH_3O_2NO_2$, and recommendations on how to measure upper tropospheric *in situ* NO_2 with minimal interferences from the thermal decomposition of $CH_3O_2NO_2$ during sampling. I show that $CH_3O_2NO_2$ is ubiquitous in the upper troposphere and is as important NO_x oxidative product as HNO_3. Then, using observations from one quasi-Lagrangian flight during DC3, I derive constraints on the daytime NO_x oxidative rate constants for the reactions that remove upper tropospheric NO_x. The reactions include the production of $CH_3O_2NO_2$, HO_2NO_2, PAN, PPN, alkyl and multifunctional nitrates, and HNO_3.

These constraints indicate that NO_x lifetime is longer than currently believe due to the daytime HNO_3 and HO_2NO_2 production rate constants being 30 – 50% slower than currently assumed. Finally, the implications of the longer lifetime are used to show that lightning NO_x emission rates are at least 33% larger than current estimates. As a consequence, model predictions indicate O_3 in the upper troposphere increase by 5 – 10% with a resulting increase in radiative forcing.

Table of Contents

List of Tables ..... **iv**

List of Figures ..... **v**

Acknowledgements ..... **xi**

Chapter 1. Introduction **1**

1.1 Sources of upper tropospheric NO_x 1

1.2 Production of upper tropospheric O_3 2

1.3 Sinks of upper tropospheric NO_x 3

1.4 Analysis of upper tropospheric NO_x chemistry 4

Chapter 2. Measurements of $CH_3O_2NO_2$ in the Upper Troposphere **6**

2.1 Introduction 6

2.2 Thermal-dissociation laser-induced fluorescence detection of $CH_3O_2NO_2$ 7

2.2.1 Thermal-dissociation laser-induced fluorescence 7

2.2.2 NO_2 measurements free of non-acyl peroxy nitrate interference 8

2.2.3 Inlet configurations and effects on NO_2 and $CH_3O_2NO_2$ measurements 9

2.2.4 Accuracy, uncertainty and limit of detection for $CH_3O_2NO_2$ 9

2.3 Ambient measurements of $CH_3O_2NO_2$ 10

2.3.1 Characterization of the measurements of ambient $CH_3O_2NO_2$ 10

2.3.2 Examples of measurements of $CH_3O_2NO_2$ 11

2.4 Discussion 13

2.5 Conclusion 14

Chapter 3. Observational Constraints on the Oxidation of NO_x in the Upper Troposphere **29**

3.1 Introduction 29

3.2 Instrumentation 31

3.3 Results 32

3.4 Analysis 34
3.4.1 Nitric acid production 34
3.4.2 Speciated peroxy nitrate production 34
3.4.3 Alkyl and multifunctional nitrate production 35
3.5 Atmospheric Implications 36
3.6 Conclusions 37

Chapter 4. Impacts of Updated Upper Tropospheric NO_x Chemistry on Lightning NO_x Emission Rates 51
4.1 Introduction 51
4.2 Methods 52
4.2.1 Model Description 52
4.2.2 Airborne Observations 53
4.2.3 Satellite Observations 54
4.3 Sensitivity in modeled NO_2 and HNO_3 from lightning emissions 54
4.3.1 Changes in NO_2 column densities 54
4.3.2 Changes in upper tropospheric HNO_3 mixing ratios 55
4.3.3 Changes in other regions of the world 55
4.4 Implications for lightning NO_x emission rates 56
4.4.1 Comparison to upper tropospheric observations during DC3 56
4.4.2 Comparisons to satellite observations 58
4.4.3 Impacts of shorter NO_x lifetime on direct lightning NO_x observations 58
4.4.4 Impacts on O_3 59
4.5 Conclusions 59

Chapter 5. Conclusions 72

References 75

Appendix A. Observational Constraints on the Oxidation of NO_x in the Upper Troposphere 90
A.1 Measurement Intercomparisons 90

A.2 Calculation of Alkyl and Multifunctional Nitrate 90
A.3 Calculation of Alkyl and Multifunctional Nitrate in Aerosol-Phase 91
A.4 Description of GEOS-Chem Model 91

List of Tables

Table 2.1. Lengths for tubing in the corresponding sections for Figure 2.3. *15*

Table 2.2. Reactions and rates used in calculating dissociations in instrument and photostationary steady state calculations for $CH_3O_2NO_2$. *16*

Table 2.3. Measurements used in this analysis and calculations of the lifetimes in Figure 2.1. *17*

Table 3.1. Measurements used in this analysis to calculate rate constants, peroxy radical concentrations, average α, and ΣANs production rate. *38*

Table 3.2. Calculated and recommended rate constants (±2σ uncertainty) for speciated peroxy nitrates at T = 225 K and P = 230 hPa. *39*

Table 4.1. Description of the different chemical sensitivity cases used in this study. *61*

Table 4.2. Coordinates of the different regions used in this study. *62*

Table 4.3. Percent biases of the NO_2 column density from the averaged OMNO2d and DOMINO product over South America, Northern Africa, Southern Africa, and Southeast Asia during their respective summer months (June – August for Northern Africa and Southeast Asia and December – February for South America and Southern Africa). The Cases are defined in Table 4.1. The percent mean bias is calculated as (observations – Case 5)/observations × 100. *63*

Table A1. Reactions and rate constants at T = 225 K and P = 230 hPa used to calculate PAN production rate and $CH_3C(O)O_2$ concentrations. *92*

Table A2 Reactions and rate constants used to calculate PPN production rate and $C_2H_5C(O)O_2$ concentrations. *93*

Table A3. Reactions and rate constants used to calculate $CH_3O_2NO_2$ production rate and CH_3O_2 concentrations. *94*

Table A4. Species, rate constants, average α, and classification used to calculate alkyl nitrate production (E2 in Chapter 3 and Fig. 3.8b) at T = 225 K and P = 230 hPa. *95*

Table A5. Species, corrected vapor pressure (atm), percent of gas–phase condensing onto the aerosol particle, and percent contribution of each species to the total calculated $\Sigma ANs_{(p)}$. The vapor pressure is calculated using SIMPOL.1 (Pankow and Asher, 2008) and divided by 3 (Leungsakul et al., 2005; Fry et al., 2009; Fry et al., 2011). *97*

List of Figures

Figure 2.1. Calculated mean total lifetime profile of $CH_3O_2NO_2$ (blue) and HO_2NO_2 (green) for typical conditions observed during DC3 in the daytime. The total lifetime is calculated using observed OH, photolysis rates, and temperatures along with the rate constants listed in Table 2.2. The black line is marks the region where the non-acyl peroxy nitrates have a lifetime longer than 1 hour. *18*

Figure 2.2. Calculated fraction of **(a)** $CH_3O_2NO_2$ and **(b)** HO_2NO_2 dissociated at residence times of 2.0 s (blue), 0.5 s (red) and 0.1 s (black) and cabin temperatures ranging from 275-310K. The calculations are for ambient pressures of 230 hPa and ambient temperatures of ~225 K. **(c)** XNO_2 ($XNO_2 = NO_2$ + fraction dissociated $CH_3O_2NO_2$ and fraction dissociated HO_2NO_2) as a function of the residence times and cabin temperatures used in **(a)** and **(b)**. We use the median mixing ratios of NO_2 (200 pptv), $CH_3O_2NO_2$ (90 pptv), and HO_2NO_2 (40 pptv) observed between 220 and 230 K during DC3. *19*

Figure 2.3. Schematic of the TD-LIF inlet sampling manifold. Arrows and letters refer to lengths referenced in Table 2.1. The species measured in each channel is shown at the right, where ΣPNs ≡ PAN + PPN + $CH_3O_2NO_2$ + HO_2NO_2 + … and ΣANs ≡ the sum of gas and aerosol alkyl and multifunctional nitrates. *20*

Figure 2.4. The calculated fractional decomposition of $CH_3O_2NO_2$ (blue) and HO_2NO_2 (green) as a function of $CH_3O_2NO_2$ oven temperatures at a pressure of 230 hPa and a residence time of 0.08 s. The black line marks the target temperature (~60°C) for optimal separation of $CH_3O_2NO_2$ and HO_2NO_2. Rates used to calculate the fraction decomposition are shown in Table 2.2. *21*

Figure 2.5. Schematic of the species measured in the TD-LIF channels and the temperature set points (temperatures the species dissociate) for those channels. ΣPNs ≡ PAN + PPN + $CH_3O_2NO_2$ + HO_2NO_2 + … and ΣANs ≡ alkyl and multifunctional nitrates. The channel subtracted to calculate the measured species (e.g., $CH_3O_2NO_2$) is shown before the equals sign in the third column. *22*

Figure 2.6. Five minute averaged time series of **(a)** NO_2 (blue) and $CH_3O_2NO_2$ (black) channel and **(b)** temperature from a flight on 17 June 2012 during DC3. The local time was approximately midafternoon during this time segment. *23*

Figure 2.7. Five minute averaged time series of **(a)** uncorrected (black) and corrected (magenta) $CH_3O_2NO_2$ for HO_2NO_2 thermal decomposition, **(b)** HO_2NO_2, and **(c)** pressure altitude (blue) and temperature (green) from a flight on 30 May 2012 during DC3. Local sunset is approximately 00:00 UTC. *24*

Figure 2.8. $CH_3O_2NO_2$ inferred ($\Delta CH_3O_2NO_2$) as the difference of the total peroxy nitrates minus PAN, PPN, and HO_2NO_2 compared to $CH_3O_2NO_2$ observed by TD-LIF at temperatures between 220 and 230 K. The red line is a weighted fit to the data: slope of 0.93 (±0.07) and intercept of −33.0(±5.9) pptv. The uncertainties used in the calculations are ±40% + 20 pptv for

$CH_3O_2NO_2$, ±15% + 20 pptv for ΣPNs, ±15% + 2 pptv for PAN, ±20% + 1 pptv for PPN, and ±30% + 1 pptv for HO_2NO_2. The R^2 of the fit is 0.3. *25*

Figure 2.9. Five minute averaged time series of the chemical evolution of $CH_3O_2NO_2$ downwind from convection from a flight on 21 June 2012 during DC3. The x-axis shows the age of the air parcel that the DC-8 started sampling at approximately 12:00 UTC (0 hr), which was the local sunrise. *26*

Figure 2.10. The median profile of **(a)** NO_2, **(b)** $CH_3O_2NO_2$, **(c)** $CH_3O_2NO_2/(NO_2 + CH_3O_2NO_2)$, and **(d)** temperature for ARCTAS-A (blue), DC3 (black), and SEAC4RS (dark grey). The red line in **(b)** is the median limit of detection for S/N = 2, 60 s for DC3. The green line in **(c)** is the median $CH_3O_2NO_2/(NO_2 + CH_3O_2NO_2)$ in background air where NO_x/NO_y is less than 0.2 during DC3. *27*

Figure 2.11. Binned modeled versus measured $CH_3O_2NO_2$. The bars identify the interquartile of the modeled $CH_3O_2NO_2$. The blue line has a slope of 1 for reference. *28*

Figure 3.1. Daytime NO_x fate in the upper troposphere. Reactions or channels that are not NO_x sinks (e.g., R2a) are not included. Double arrows indicate important thermal decomposition reactions that occur in the upper troposphere. Arrows and compounds in red (black) indicate reactions and products with NO (NO_2), and the blue arrow and reactants (products) in the bracket correspond to all the products. The lifetime for conversion back NO_x in the upper troposphere by photolysis and reactions with OH is days for all species except HO_2NO_2 and HOONO. For these two species, the lifetime is hours in the upper troposphere. *40*

Figure 3.2. Portions of the NASA DC-8 flight path (blue) used to calculate all the rate constants. The wind direction and relative speed observed on the DC-8 for the 21 June 2012 flight is shown as red arrows. The edge of the cloud that marks time equals 0 for the Lagrangian observations is shown as the green dashed-dot line. Leg 1, 2, and 3 corresponds to the left most, center, and right most flight tracks. Red arrow and black horizontal line corresponds to 25 m/s wind speed and 88 km distance, respectively. *41*

Figure 3.3. Time series of **(a)** NO and NO_2, **(b)** ΣPNs_i, **(c)** $\Sigma ANs_{(g+p)}$, and **(d)** $HNO_{3(g+p)}$, where $\Sigma PNs_i = CH_3O_2NO_2 + HO_2NO_2 + PAN + PPN$ and $HNO_{3(g+p)}$ is the average of the IC and CIMS data. Note, NO_2 is blue and the left y-axis and NO is green and the right y-axis in **(a)**. Measurements not shown between 14:30 and 15:10 UTC are when the DC-8 sampled air outside the Lagragian parcel. The vertical red lines correspond to the beginning of Legs 1, 2, and 3 in Figure 3.2. *42*

Figure 3.4. First order loss rate of ethene. The solid red line is the slope (-9.6×10^{-5} s^{-1}) and the dashed-dot red line is the 2σ uncertainty ($\pm1.4\times10^{-5}$ s^{-1}). *43*

Figure 3.5. The observed $HNO_{3(g+p)}$ production rate (molecules/cm^3/s) versus NO_2 (molecules/cm^3). The solid red line is the slope (6.2×10^{-5} s^{-1}) and the dashed-dot line is the 2σ uncertainty ($\pm2.0\times10^{-5}$ s^{-1}). *44*

Figure 3.6. Comparison of k_{1a} rate constant at T = 225 K and M = 7.3×10^{18} molecules/cm^3 from Sander et al. (2011), Atkinson et al. (2004), Henderson et al. (2012) and this study (red). The range shows the 2σ uncertainty of the product of the rate constant and branching ratio for HNO_3 formation. *45*

Figure 3.7. The observed **(a)** PAN, **(b)** PPN, **(c)** $CH_3O_2NO_2$, and **(d)** HO_2NO_2 production rate (molecules/cm^3/s) versus NO_2 (molecules/cm^3). The solid red line is the slope and the dashed-dot red lines are the 2σ uncertainty. The slopes are **(a)** $4.5(\pm1.0)\times10^{-5}$ s^{-1}, **(b)** $6.8(\pm1.2)\times10^{-6}$ s^{-1}, **(c)** $8.4(\pm4.8)\times10^{-5}$ s^{-1}, and **(d)** $3.4(\pm1.8)\times10^{-5}$ s^{-1}. For **(c)**, three minute averages are used to reduce the noise of the measurements. *46*

Figure 3.8. (a) The observed O_3 versus $\Sigma ANs_{(g+p)}$ during the flight. The slope (2σ uncertainty) is 25(±6). **(b)** The calculated cumulative production of alkyl and multifunctional nitrates (area plot in pptv) and the 15 minute average (±1σ of the mean) measured production (red error bars in pptv). *47*

Figure 3.9. The observed (black at ambient T and P) and calculated (blue) cumulative production of the $\Sigma ANs_{(p)}$. The observations are 15 minute averages (±1σ of the spread) and the p_{vap} is reduced by a factor of 3. *48*

Figure 3.10. Comparison of the NO_x lifetime (NO_x lifetime = NO_x/Loss of NO_z) in the upper troposphere (T ≤ 230 K) from a steady state model during the entire DC3 campaign. The base case uses the recommended rate constants from Sander et al. (2011) and the updated chemistry case uses the rate constants from Henderson et al. (2012) and Bacak et al. (2011). The slope (±1σ) is 1.20(±0.01). *49*

Figure 3.11. The absolute annual mean change in **(a)** NO_x, **(b)** HO_2, **(c)** OH, **(d)** O_3, **(e)** HNO_3, **(f)** PAN, **(g)** HO_2NO_2, and **(h)** $CH_3O_2NO_2$ in the upper troposphere (200 – 400 hPa). The mean change is calculated as (updated chemistry case – base case). Values above the tropopause are removed. Note the different scales for the color bars. *50*

Figure 4.1. Changes in modeled NO_2 column density ($\times10^{14}$ molec./cm^2, first row) and upper tropospheric HNO_3 mixing ratios (pptv, second row) between Case 1 and Case 2 (first column), Case 3 (second column) and Case 4 (third column). Description of each case is found in Table 4.1. Note the differences in scale for each figure. *64*

Figure 4.2. Changes in modeled NO_2 column density ($\times10^{14}$ molec./cm^2) between Case 1 and Case 4 for Northern Africa, Southeastern Asia, Southern Africa, and South America. The changes correspond to the months June through August for Northern Africa and Southeastern Asia and December through February for Southern Africa and South America. Description of each case is found in Table 4.1 and definitions of the regions are found in Table 4.2. Note the differences in scale for each figure. *65*

Figure 4.3. Changes in modeled upper tropospheric HNO_3 mixing ratios (pptv) between Case 1 and Case 4 for Northern Africa, Southeastern Asia, Southern Africa, and South America. The changes correspond to the months June through August for Northern Africa and Southeastern

Asia and December through February for Southern Africa and South America. Description of each case is found in Table 4.1 and definitions of the regions are found in Table 4.2. Note the differences in scale for each figure. *66*

Figure 4.4. Comparison between modeled and measured ratio of upper tropospheric **(a)** NO_x and **(b)** HNO_3. Values reported from Hudman et al. (2007) and Martini et al. (2011) are shown in dark grey as comparison to the values from Case 1 (black), Case 4 (red) and Case 5 (blue). Description of the cases is found in Table 4.1. The light grey dashed-dot line in **(b)** represents the upper 1σ of observations during DC3. Note, the measured NO_x and HNO_3 from Hudman et al. (2007) and Martini et al. (2011) are adjusted as recommended by Browne et al. (2011) and Bertram et al. (2007), respectively, assuming the upper limit that 35% of the NO_2 signal is thermally decomposed $CH_3O_2NO_2$. *67*

Figure 4.5. Relative frequency of NO_x/HNO_3 ratios observed during DC3 (grey bars) and calculated in Case 1 (black line), Case 4 (red line) and Case 5 (blue line) models. *68*

Figure 4.6. Mean binned scatter plot of instantaneous 1 hr HNO_3 production rate (pptv/s) from modeled N_2O_5 hydrolysis (black) and modeled reaction of OH with NO_2 (red) versus the modeled-to-measured ratio from DC3 observations. The bars represent 1σ standard deviation about the mean of the production. A hydrolysis rate of 4×10^{-5} s^{-1} (Evans and Jacob, 2005) is assumed, and the slower OH and NO_2 rate constant (Henderson et al., 2012) is used. The R^2 for the grey (N_2O_5 hydrolysis) and red (OH with NO_2 reaction) is 0.23 and 0.02, respectively. *69*

Figure 4.7. Comparison between modeled and observed O_3 during DC3 **(a)**. Modeled annually averaged percent in upper tropospheric (350 hPa – tropopause) O_3 concentration, by region, between Case 1 and Case 5, where percent change is (Case 5 – Case 1)/Case 1 × 100. *70*

Figure 4.8. Binned mean observed (black) and modeled (blue) upper tropospheric (200 – 350 hPa) versus relative age of air mass (NO_x/HNO_3). *71*

Figure A1. Intercomparison of **(a)** DC-8 versus GV HO_2NO_2, **(b)** ΣPNs_i (ΣPNs_i = $CH_3O_2NO_2$ + HO_2NO_2 + PAN + PPN) versus ΣPNs, and **(c)** IC $HNO_{3(p+g)}$ versus CIMS $HNO_{3(g)}$. The slopes (±1σ), intercepts (±1σ), and R^2 values are **(a)** 0.66(±0.01), −3(±1), and 0.96, **(b)** 0.96(±0.02), 7(±9), and 0.68, and **(c)** 1.09(±0.02), 34(±2), and 0.81. *99*

Figure A2. Intercomparison of photostationary steady state (PSS) NO_2 versus measured NO_2. The slope (±1σ), intercept (±1σ), and R^2 is 0.99(±0.01), −12(±2), and 0.89. *100*

Figure A3. The full flight path of the NASA DC-8 is shown in black for the entire 21 June 2012 experiment. Wind direction and relative speed observed on the DC-8 is shown by the red arrows. *101*

Figure A4. Time series of **(a)** $CH_3O_2NO_2$, **(b)** HO_2NO_2, **(c)** PAN, and **(d)** PPN. The red vertical lines indicate the start of legs 1, 2, and 3, respectively in Fig. 3.2. The $CH_3O_2NO_2$ observations are three minute averages and the values. *102*

Figure A5. First order loss rate of **(a)** toluene and **(b)** ethyne. The solid red line is the slope (-1.01×10^{-4} and -5.9×10^{-6} s^{-1} for toluene and ethyne, respectively) and the dashed-dot red line is the 2σ uncertainty ($\pm2.3\times10^{-5}$ and $\pm2.6\times10^{-6}$ s^{-1} for toluene and ethyne, respectively). *103*

Dedicated in loving memory to my mom, Susan Kreigh,

and my step-father, Terry Kreigh, who both passed away too early.

Wished you could have been part of this and future journeys.

Acknowledgements

First, I would like to thank my advisor, Ronald Cohen, for his mentorship, support, advice, and guidance. He allowed me intellectual freedom in the topics I research while still pushing me to find the new and exciting story and discovery. With his guidance, I have achieved significant growth intellectually, scientifically, and how I communicate as a scientist within the community and to broader audiences. Thank you for everything and never giving up.

I appreciate all of the discussions and advice from my qualifying exam and dissertation committees. Thank you, Inez Fung, David Shuster, and Allen Goldstein, for assisting me with explaining how my work fits into the big picture and the discussions about how to present myself and my work for my future endeavors.

Also, I would like to thank the group members that assisted me in learning how to operate the instrument and to analyze the data from the two airborne campaigns I participated in and use in this dissertation: Paul Wooldridge, Charity Garland, and Sally Pusede. I also want to thank Sally for her guidance during my second and third years as I was preparing for my qualifying exam and my first paper submission.

The support from prior and current Cohen Research Group members has been greatly appreciated. Thanks for being my sounding board, coffee breaks, and support system. Also, Josh Laughner, thanks for being a model whiz. Finally, I want to thank the support of prior and current Earth and Planetary Science graduate students during my 4.5 years. The camping trip adventures and conversations will never be forgotten.

The assistance of the administrative staffs in Chemistry, especially Maria Rodriguez, Earth and Planetary Sciences, and NSF fellowship coordination office has been greatly valued and will never be overlooked.

This work could not have happened without the administrative work and ground and flight support of NASA. Also, I acknowledge and appreciate the observations, discussions, and comments from my many collaborators that made my research possible. Finally, without the planning and leadership from the science teams from the two campaigns, my work would not have been possible. Thanks.

My undergraduate and graduate school could not have been done without the support of my family, especially from my dad, Nat Nault, grandmother, Betty Lou Nault, mother-in-law, Kate Metiva, and father-in-law, Stan Metiva. Thank you always being there and the encouragement.

I owe the last 4.5 years to you, Vanessa Nault. Thank you for understanding when I needed to get work completed at home but at the same time realizing when you needed to pull me away from work. Also, thank you for the support, encouragement, and belief that I could complete this and the support for all my future endeavors.

Besides the collaborators mentioned at the beginning of each chapter, I would like to acknowledge the following people for allowing me to use their data for my research: in Chapter

2, Professor William H. Brune (Pennsylvania State University) for OH and HO_2 measurements, Professor L. Gregory Huey (Georgia Institute of Technology) for HO_2NO_2, PAN, and PPN measurements, Professor Paul O. Wennberg (California Institute of Technology) for HNO_3 measurements, and Dr. Thomas B. Ryerson (NOAA) for NO data; in Chapter 3, Joshua L. Laughner (University of California, Berkeley) for assistance in setting up and running the GEOS-Chem model, Professor Donald Blake (University of California, Irvine) for the hydrocarbon measurements, and Dr. Glenn Diskin (NASA) for the CH_4 measurements; and, in Chapter 4, Joshua L. Laughner (University of California, Berkeley) for assistance in GEOS-Chem and satellite analysis, Dr. Thomas B. Ryerson (NOAA) for NO and O_3 measurements, Professor Jack Dibb (University of New Hampshire) and Professor Paul O. Wennberg (California Institute of Technology) for HNO_3 measurements, Dr. Glenn Diskin (NASA) for H_2O measurements, and the free use of tropospheric NO_2 column data from the OMI sensor from www.temis.nl.

Finally, I gratefully acknowledge and appreciate the financial support from NASA grant NNX12AB79G and from the National Science Foundation Graduate Research Fellowship under grant number DGE 1106400.

Chapter 1. Introduction

Nitrogen, N_2, constitutes 78% of the atmosphere; however, it is a chemically inert gas. Oxidized forms of nitrogen (e.g, NO, NO_2, HNO_3, …) make up a relatively small fraction of the atmosphere (10 parts per trillion, or ppt, to 100 parts per billion, or ppb). Nitrogen oxide concentrations and the associated chemistry are strongly coupled to the production of ozone (O_3) and aerosols, both of which impact human, animal, and plant health (e.g., Monks et al., 2009; Myre et al., 2013). Oxidized nitrogen is generally emitted to the atmosphere as a result of combustion, microbial activity in soil, or lightning in the form of nitric oxide (NO). The majority, ~60%, of the emissions originate from anthropogenic activities (e.g., Schumann and Huntrieser, 2007). These emissions are concentrated in locations with high population densities. In remote regions, isolated from anthropogenic activities, the important sources of nitrogen oxides are natural.

In this dissertation, I focus on the chemistry and on the oxidation products of NO in one of these remote regions of the atmosphere, the upper troposphere. The upper troposphere is one of the coldest regions of Earth's atmosphere and, as a result, is a location with unique chemistry. The products of oxidation of NO include nitrogen dioxide (NO_2), peroxy nitrates (PNs, RO_2NO_2), alkyl and multifunctional nitrates (ANs, $RONO_2$), and nitric acid ($HONO_2$). Typically NO and NO_2 reaches a steady-state with each other on a time scale of 100 seconds. We commonly treat them as a family and refer to the two molecules collectively as NO_x. The sum of all odd-nitrogen molecules are referred to as NO_y, and the higher oxide components of NO_x are labelled NO_z, which can be defined as $NO_y - NO_x$.

The upper troposphere, 8 to 12 km above the Earth's surface, is a region of the atmosphere where temperatures are in the range 210 – 250 K and pressures are 200 – 400 hPa. In this region of the atmosphere, O_3 is an important greenhouse (e.g., Martini et al., 2011; Myre et al., 2013). Directly observing NO_x and its chemical oxidation products in this region is difficult. As a result, tests of our understanding of the chemistry in the region by comparison of model predictions that use laboratory measurements of the kinetics of NO_x as constraints have been inconclusive.

1.1 Sources of upper tropospheric NO_x

The major source of upper tropospheric NO_x include lightning, with secondary sources including transport from the stratosphere above (region of the atmosphere that is 12 to 50 km above ground level), by convection from below (e.g., thunderstorms), and by emissions from aircraft (e.g., Levy et al., 1999; Bertram et al., 2007; Schumann and Huntrieser, 2007; Liang et al., 2011). Lighting heats the surrounding air to temperatures greater than 2000 K, breaking the oxygen, O_2, molecular bonds to form atomic oxygen (O). Once the air has cooled to temperatures less than 2000 K, NO_x is produced by the reaction of O with N_2 (R1) or atomic N (from R1) with O_2 (R2; e.g., Goldenbaum and Dickerson, 1993; Lee et al., 1997).

(R1) $N_2 + O \rightleftharpoons NO + N$

(R2) $O_2 + N \rightleftharpoons NO + O$

Estimates of the rate of lightning NO_x production ranges from 2 to 8 Tg yr^{-1} (Schumann and Huntrieser, 2007). These ranges include uncertainties in the total global lightning flash rate and the flash energies as well as the production of NO_x per flash. Cloud to cloud and cloud to ground lightning are thought to behave differently, and there is evidence that storms at different latitudes produce NO_x at different rates—possibly due to the coupling of wind-shear to flash length (e.g., Schumann and Huntrieser, 2007). As an alternative to mechanistic estimates of lightning NO_x production, observations of NO_x in the upper troposphere have been used to constraints on the aggregate source at global or regional scales (e.g., Beirle et al., 2004; Hudman et al., 2007; Martin et al., 2007; Martini et al., 2011; Miyazaki et al., 2014). These estimates, generally, assume that our knowledge of the chemistry of the upper troposphere is perfect, or at least neglect to propagate that uncertainty into the uncertainty of lightning NO_x estimates (e.g., Stavrakou et al., 2013; Miyazaki et al., 2014). In the simplest terms, the lightning NO_x emission rate as estimate from NO_x concentrations can be described as being inversely proportional to the NO_x lifetime (e.g., Beirle et al., 2004). The NO_x lifetime accounts for the chemical and physical removal of the lightning NO_x prior to sampling (E1). Here, τ_{NO_x} represents the lifetime of NO_x.

(E1) $$Lightning\ NO_x\ Emission\ \propto \frac{\frac{[NO_x]}{\tau_{NO_x}}}{Lightning\ flash\ rate}$$

This approximation is applicable for regional scale lightning NO_x emission rates that are less than a day old (e.g., Beirle et al., 2004; Beirle et al., 2010). In one study that did take chemistry uncertainties into account, Miyazaki et al. (2014) estimated a 1 Tg yr^{-1} uncertainty (17%) in global lightning NO_x emission rates due to uncertainty in the NO_x lifetime.

1.2 Production of upper tropospheric O_3

The uncertainty associated with lighting NO_x has important impacts on the global burden of O_3 (e.g., Labrador et al., 2005). The coupling of NO_x to O_3 production occurs in the process of oxidation of organic molecules. In the upper troposphere, the source of these organic molecules, which includes methane, butane, and acetone, is the transport of surface air by deep convection (e.g., Bechara et al., 2010; Apel et al., 2012). During the day, the organics, represented here as RH, are oxidized by the hydroxyl radical (OH), forming organic peroxy radicals, $RO_2^{\bullet}$ (R3). When $RO_2^{\bullet}$ reacts with NO (R4a), NO_2 is produced. The reaction of the organic alkoxy radical, $RO^{\bullet}$, with O_2 (R5) leads to the production of the hydroperoxy radical, or $HO_2^{\bullet}$. $HO_2^{\bullet}$ also reacts with NO to form NO_2 (R6a). The two NO_2 molecules produced from this reaction sequence undergo photolysis (R7) to produce ground state oxygen atom, $O(^3P)$, and $O(^3P)$ reacts with O_2 to form O_3 (R8).

(R3) $RH + OH \xrightarrow{O_2} RO_2^{\bullet} + H_2O$

(R4a) $RO_2^{\bullet} + NO \rightarrow RO^{\bullet} + NO_2$

(R5) $RO^{\bullet} + O_2 \rightarrow RO + HO_2^{\bullet}$

(R6) $HO_2^{\bullet} + NO \rightarrow OH + NO_2$

(R7) $NO_2 \xrightarrow{h\nu} NO + O(^3P)$

(R8) $O(^3P) + O_2 + M \rightarrow O_3 + M$

Here, *M* represents any third body molecule (e.g., argon, N_2, or O_2). As concluded by Seltzer et al. (2015), upper tropospheric O_3 concentrations, and its radiative impact, are sensitive to the upper tropospheric NO_x lifetime. If the NO_x lifetime is longer (shorter) than currently assumed, then more (less) NO_x is available to produce O_3, and more (less) ozone is produced.

1.3 Sinks of upper tropospheric NO_x

The sinks of upper tropospheric NO_x include oxidation to PNs, ANs, and HNO_3 and transport to lower altitudes in the troposphere (e.g., Bertram et al., 2007; Fang et al., 2010; Henderson et al., 2011). For this dissertation, I focus only on the daytime chemical oxidation of NO_x. Nighttime processes can be summarized as follows: NO_2 reacts with O_3 to produce nitrate radical, $NO_3^\bullet$, which reacts with NO_2 to produce dinitrogen pentoxide, N_2O_5. N_2O_5 then hydrolyzes on aerosols to produce two HNO_3 molecules.

(R9) $NO_2 + O_3 \rightarrow NO_3^\bullet + O_2$
(R10) $NO_2 + NO_3^\bullet \rightarrow N_2O_5$
(R11) $N_2O_5 + H_2O \xrightarrow{\text{aerosol}} HNO_3$

In the daytime, PNs are produced as products of the oxidation of NO_2 by simple peroxy radicals, $RO_2^\bullet$ and $HO_2^\bullet$, or acyl peroxy radicals, $R(O)O_2^\bullet$ (R12 – R14); ANs are produced as a branch in the oxidation of NO to NO_2 by $RO_2^\bullet$ (R4b); and HNO_3 is produced through the oxidation of NO_2 by OH (R15).

(R12) $HO_2^\bullet + NO_2 + M \rightleftharpoons HO_2NO_2 + M$
(R13) $RO_2^\bullet + NO_2 + M \rightleftharpoons RO_2NO_2 + M$
(R14) $R(O)O_2^\bullet + NO_2 + M \rightarrow R(O)O_2NO_2 + M$
(R4b) $RO_2^\bullet + NO \rightarrow RONO_2$
(R15) $OH + NO_2 + M \rightarrow HONO_2 + M$

However, Henderson et al. (2011) concluded the representation of the chemical removal of NO_x in the upper troposphere is not consistent with observations, a problem that arises from the challenge of replicating upper tropospheric conditions in the laboratory. This misrepresentation of NO_x sinks in the atmosphere has led to a 30% NO_x under-prediction compared to observations (Henderson et al., 2011), indicating that the NO_x removal rate is too fast. This fast NO_x removal rate has important impacts on upper tropospheric O_3 chemistry (e.g., Seltzer et al., 2015), and lightning NO_x production rates (e.g., Stavrakou et al., 2013).

Once produced, the effect of these products depends on their lifetime before conversion back to NO_x. The shortest lived molecules are HO_2NO_2 and RO_2NO_2. Their lifetime is typically hours due to the weak molecular bond between NO_2 and the simple peroxy radical. The lifetime of HO_2NO_2 and its organic analogs is set by the thermal decomposition rate (the reverse of R12 and R13) and by photolysis (R16 – R17). HO_2NO_2 also reacts with OH at an appreciable rate (R18).

(R16) HO_2NO_2 ($CH_3O_2NO_2$) + $h\nu$ → $HO_2^{\bullet}$ ($CH_3O_2^{\bullet}$) + NO_2

(R17) HO_2NO_2 ($CH_3O_2NO_2$) + $h\nu$ → HO ($CH_3O^{\bullet}$) + NO_3

(R18) HO_2NO_2 + OH → H_2O + O_2 + NO_2

Several studies of HO_2NO_2 have clarified the role this molecule plays in the upper troposphere, identified that it photolyzes in the near-infrared through an unusual (for the atmosphere) overtone absorption mechanism, and established that current models and observations are in disagreement by about a factor of 2 for the concentration of HO_2NO_2 in the upper troposphere (e.g., Jaeglé et al., 2001; Murphy et al., 2004; Hudman et al., 2007; Kim et al., 2007). Prior to my dissertation (Chapters 2 and 3), there were no direct measurements of any RO_2NO_2 molecule in the atmosphere. The presence of methyl peroxy nitrate ($CH_3O_2NO_2$), the most important RO_2NO_2 in the atmosphere, was inferred from observations of total PNs in a pioneering study by Murphy et al. (2004). Subsequently, Browne et al. (2011) established the presence of $CH_3O_2NO_2$ by analysis of the temperature dependence of an apparent interference in the measurement of NO_2. Such interferences have plagued measurements of NO_2 for decades (see Bradshaw et al., 1999 or Davis et al., 1993) without a clear explanation for their cause.

The acyl PNs, ANs, and HNO_3 have longer chemical lifetimes of weeks to months. As a result, the transport and rainout is the main path for removal of these molecules from the upper troposphere. Chemical reactions of NO_z include photolysis and oxidation by OH to produce NO_x, or partitioning to aerosols or cloud droplets (e.g., Jacob et al., 1996; Marmo et al., 2014). The residence time of air masses remaining in the upper troposphere is less than 10 days (e.g., Bertram et al., 2007).

1.4 Analysis of upper tropospheric NO_x chemistry

To improve our understanding of upper tropospheric NO_x chemistry, I designed and built an instrument for measuring $CH_3O_2NO_2$ and measured $CH_3O_2NO_2$ and a wide suite of other nitrogen oxides as part of two airborne field campaigns that focused on the chemistry of the upper troposphere: the Deep Convective Clouds and Chemistry (DC3, May – June 2012) and Studies of Emissions and Atmospheric Composition, Clouds and Climate Coupling by Regional Surveys (SEAC4RS, August – September 2013). Both studies occurred over the continental United States to enable sampling of air where the effects of lightning and convection were large.

In Chapter 2, I describe instrument modifications that enabled the first direct measurements of $CH_3O_2NO_2$, and evaluate their effectiveness using measurements from the DC3 experiment. I then describe the role of $CH_3O_2NO_2$ in the chemistry of the upper troposphere over the continental United States.

In Chapter 3, I target a comprehensive test of our understanding of the kinetics of NO_x oxidation. I use observations downwind of a mesoscale convective system. In the cloud, all soluble species are removed by rain and large emissions of NO_x are created by lightning. Consequently, we have an observational definition of time zero as the time when air exits the cloud and oxidation of NO_x begins. The NASA DC-8 followed this air mass in a quasi-Lagrangian fashion enabling direct inference of the oxidation rate of NO_x and the production rate of each of the higher oxides. I characterize the daytime rates for conversion of NO_x to HO_2NO_2, $CH_3O_2NO_2$, and acyl peroxy

nitrates, to the sum of alkyl and multifunctional nitrates, and to HNO_3. I find that the HNO_3 and HO_2NO_2 production rates are ~30 – 50% lower than currently expected while the other rate are consistent with expectations to within ±30%. Also, I evaluate the potential for HNO_3 production from the reaction of HO_2 with NO (e.g., Butkovskaya et al., 2005; Butkovskaya et al., 2007) to affect the chemistry of the upper troposphere. I show that to be consistent with measurements, if this reaction takes place, it must be accompanied by a slower rate for the production of HNO_3 from the reaction of OH with NO_2. Finally, I show that decreasing HNO_3 and HO_2NO_2 kinetic rate constants, which increases the NO_x lifetime, increases upper tropospheric O_3 mixing ratios.

In Chapter 4, I build on the previous chapters to assess our understanding of lightning NO_x emission rates. Compared to a model without $CH_3O_2NO_2$ chemistry and with fast HNO_3 production rate constant, a model with $CH_3O_2NO_2$ chemistry (Chapter 2) and with a slower HNO_3 production rate (Chapter 3) has decreased upper tropospheric HNO_3 and increased upper tropospheric NO_x and O_3 mixing ratios. The NO_2 column density, a quantity observed from space instruments, such as OMI, is also larger in the revised model. The revised model is more consistent with observations, including *in situ* and space-based observations of HNO_3 and measurements of the ratio of HNO_3 to NO_2. The lightning NO_x emissions that are consistent with observations are 33% larger than in the reference model.

In Chapter 5, I propose future directions for research, including measurements of $CH_3O_2NO_2$ to investigate its seasonal and diurnal behavior and additional measurements that would aid in our understanding of upper tropospheric HNO_3.

Chapter 2. Measurements of $CH_3O_2NO_2$ in the Upper Troposphere

Adapted from Nault, B. A., Garland, C., Pusede, S. E., Wooldridge, P. J., Ullmann, K., Hall, S. R., and Cohen, R. C., Atmos. Meas. Tech., 8, 987–997, 2015.

2.1 Introduction

Methyl peroxy nitrate ($CH_3O_2NO_2$) is predicted to be abundant at temperatures below 240 K (Figure 2.1), where it serves a temporary reservoir of NO_x (NO_x = NO + NO_2). $CH_3O_2NO_2$ can be transported on regional scales moving NO_x from source to receptor regions and thus affecting O_3, OH, and other chemistry of the upper troposphere. The emphasis on low temperatures results from non-acyl peroxy nitrates, such as $CH_3O_2NO_2$ and pernitric acid (HO_2NO_2), having lower thermal stability and shorter lifetimes than acyl peroxy nitrates, such as peroxy acetyl nitrate (PAN) and peroxy proionyl nitrate (PPN) (~100 kJ/mol for non-acyl peroxy nitrates versus ~120 kJ/mol for acyl peroxy nitrates).

The low thermal stability of $CH_3O_2NO_2$ poses analytical challenges. At room temperature, $CH_3O_2NO_2$'s lifetime is shorter than a second (Figure 2.1). If the air sample is brought into a warm aircraft prior to detection, this very short lifetime results in substantial decomposition for residence times longer than even 0.1 s (Figure 2.2). As a result of the decomposition of $CH_3O_2NO_2$, there is also a positive interference to NO_2 measurements with residence times at warm temperatures longer than 0.1 s. For NO_2 measurements, the interference was quantified to be as much as 43% during a study over Canada in springtime (Browne et al., 2011). Thus, in addition to interest in measurement of $CH_3O_2NO_2$, it is essential to understand $CH_3O_2NO_2$ to correct NO_2 measurements for its presence. Alternatively, in the absence of such a correction, it is necessary to interpret NO_2 measurements as XNO_2, where XNO_2 is the sum of ambient NO_2 and some or all of non-acyl peroxy nitrates (Browne et al., 2011).

There have been no prior direct measurements of ambient $CH_3O_2NO_2$. The only *in situ* information about $CH_3O_2NO_2$ stems from indirect measurements of the sum of $CH_3O_2NO_2$ and HO_2NO_2 by calculating the difference between total peroxy nitrate measurements and measurements of PAN and PPN (Murphy et al., 2004) and analysis of temperature dependent deviations of NO_2 observations from photostationary state (e.g., Browne et al., 2011). Murphy et al. (2004) showed that the sum of non-acyl peroxy nitrates contribute a large fraction of the NO_y budget (10 – 22%) in aged air masses. However, the individual contributions from $CH_3O_2NO_2$ and HO_2NO_2 were only identified modeling the sum. Browne et al. (2011) calculated that $CH_3O_2NO_2$ mixing ratios of ~25 pptv should be expected; however, their calculations along flight tracks were limited to air samples at photostationary steady state.

Using the limited observational inferences as a guide, Browne et al. (2011) added $CH_3O_2NO_2$ chemistry to a global chemical transport model (GEOS-Chem) and used the model to explore the role of $CH_3O_2NO_2$ in the upper troposphere (T ~210 – 250 K), allowing study of conditions that do not reach steady-state. They found that $CH_3O_2NO_2$ chemistry reduced NO_x mixing ratios with measureable effects on O_3, HNO_3, OH, and HO_2. They showed that $CH_3O_2NO_2$ mixing ratios peak in the summer due to more rapid photochemistry, and that biomass burning or deep

convection can increase $CH_3O_2NO_2$ mixing ratios by a factor of ~3 over mean atmospheric mixing ratios.

Following on these studies demonstrating an understanding of $CH_3O_2NO_2$ is important, we developed new configurations of the UC Berkeley thermal-dissociation laser-induced fluorescence (TD-LIF) instrument inlet aimed at unambiguous measurements of NO_2 and $CH_3O_2NO_2$. In this paper, we describe the design and performance of a modified inlet for the TD-LIF instrument, provide recommendations for minimizing and eliminating $CH_3O_2NO_2$ interferences to NO_2, and present observations of $CH_3O_2NO_2$ from DC3 and SEAC4RS. These measurements are the first *in situ* measurements providing specific information about atmospheric $CH_3O_2NO_2$.

2.2 Thermal-dissociation laser-induced fluorescence detection of $CH_3O_2NO_2$

2.2.1 Thermal-dissociation laser-induced fluorescence

The TD-LIF instrument has been described previously (Thornton et al., 2000; Day et al., 2002; Wooldridge et al., 2010). Briefly, NO_2 is measured by laser-induced fluorescence (Thornton et al., 2000) with supersonic expansion (Cleary et al., 2002). A 7 kHz, Q-switched, frequency doubled Nd:Yag laser pumps a tunable dye laser producing ~20 ns pulses at 585 nm and a bandwidth of 0.06 cm^{-1}. The dye laser is tuned on (9 s) and off (3 s) an isolated rovibronic feature of the jet-cooled NO_2 at 585 nm. The ratio between the peak and background NO_2 fluorescence is 10:1 sampling from an ambient pressure of 1 atm. The laser light is focused through two multipass White cells. Red-shifted fluorescence (wavelengths greater than 700 nm) of excited NO_2 is detected at a right angle to the excitation using a red sensitive photomultiplier tube (Hamamatsu H7421-50). Scattered light is minimized using time-gated detection and dielectric band pass filters that block light at wavelengths less than 700 nm. Fluorescence counts are collected at 4 Hz and reported as one second averages. For these measurements, calibrations were performed at least every hour during a level flight leg or after a significant change in altitude using a 4.67 (±0.26) ppmv NO_2 standard (Praxair) diluted to ~2 – 8 ppbv in zero air. The accuracy and stability of this reference gas was compared against a library of other NO_2 standards in our laboratory. Measurements of zero were obtained with similar frequency. Fluorescence quenching by water vapor is accounted for (Thornton et al., 2000) using diode laser hygrometer (DLH) measurements of H_2O (Diskin et al., 2002).

The TD-LIF instrument samples ambient air using a large flow carried through a 35 mm i.d. tube from the undisturbed free stream either by ram pressure from a partially plugged shroud at the inlet tip (ARCTAS, DC3), or carried through a 16 mm i.d. tube by a 120 liter/minute sample pump (SEAC4RS). The core of that flow was subsampled by a short (~ 0.10 m long) tube where air had a residence time of ~0.03 s and then split into multiple sample lines for detection of specific categories of NO_y (Figure 2.3). For $CH_3O_2NO_2$ detection, the sample is passed directly through a heated quartz tube (internal diameter ~ 4.3 mm, T ≈ 60°C) for 0.06 – 0.08 s followed by PFA tubing (i.d. ~3.2 mm) to one of two NO_2 detection cells. The residence time between the heater and the detector was ~0.4 – 0.5 s. The temperature (~60°C) for the heated quartz was chosen by calculating the temperature that would maximize the amount of $CH_3O_2NO_2$ dissociated while minimizing the amount of HO_2NO_2 dissociated (Figure 2.4). This also ensures

that PAN and its analogs (e.g., PPN) did not dissociate in the $CH_3O_2NO_2$ channel. Dinitrogen pentoxide (N_2O_5) has similar thermodynamics to HO_2NO_2 at this temperature (Wooldridge et al., 2010); however, the typical N_2O_5 mixing ratio during the day is estimated to be small due to slow rates of production at night under the low temperature conditions favorable to the presence of $CH_3O_2NO_2$.

The lower maximum temperatures of the $CH_3O_2NO_2$ and sum of peroxy nitrates (ΣPNs) heaters compared to the sum of alkyl and multifunctional nitrates (ΣANs) heaters (Figure 2.5) allow for a simpler construction, as described in Wooldridge et al., 2010). Instead of bare nichrome wire, commercial woven fiberglass insulated heating cables are used, and thermocouples are fastened directly to the quartz tubes. The very small amount of heat required to bring the sample streams to 60°C (~ 1 W for $CH_3O_2NO_2$, as calculated from the air heat capacity and mass flow rates) means that neither the maximum heater power (50 W across the 0.175 m heated length for $CH_3O_2NO_2$ dissociation) or the quartz tube thermal resistance are limiting factors that would cause the thermocouple measurement to differ significantly from the internal gas temperature. Additionally, using the constant wall temperature approximation (e.g., Kliner et al., 1997; references therein), we calculate thermal equilibration lengths of 0.01 – 0.02 m for $CH_3O_2NO_2$, which are short compared to the overall heated lengths (0.175 m).

Mixing ratios of ambient $CH_3O_2NO_2$ are determined by subtracting the measurements from the NO_2 channel from the $CH_3O_2NO_2$ channel (60°C, Figure 2.5). Similarly, the mixing ratio of ambient sum of peroxy nitrates (ΣPNs = PAN + PPN + $CH_3O_2NO_2$ + HO_2NO_2 + …) is determined by subtracting the measurements from the NO_2 channel from the ΣPNs channel, and the mixing ratio of ambient sum of alkyl and multifunctional nitrates (ΣANs) is determined by subtracting the measurements from the ΣPNs channel from the ΣANs channel (Figure 2.5). The HNO_3 channel depicted in Figure 2.5 has been employed in other TD-LIF deployments, but was not part of the DC3 and SEAC4RS configuration.

2.2.2 NO_2 measurements free of non-acyl peroxy nitrate interference

Measuring NO_2 free of $CH_3O_2NO_2$ interference is desirable for understanding upper tropospheric chemistry and essential to correctly derive the $CH_3O_2NO_2$ and ΣPNs mixing ratios from the heated channels (Figure 2.5). Measurements of NO_2 at ambient temperatures lower than 240 K, where non-acyl peroxy nitrates are more abundant due to longer thermal lifetimes (Figure 2.1), are not free of interferences if the sample residence time in the aircraft is long (Browne et al., 2011). Figure 2.2 shows the calculated fraction of $CH_3O_2NO_2$ and HO_2NO_2 thermally dissociating in the NO_2 inlet prior to measuring NO_2 for different residence times and as a function of cabin temperature. At a cabin temperature of 300 K, approximately 90^{+5}_{-10}%, 40^{+11}_{-6}% and 10^{+3}_{-2}% of $CH_3O_2NO_2$ and approximately 8±2%, 2%, and less than 1% of HO_2NO_2 will thermally decompose at residence times of 2 s, 0.5 s, and 0.1 s, respectively. The uncertainties are based on the 2σ range reported for the decomposition rates of $CH_3O_2NO_2$ and HO_2NO_2. The partial thermal decomposition of $CH_3O_2NO_2$ and HO_2NO_2 can cause up to 50% increase in the measured NO_2 (XNO_2) versus the ambient NO_2 (Figure 2.2c).

2.2.3 Inlet configurations and effects on NO_2 and $CH_3O_2NO_2$ measurements

Figure 2.3 shows the schematic of the TD-LIF inlet. Table 2.1 lists the lengths and residence times of the different inlets used in three recent experiments: ARCTAS, DC3, and SEAC4RS. The residence time is set by the measured length of tubing, the diameter of the tubing, and the flow speed of the sample pumps. Unless stated otherwise, the tubing has an internal diameter of ~3.2 mm. Following the recommendations of Wooldridge et al. (2010) and Browne et al. (2011), we shortened the residence time for the NO_2 sample from 0.85 s during ARCTASto 0.5 s during DC3 reducing the decomposition of $CH_3O_2NO_2$ in the NO_2 channel from ~90% to ~45%.

To reduce the residence time further during SEAC4RS, a bypass pump was used to bring a large flow of ambient air through a 1 m, 15.9 mm id tubing (Section A). We then reduced the length of Section C (Figure 2.3, Table 2.1). The combined effects of these changes reduced the maximum residence time for NO_2 from 0.5 s (DC3) to 0.23 s (SEAC4RS). This reduced the factional thermal dissociation of $CH_3O_2NO_2$ in the NO_2 channel to ~22%.

We obtain an NO_2 measurement by correcting for the partial thermal dissociation of $CH_3O_2NO_2$ in the XNO_2 channel (E1). The $CH_3O_2NO_2$ measurement is then determined by subtracting the corrected NO_2 and the fraction of thermally dissociated HO_2NO_2 in the $CH_3O_2NO_{2,CHANNEL}$ (E2) from the total signal in that channel.

(E1) $$NO_2 = XNO_2 - f_1 \times CH_3O_2NO_2$$

(E2) $$CH_3O_2NO_2 = CH_3O_2NO_{2,CHANNEL} - NO_2 - f_2 \times HO_2NO_2$$

To calculate the fraction of $CH_3O_2NO_2$ (f_1 in E1) that dissociates in the NO_2 sample line, we use the cabin temperature we measured near the TD-LIF NO_2 sample line along with the thermal rate constant (Table 2.2). To calculate the fraction of HO_2NO_2 (f_2 in E2) that has dissociated in the $CH_3O_2NO_2$ channel we use the measured oven temperature (~60°C) along with the thermal rate constant (Table 2.2). With E1 and E2, we solve for the NO_2 and $CH_3O_2NO_2$ mixing ratios observed if there is an independent measurement or calculation of HO_2NO_2. During DC3, the correction for the thermal dissociation of $CH_3O_2NO_2$ in XNO_2 ranged from a 0 to 30 pptv (0 to 40%) of the NO_2 mixing ratios at temperatures less than 240 K. During SEAC4RS, the correction ranged from 0 to 23 pptv (0 to 21%). The correction for the thermal decomposition of HO_2NO_2 ranged from 0 to 20 pptv (0 to 11%) for both campaigns.

2.2.4 Accuracy, uncertainty and limit of detection for $CH_3O_2NO_2$

The accuracy of the $CH_3O_2NO_2$ measurements depends on the accuracy of our primary measurement of NO_2, the conversion efficiency in our inlet, and the interference of HO_2NO_2 in the $CH_3O_2NO_2$ channel. The uncertainty of the NO_2 calibration standard is ~5% (Sect. 2.1). Using the rate constant and 2σ uncertainty recommendation from JPL-2011 (Sander et al., 2011) at 60°C, the thermal decomposition rate constant of $CH_3O_2NO_2$ is $36.0^{+19.0}_{-13.0}$ s^{-1}, indicating between 85 to 99% of $CH_3O_2NO_2$ is decomposed at this temperature and a residence time of 0.08

s. Including the uncertainty estimated for the oven temperature (±5°C), the amount of $CH_3O_2NO_2$ decomposed ranges from 70 to 100%.

The transmission efficiency depends on recombination reactions and oxidation of NO. Day et al. (2002) and Wooldridge et al. (2010) showed these to be small effects (~5 – 10%) at NO mixing ratios less than 1 ppbv and pressures in the inlet region less than 400 hPa (ambient pressure). Assuming mixing ratios of 100 pptv for $CH_3O_2NO_2$ and HO_2NO_2, 200 pptv for NO_2 and 100 – 5000 pptv NO, we calculate a positive interference to $CH_3O_2NO_2$ measurements ranging from ~8 – 26% from the oxidation of NO to NO_2. The typical NO mixing ratios at the temperatures where $CH_3O_2NO_2$ is stable range from ~50 – 400 pptv (25^{th} – 75^{th} percentile), and for this range, we calculate a positive interference of less than 10%.

The similarity in the bond strength between HO_2NO_2 and $CH_3O_2NO_2$ (~100 kJ/mol and ~93 kJ/mol, respectively) prevents having a temperature set point that completely separates the two species (Figure 2.4). For the oven temperature selected to decompose $CH_3O_2NO_2$ (60°C) and the residence time in the oven (0.08 s), we calculate approximately 11^{+10}_{-6}% of HO_2NO_2 dissociates in the $CH_3O_2NO_2$ channel.

To summarize, the largest source of uncertainty in the $CH_3O_2NO_2$ measurement is the uncertainty of the thermal decomposition rate for $CH_3O_2NO_2$ (~30%). Other effects, including recombination reactions and the thermal decomposition of HO_2NO_2, are each typically less than 10%. Combining these uncertainties we estimate a total uncertainty of ±40% for the $CH_3O_2NO_2$ measurements. We note that the sum of the NO_2 and $CH_3O_2NO_2$ measurement ($CH_3O_2NO_{2,CHANNEL}$) is more accurate (~10%) than the separate quantities.

The precision of the $CH_3O_2NO_2$ measurements depends on the shot noise of the photon counting rate, the precision of the NO_2 measurement, the concentration of NO_2, and the concentration of $CH_3O_2NO_2$. Using the median NO_2 measured between 10 and 11 km (~200 pptv of NO_2), and using the lower end of the sensitivity observed during DC3 (0.100 cts/pptv), the detection limit for $CH_3O_2NO_2$ is 15 pptv at 60 s^{-1} for S/N = 2. The median limit of detection (S/N = 2 and 60 s averaged data) for the DC3 campaign is shown versus altitude in Figure 2.10b (red line).

2.3 Ambient measurements of $CH_3O_2NO_2$

$CH_3O_2NO_2$ measurements obtained during the DC3 (2012) and SEAC4RS (2013) campaigns are located in NASA's publicly accessible archives: http://www-air.larc.nasa.gov/cgi-bin/ArcView/dc3-seac4rs and https://www-air.larc.nasa.gov/cgi-bin/ArcView/seac4rs.

2.3.1 Characterization of the measurements of ambient $CH_3O_2NO_2$

We utilize the measurements collected during DC3 to validate the temperature selected to fully decompose $CH_3O_2NO_2$ with minimal interference from thermally decomposed HO_2NO_2. First, we ensure that the $CH_3O_2NO_2$ channel behaves as expected: at high ambient temperatures (low altitudes), the $CH_3O_2NO_2$ channel should only be detecting ambient NO_2 (Figure 2.1), but at low ambient temperatures (high altitudes), the $CH_3O_2NO_2$ channel should be detecting NO_2 from

both ambient NO_2 and thermally decomposed $CH_3O_2NO_2$. This behavior is observed, as shown in an example flight from DC3 (Figure 2.6).

We utilize observations of $CH_3O_2NO_2$ near the limit of detection (Figure 2.7 between ~ 21:30 – 22:00 UTC) to calculate an upper limit for the thermal dissociation of HO_2NO_2 in the $CH_3O_2NO_2$ channel. The median observed HO_2NO_2 is 94^{+11}_{-35} pptv (plus 75th quartile and minus 25th quartile). In the $CH_3O_2NO_2$ channel, we observed 24^{+10}_{-6}pptv (median and inter-quartile). Assuming zero for the $CH_3O_2NO_2$ mixing ratio, this gives an upper limit to the HO_2NO_2 present in the $CH_3O_2NO_2$ of ~ 25% of the measured HO_2NO_2. Calculations (Sect. 2.4) suggest the most likely amount of HO_2NO_2 thermally dissociated is ~ 11% with an upper limit based on propagating uncertainties in rate constants of 25 to 30%. The observed values are consistent with this upper limit. We conclude that some (~ 6 pptv calculated assuming photostationary steady state) $CH_3O_2NO_2$ should be present. If we assume this $CH_3O_2NO_2$ is correct, the HO_2NO_2 fraction dissociated is ~20%.

Another way to determine if the temperature selected fully decomposes $CH_3O_2NO_2$ with minimal HO_2NO_2 decomposition is to compare inferred $CH_3O_2NO_2$ ($CH_3O_2NO_{2(inferred)} \equiv \Sigma PNs - (HO_2NO_2 + PAN + PPN)$) to measured $CH_3O_2NO_2$ during the DC3 campaign (Figure 2.8). PAN, PPN, and HO_2NO_2 were measured by chemical ionization-mass spectrometry (Slusher et al., 2004; Kim et al., 2007). The observations used are one minute merged data from temperatures between 220 and 230 K, where the signal of the $CH_3O_2NO_2$ measurements is well above the noise (Figure 2.10b). Using weighted (by accounting for differing uncertainties in the individual points) bivariate least-squares fit (Cantrell, 2008), we calculated a slope of 0.93 (±0.07) after removing a few (378 of 1296 data points) $CH_3O_2NO_{2(inferred)}$ points more than ±3 standard deviations from the median. While the $CH_3O_2NO_{2(inferred)}$ is not completely independent from $CH_3O_2NO_2$, as both $CH_3O_2NO_2$ and ΣPNs are measured by the same technique, the fact that the slope is nearly 1 indicates that the temperature selected for the $CH_3O_2NO_2$ channel is high enough to thermally decompose all $CH_3O_2NO_2$ supporting the conclusion that the thermally decomposed HO_2NO_2 is less than the upper limit (25 – 30%) calculated above. Also, the slope implies that the direct $CH_3O_2NO_2$ measurement is accurate to at least the ±40% estimated above.

2.3.2 Examples of measurements of $CH_3O_2NO_2$

A time series of $CH_3O_2NO_2$ during the flight of 30 May 2012 is shown in Figure 2.7. The flight of 30 May 2012 sampled the aging of deep convective outflow affected by lightning NO_x. The time series shows the variability in the $CH_3O_2NO_2$ measurements that corresponds to the temperature of the ambient air, location of the DC-8, and chemical aging of the convective outflow. Prior to approximately 01:00 UTC, the DC-8 was sampling different altitudes to characterize the aging of convective outflow. At higher altitudes (ambient temperatures less than 230 K), the mean $CH_3O_2NO_2$ was ~100 pptv and ranged from ~26 – 165 pptv. At lower altitudes (ambient temperatures between 230 and 260 K), the mean $CH_3O_2NO_2$ was ~35 pptv and ranged from 0 – 95 pptv.

At these lower altitudes, where the HO_2NO_2 measurements are higher (range ~20 – 170 pptv) than the $CH_3O_2NO_2$ mixing ratios, the structure in the $CH_3O_2NO_2$ measurements is not simply a mirror of the HO_2NO_2 measurements. If there was a large interference from the thermal

decomposition of HO_2NO_2 in the $CH_3O_2NO_2$ channel, we would expect to see similar structure in the two measurements. For example, between 00:00 and 01:00 UTC, the HO_2NO_2 mixing ratio peaks at ~170 pptv whereas at the same time the $CH_3O_2NO_2$ decreases to ~10 pptv. The largest corrections for the thermal decomposition of HO_2NO_2 in the $CH_3O_2NO_2$ channel occur at lower altitudes (Figure 2.6a), where $CH_3O_2NO_2$ lifetime is short (Figure 2.1). This gives us further confidence that the thermal decomposition of HO_2NO_2 is a small interference in the measurement of $CH_3O_2NO_2$.

At 01:00 UTC, the DC-8 started sampling stratospheric air. The $CH_3O_2NO_2$ mixing ratios dropped to ~30 pptv (range 0 – 140 pptv). This is lower than the values observed in the upper troposphere at ambient temperatures less than 230 K. Even though the temperatures in the lower stratosphere are low enough for the $CH_3O_2NO_2$ lifetime to be greater than 10 h, the observations of $CH_3O_2NO_2$ indicate that the lower stratosphere has lower mixing ratios of the precursors of CH_3O_2 needed to form $CH_3O_2NO_2$. These include the peroxy acyl radical from acetaldehyde, which reacts with NO to produce CH_3O_2 (e.g., Tyndall et al., 2001), and CH_3COCH_3, which can photolyze to produce CH_3O_2 (e.g., Folkins and Chatfield, 2000; Jaeglé et al., 2001; Neumaier et al., 2014).

An example of $CH_3O_2NO_2$ behaving as an important NO_x reservoir downwind of deep convection is shown in Figure 2.9. We observed the production of $CH_3O_2NO_2$ in the aging outflow of deep convection during the flight of 21 June 2012 (Figure 2.9). The DC-8 sampled at a constant ambient temperature (~ 225 K) and entered the outflow between 12:00 and 13:00 UTC (0 – 1 hr chemically aged), where the $CH_3O_2NO_2$ mixing ratio was observed to be ~ 0 pptv. The aircraft sampled the outflow until ~ 16:30 UTC (4.5 hr chemically aged), where the $CH_3O_2NO_2$ mixing ratio was observed to be ~ 150 pptv. The apparent $CH_3O_2NO_2$ production rate was ~ 60 pptv/hr; an indication of the importance of this chemistry to understanding upper tropospheric chemistry.

We compare the median $CH_3O_2NO_2$ profiles during DC3 (black), SEAC4RS (dark grey) and ARCTAS-A (blue, as calculated by Browne et al., 2011) in Figure 2.10b. At altitudes above 7 km, higher mixing ratios of $CH_3O_2NO_2$ were observed during both DC3 and SEAC4RS compared to ARCTAS-A due to the influence of deep convection, lightning NO_x, and biomass burning. Also, DC3 and SEAC4RS occurred later in the year (May – June, 2012 for DC3 and August – September, 2013 for SEAC4RS) than ARCTAS-A (April 2008); thus, photochemistry is more active, producing more $CH_3O_2NO_2$. This is consistent with calculations described by Browne et al. (2011), who found modeled $CH_3O_2NO_2$ mixing ratios are higher in the summer than spring. Finally, the observed $CH_3O_2NO_2$ during SEAC4RS at lower altitudes is higher due to the impact of agricultural and biomass burning. Higher NO_2 mixing ratios from biomass burning shift the equilibrium towards $CH_3O_2NO_2$, similar to the higher NO_2 concentrations shifting the equilibrium towards HO_2NO_2 production near an urban area (Spencer et al., 2009). Higher $CH_3O_2NO_2$ mixing ratios due to biomass burning are also consistent with the GEOS-Chem results from Browne et al. (2011).

During DC3, $CH_3O_2NO_2$ measurements drop to below the limit of detection at high altitudes (> 11.5 km) when the aircraft was sampling the stratosphere. The stratosphere is higher during

SEAC4RS since the campaign is occurring later in the season; thus, higher mixing ratios of $CH_3O_2NO_2$ are observed.

Finally, we compare the calculated instantaneous steady state mixing ratios of $CH_3O_2NO_2$ to measured $CH_3O_2NO_2$ during DC3 (Figure 2.11). We limit the comparison to observations for which the calculated lifetime of $CH_3O_2NO_2$ lifetime is less than 10 hrs, the tropospheric composition has not been recently perturbed by fresh NO_x emissions ($NO_x/NO_y < 0.4$) or stratospheric intrusions ($O_3/CO < 1.25$), and to solar zenith angles less than 85 degrees—all conditions that make it more likely that steady-state is achieved in the atmosphere. We used only observations at temperatures less than 250 K where $CH_3O_2NO_2$ is thermally stable. The comparison is also restricted to observations where the $CH_3O_2NO_2$ signal is greater than the noise (Figure 2.10b). Observations with $CH_3O_2NO_2/NO_2$ greater than 1 are excluded as they are also indicative of an air mass that is not in steady state. The reactions used in the model are listed in Table 2.2. Within the variability and uncertainty of the measured and calculated $CH_3O_2NO_2$ mixing ratios, the calculated values are nearly the same as the measured values (median values falling near the one-to-one line). This agreement indicates that for air parcels in photostationary state, the chemistry and kinetics are understood to within ~50%. This also provides us with further confidence in the laboratory measurements of $CH_3O_2NO_2$ rate constants that we use as a guide to instrument design and evaluation.

2.4 Discussion

We observe that $CH_3O_2NO_2$ composed 7% and HO_2NO_2 composed 5% of the median NO_y budget between 220 K and 230 K during DC3, where NO_y is defined as the sum of NO_x, ΣPNs, ΣANs, and HNO_3. This is significant since many transport models neglect $CH_3O_2NO_2$ chemistry. During DC3, these weakly bound species comprised a larger portion of the median NO_y budget than HNO_3 (4%), which is a terminal sink for NO_x. In prior analysis of tropospheric air cooler than 240 K, Murphy et al. (2004) calculated the sum of HO_2NO_2 and $CH_3O_2NO_2$ as the difference between ΣPNs measured by TD-LIF and PAN and PPN measured using gas chromatography with electron capture detection (similar to $CH_3O_2NO_{2(inferred)}$ above). Murphy et al. (2004) reported these two species were a large fraction of the NO_y budget at temperatures cooler than 240 K (17 – 22%), impacting NO_x and radical chemistry. That the percent composition for the non-acyl peroxy nitrates during DC3 were lower than reported by Murphy et al. (2004) is not surprising because the sampling during DC3 was biased toward fresh convective outflow impacted by lightning NO_x, meaning NO_x composed 39% of the NO_y budget versus the 5% for the air observed by Murphy et al. (2004). For background air ($NO_x/NO_y < 0.2$) observed during DC3, $CH_3O_2NO_2$ composed a larger portion of the median NO_y budget (12%), and the median non-acyl peroxy nitrate portion of the NO_y budget ($CH_3O_2NO_2$ + HO_2NO_2 (5%)) have a sum that is similar to the observations by Murphy et al. (2004) of 17%.

The lower NO_x mixing ratios characteristic of the air observed by Murphy et al. (2004) were also characteristic of the air observed by Browne et al. (2011) during ARCTAS-A, as both were springtime measurements in the Arctic. The comparison of ARCTAS-A, DC3, and SEAC4RS is shown in Figure 2.10. The lower NO_2 mixing ratios observed during ARCTAS-A meant the air masses were more dominated by $CH_3O_2NO_2$ than by NO_2 ($CH_3O_2NO_2/(NO_2 + CH_3O_2NO_2)$ ratios closer to 1.0, Figure 2.10c). The dominance of $CH_3O_2NO_2$ means that it is an important source of

NO_2 and that is an important interference for ambient NO_2 measurements. In DC3, the influence of lightning NO_x emissions made the median air masses for the entire campaign more dominated by NO_2 (ratios less than 0.5). The median $CH_3O_2NO_2/(NO_2 + CH_3O_2NO_2)$ ratios are slightly smaller than the ratios calculated in the GEOS-Chem model from Browne et al. (2011) for air influenced by deep convection and lightning. In background air sampled by the DC-8 during DC3, the median $CH_3O_2NO_2/(NO_2 + CH_3O_2NO_2)$ ratio was in the range 0.3 to 0.7 (Figure 2.10c, green). We observed similar median ratios during SEAC4RS (Figure 2.10c, dark grey). These values are closer to the values calculated during ARCTAS (Figure 2.10c, blue; Browne et al., 2011). This indicates that with aging, the ratio shifts toward air more dominated by $CH_3O_2NO_2$, impacting the ozone chemistry of the upper troposphere, as previously described by Browne et al. (2011).

2.5 Conclusion

We report the first measurements of atmospheric $CH_3O_2NO_2$ and report recommendations for instrument design to sample NO_2 free of interferences from thermal decomposition of non-acyl peroxy nitrates. We conclude that for an instruments where the sample lines and/or detection region is at a temperature of 300 K, total residence times of less than 0.1 s are required to keep the interference to NO_2 below 10% of $CH_3O_2NO_2$ and below 1% of HO_2NO_2. We describe a procedure for evaluating the interference of $CH_3O_2NO_2$ in NO_2 using measurements of $CH_3O_2NO_2$. Our measurements show that for temperatures less than 230 K, the median $CH_3O_2NO_2$ is a larger fraction of NO_y than HNO_3, experimental evidence for the important role of $CH_3O_2NO_2$ in the upper troposphere. Our measurements also provide supporting evidence for the conclusion of Browne et al. (2011), who predicted larger $CH_3O_2NO_2$ mixing ratios in summer than in spring using GEOS-Chem.

Table 2.1. Lengths for tubing in the corresponding sections for Figure 2.3.

Campaign	Section A	Section B	Section C	NO_2 Channel Max Residence Time
ARCTAS	0.10 m	0.20 m	2.00 m	0.85 s
DC3	0.10 m	0.08 m	1.50 m	0.50 s
SEAC4RS	1.00 m	0.12 m	0.30 m	0.23 s

Table 2.2. Reactions and rates used in calculating dissociations in instrument and photostationary steady state calculations for $CH_3O_2NO_2$.

Reaction	Rate Constant
$CH_3O_2NO_2 + M \rightleftharpoons CH_3O_2 + NO_2 + M$	Low Pressure Limit = $1.0 \times 10^{-30} \times (T/300)^{-4.8}$ High Pressure Limit = $7.2 \times 10^{-12} \times (T/300)^{-2.1}$ $K_{eq} = 9.5 \times 10^{-29} \times \exp(11234/T)$[a]
$HO_2NO_2 + M \rightleftharpoons HO_2 + NO_2 + M$	Low Pressure Limit = $2.0 \times 10^{-31} \times (T/300)^{-3.4}$ High Pressure Limit = $2.9 \times 10^{-12} \times (T/300)^{-1.1}$ $K_{eq} = 2.1 \times 10^{-27} \times \exp(10900/T)$[a]
$CH_3O_2NO_2 + h\nu \rightarrow CH_3O_2 + NO_2$	Assumed to be equal to measured HO_2NO_2 value
$CH_3O_2NO_2 + h\nu \rightarrow CH_3O + NO_3$	Assumed to be equal to measured HO_2NO_2 value
$CH_4 + OH \rightarrow CH_3O_2 + NO_2$	$2.45 \times 10^{-12} \times \exp(-1775/T)$[a]
$CH_3C(O)O_2 + NO \rightarrow CH_3O_2 + CO_2 + NO_2$	$8.1 \times 10^{-12} \times \exp(270/T)$[a]
$CH_3C(O)O_2 + CH_3C(O)O_2 + 2\ O_2 \rightarrow 2\ CH_3O_2 + 2\ CO_2 + O_2$	$2.9 \times 10^{-12} \times \exp(500/T)$[a]
$CH_3C(O)CH_3 + h\nu + O_2 \rightarrow CH_3C(O)O_2 + CH_3O_2$	Measured
$CH_3OOH + OH \xrightarrow{70\%} CH_3O_2 + H_2O$	$3.8 \times 10^{-12} \times \exp(200/T)$[a]
$CH_3C(O)OH + h\nu + O_2 \rightarrow CH_3O_2 + HCO$	Measured
$CH_3O_2 + NO \rightarrow CH_3O + NO_2$	$2.8 \times 10^{-12} \times \exp(300/T)$[a]
$CH_3O_2 + HO_2 \rightarrow$ Products	$3.8 \times 10^{-13} \times \exp(780/T)$[b]
$CH_3O_2 + CH_3C(O)O_2 \rightarrow$ Products	$2.0 \times 10^{-12} \times \exp(500/T)$[a]
$CH_3O_2 + CH_3O_2 \rightarrow$ Products	$9.5 \times 10^{-14} \times \exp(390/T)$[a]
$CH_3C(O)O_2NO_2 \rightleftharpoons CH_3C(O)O_2 + NO_2$	Low Pressure Limit = $9.7 \times 10^{-29} \times (T/300)^{-5.6}$ High Pressure Limit = $9.3 \times 10^{-12} \times (T/300)^{-1.5}$ $K_{eq} = 9.0 \times 10^{-29} \times \exp(14000/T)$[a]
$CH_3C(O)O_2NO_2 + h\nu \rightarrow CH_3C(O)O_2 + NO_2$	Measured
$CH_3C(O)OOH + OH \rightarrow CH_3C(O)O_2 + H_2O$	3.7×10^{-12}[c]
$CH_3C(O)H + OH + O_2 \rightarrow CH_3C(O)O_2 + H_2O$	$4.7 \times 10^{-12} \times \exp(345/T)$[b]
$CH_3C(O)O_2 + HO_2 \rightarrow$ Products	$5.2 \times 10^{-13} \times \exp(980/T)$[b]
$HO_2NO_2 + OH \rightarrow$ Products	$8.8 \times 10^{-19} \times T^2 \times \exp(1130/T)$[d]

[a] JPL 2011 (Sander et al., 2011)
[b] Atkinson et al. (2006) (http://iupac.pole-ether.fr/htdocs/summary/vol2_summary.pdf)
[c] Master Chemical Mechanism v3.2 (Saunders et al., 2003)
[d] Jiménez et al. (2004)

Table 2.3. Measurements used in this analysis and calculations of the lifetimes in Figure 2.1.

Species	Method	Reference
NO_2, $CH_3O_2NO_2$, ΣPNs	Thermal dissociation-laser induced fluorescence	Thornton et al. (2000) Day et al. (2002)
HO_2NO_2, PAN, PPN	Chemical ionization mass spectrometry	Slusher et al. (2004) Kim et al. (2007)
OH, HO_2	Laser induced fluorescence	Faloona et al. (2004)
UV photolytic frequencies	Spectral radiometry	Shetter and Müller (1999)

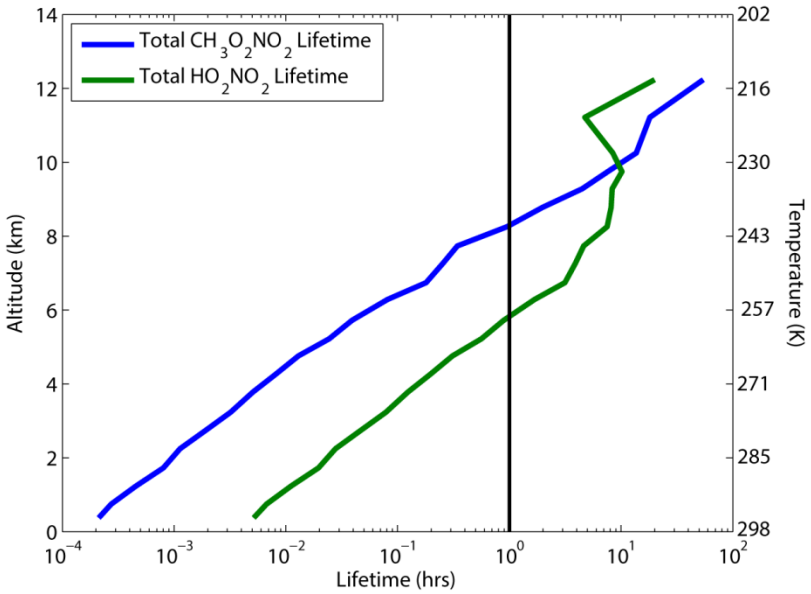

Figure 2.1. Calculated mean total lifetime profile of $CH_3O_2NO_2$ (blue) and HO_2NO_2 (green) for typical conditions observed during DC3 in the daytime. The total lifetime is calculated using observed OH, photolysis rates, and temperatures along with the rate constants listed in Table 2.2. The black line is marks the region where the non-acyl peroxy nitrates have a lifetime longer than 1 hour.

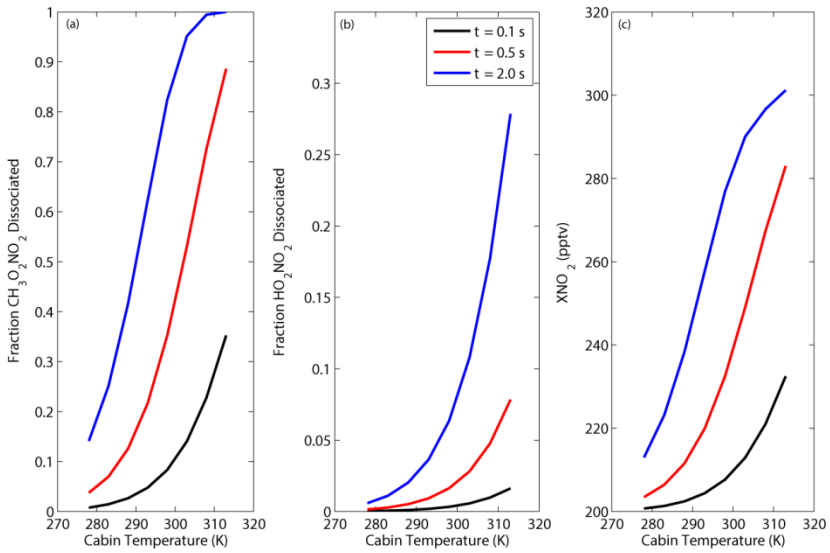

Figure 2.2. Calculated fraction of **(a)** $CH_3O_2NO_2$ and **(b)** HO_2NO_2 dissociated at residence times of 2.0s (blue), 0.5s (red) and 0.1s (black) and cabin temperatures ranging from 275-310K. The calculations are for ambient pressures of 230 hPa and ambient temperatures of ~225 K. **(c)** XNO_2 (XNO_2 = NO_2 + fraction dissociated $CH_3O_2NO_2$ and fraction dissociated HO_2NO_2) as a function of the residence times and cabin temperatures used in **(a)** and **(b)**. We use the median mixing ratios of NO_2 (200 pptv), $CH_3O_2NO_2$ (90 pptv), and HO_2NO_2 (40 pptv) observed between 220 and 230 K during DC3.

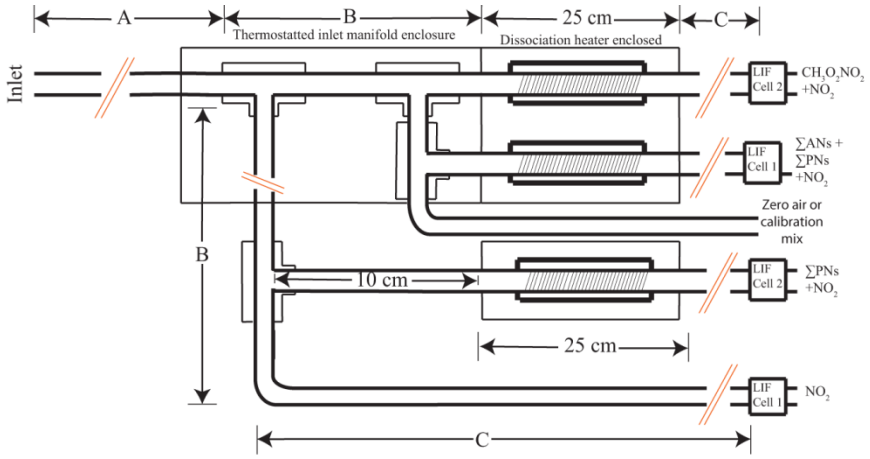

Figure 2.3. Schematic of the TD-LIF inlet sampling manifold. Arrows and letters refer to lengths referenced in Table 2.1. The species measured in each channel is shown at the right, where ΣPNs ≡ PAN + PPN + $CH_3O_2NO_2$ + HO_2NO_2 + … and ΣANs ≡ the sum of gas and aerosol alkyl and multifunctional nitrates.

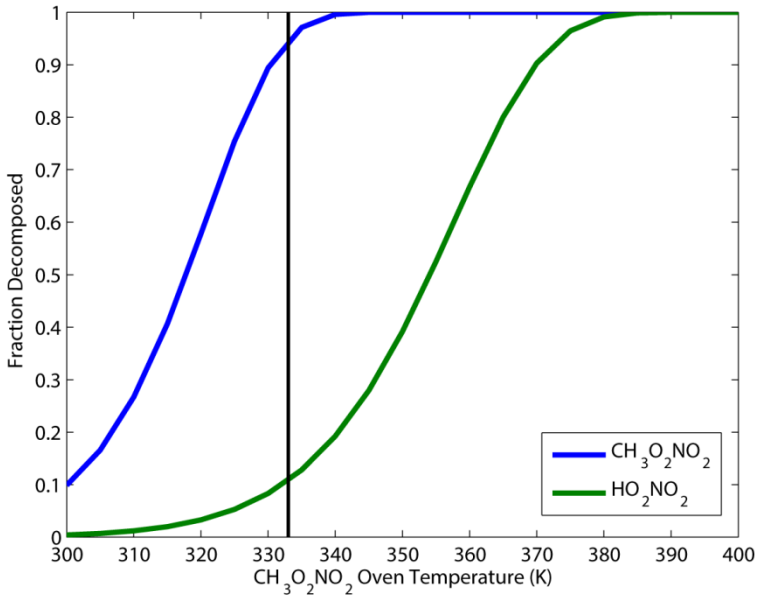

Figure 2.4. The calculated fractional decomposition of $CH_3O_2NO_2$ (blue) and HO_2NO_2 (green) as a function of $CH_3O_2NO_2$ oven temperatures at a pressure of 230 hPa and a residence time of 0.08 s. The black line marks the target temperature (~60°C) for optimal separation of $CH_3O_2NO_2$ and HO_2NO_2. Rates used to calculate the fraction decomposition are shown in Table 2.2.

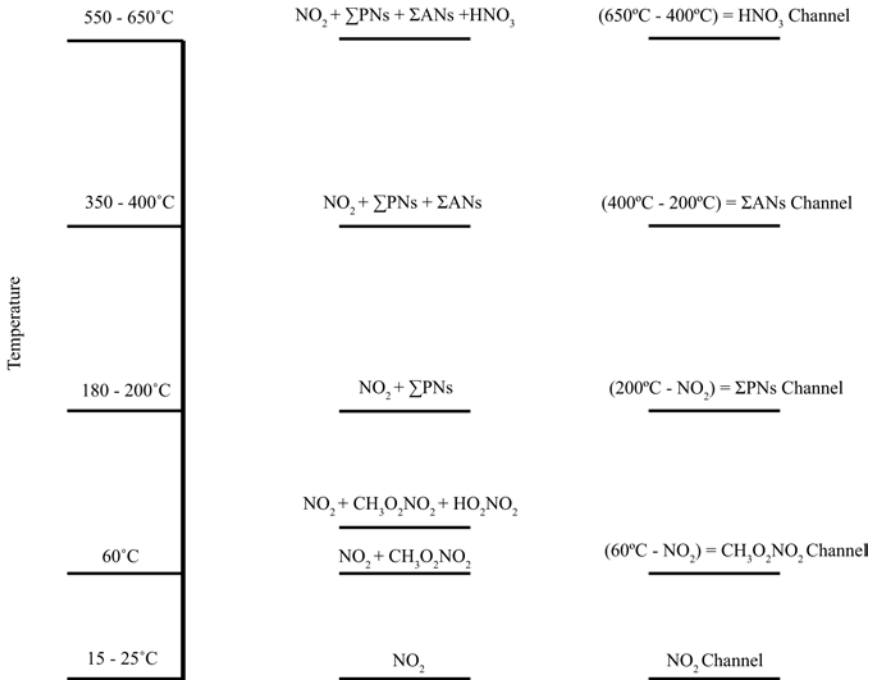

Figure 2.5. Schematic of the species measured in the TD-LIF channels and the temperature set points (temperatures the species dissociate) for those channels. ΣPNs ≡ PAN + PPN + $CH_3O_2NO_2$ + HO_2NO_2 + … and ΣANs ≡ alkyl and multifunctional nitrates. The channel subtracted to calculate the measured species (e.g., $CH_3O_2NO_2$) is shown before the equals sign in the third column.

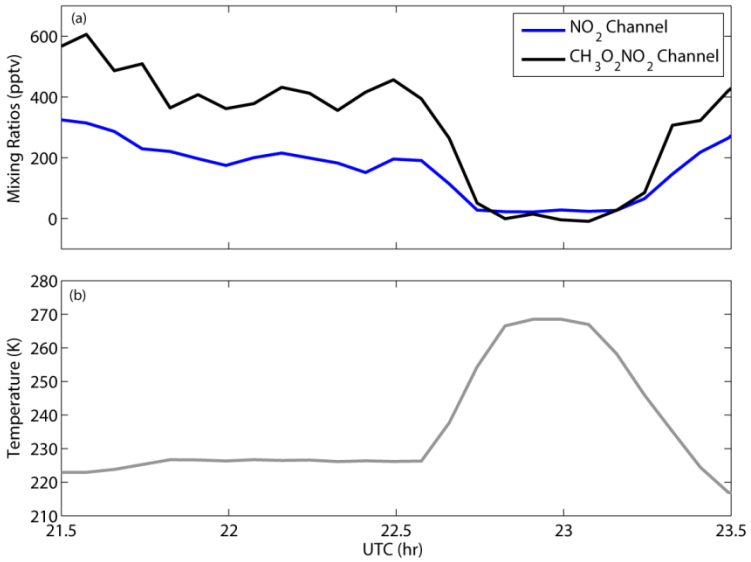

Figure 2.6. Five minute averaged time series of **(a)** NO_2 (blue) and $CH_3O_2NO_2$ (black) channel and **(b)** temperature from a flight on 17 June 2012 during DC3. The local time was approximately midafternoon during this time segment.

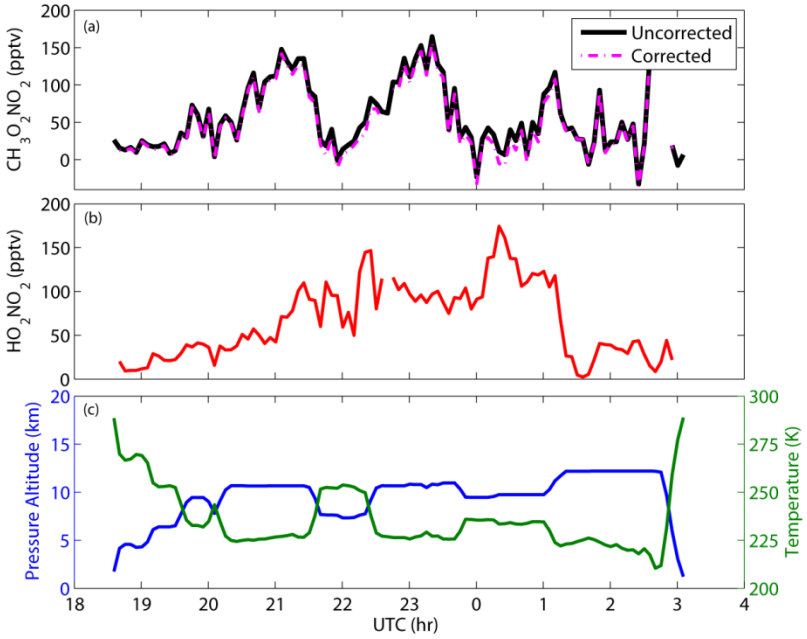

Figure 2.7. Five minute averaged time series of **(a)** uncorrected (black) and corrected (magenta) $CH_3O_2NO_2$ for HO_2NO_2 thermal decomposition, **(b)** HO_2NO_2, and **(c)** pressure altitude (blue) and temperature (green) from a flight on 30 May 2012 during DC3. Local sunset is approximately 00:00 UTC.

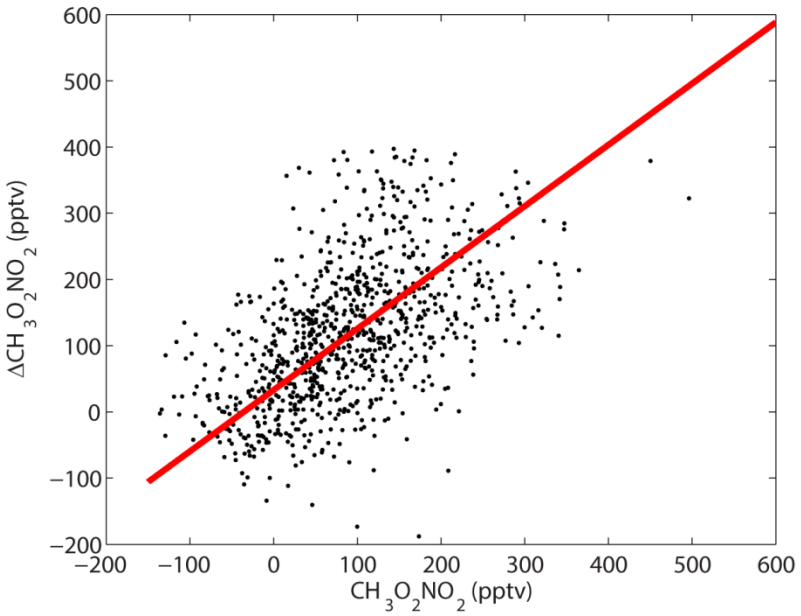

Figure 2.8. $CH_3O_2NO_2$ inferred ($\Delta CH_3O_2NO_2$) as the difference of the total peroxy nitrates minus PAN, PPN, and HO_2NO_2 compared to $CH_3O_2NO_2$ observed by TD-LIF at temperatures between 220 and 230 K. The red line is a weighted fit to the data: slope of 0.93 (±0.07) and intercept of −33.0(±5.9) pptv. The uncertainties used in the calculations are ±40% + 20 pptv for $CH_3O_2NO_2$, ±15% + 20 pptv for ΣPNs, ±15% + 2 pptv for PAN, ±20% + 1 pptv for PPN, and ±30% + 1 pptv for HO_2NO_2. The R^2 of the fit is 0.3.

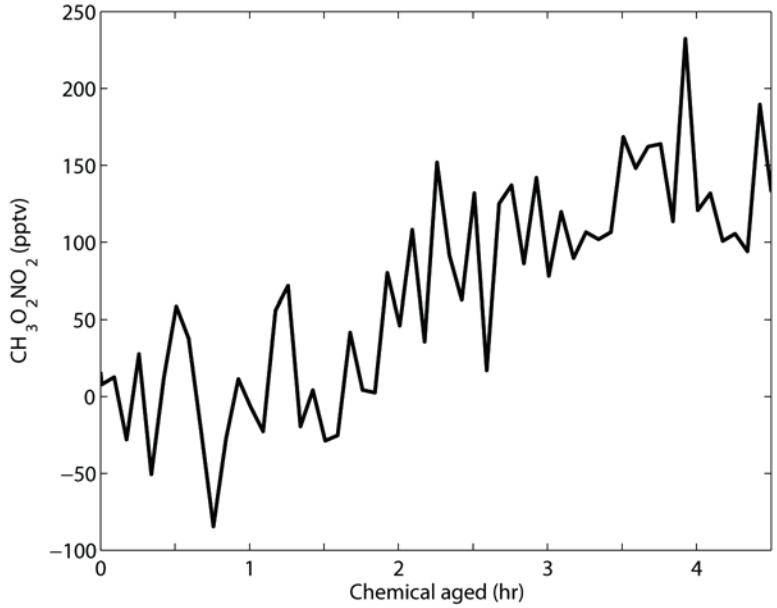

Figure 2.9. Five minute averaged time series of the chemical evolution of $CH_3O_2NO_2$ downwind from convection from a flight on 21 June 2012 during DC3. The x-axis shows the age of the air parcel that the DC-8 started sampling at approximately 12:00 UTC (0 hr), which was the local sunrise.

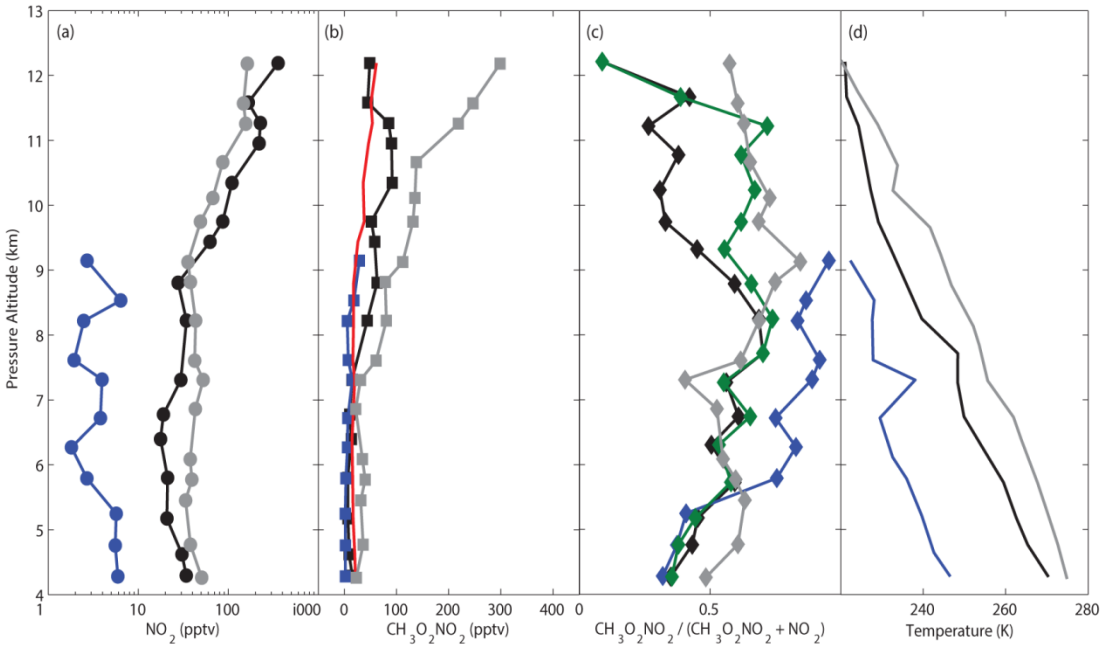

Figure 2.10. The median profile of **(a)** NO_2, **(b)** $CH_3O_2NO_2$, **(c)** $CH_3O_2NO_2/(NO_2 + CH_3O_2NO_2)$, and **(d)** temperature for ARCTAS-A (blue), DC3 (black), and SEAC4RS (dark grey). The red line in **(b)** is the median limit of detection for S/N = 2, 60 s for DC3. The green line in **(c)** is the median $CH_3O_2NO_2/(NO_2 + CH_3O_2NO_2)$ in background air where NO_x/NO_y is less than 0.2 during DC3.

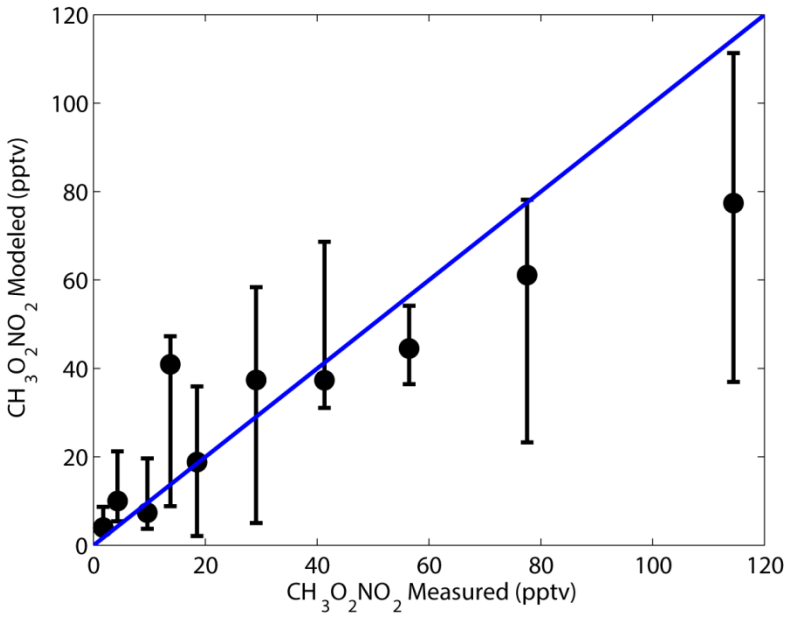

Figure 2.11. Binned modeled versus measured $CH_3O_2NO_2$. The bars identify the interquartile of the modeled $CH_3O_2NO_2$. The blue line has a slope of 1 for reference.

Chapter 3. Observational Constraints on the Oxidation of NO_x in the Upper Troposphere

Adapted from Nault, B. A., Garland, C., Wooldridge, P. J., Brune, W. H., Campuzano-Jost, P., Crounse, J. D., Day, D. A., Dibb, J., Hall, S. R., Huey, L. G., Jimenez, J. L., Liu, X., Mao, J., Mikoviny, T., Peischl, J., Pollack, I. B., Ren, X., Ryerson, T. B., Scheuer, E., Ullmann, K., Wennberg, P. O., Wisthaler, A., Zhang, L., and Cohen, R. C., J. Phys. Chem. A, 2015, *Published.*

3.1 Introduction

In the upper troposphere, where O_3 is an important greenhouse gas (Myre et al., 2013). NO_x ($NO_x \equiv NO + NO_2$) regulates O_3 production. NO_x concentrations in this region of the atmosphere are affected by transport including import from the stratosphere, convection, and large-scale descent, emissions from aircraft, *in situ* production by lightning, and photochemical reactions that convert NO_x to higher oxides, or NO_z (Figure 3.1; Levy et al., 1999; Bertram et al., 2007; Hudman et al., 2007; Liang et al., 2011). The higher oxides include HNO_3 (R1a and R2b), alkyl and multifunctional nitrates (R3b), and acyl and non-acyl peroxy nitrates (R4 and R5).

(R1a) $NO_2 + OH + M \xrightarrow{k_{1a}} HNO_3 + M$

(R1b) $NO_2 + OH + M \xrightarrow{k_{1b}} HOONO + M$

(R−1b) $HOONO + M \xrightarrow{k_{-1b}} NO_2 + OH + M$

(R2a) $NO + HO_2 \xrightarrow{k_{2a}} NO_2 + OH$

(R2b) $NO + HO_2 \xrightarrow{k_{2b}} HNO_3$

(R3a) $NO + RO_2^{\bullet} \xrightarrow{k_{3a}} NO_2 + RO^{\bullet}$

(R3b) $NO + RO_2^{\bullet} \xrightarrow{k_{3b}} RONO_2$

(R4) $NO_2 + R(O)O_2^{\bullet} + M \xrightarrow{k_4} R(O)O_2NO_2 + M$

(R−4) $R(O)O_2NO_2 + M \xrightarrow{k_{-4}} NO_2 + R(O)O_2^{\bullet} + M$

(R5) $NO_2 + RO_2^{\bullet}\ (HO_2^{\bullet}) + M \xrightarrow{k_5} RO_2NO_2\ (HO_2NO_2) + M$

(R−5) $RO_2NO_2\ (HO_2NO_2) + M \xrightarrow{k_{-5}} NO_2 + RO_2^{\bullet}\ (HO_2^{\bullet}) + M$

It has been typically assumed (with support from calculations) that production of HNO_3 strongly regulates the upper tropospheric NO_x lifetime with other NO_z playing a minor role (Jacob et al., 1996; Schultz et al., 2000; Cooper et al., 2011). However, there are relatively few laboratory studies constraining the rate constants for the production of NO_z under the conditions of the upper troposphere (T less than 250 K and P less than 400 hPa). For example, there are no laboratory observations of the rate constants for production of peroxy acetyl nitrate (PAN) and proxy propionyl nitrate (PPN) at temperatures less than 240 K.

The main sink of NO_x, formation of HNO_3, has been subject of the most laboratory experiments. Total loss of OH in the reaction of OH with NO_2 is known to represent production of HNO_3

(R1a) and peroxynitrous acid (HOONO, R1b; Mollner et al., 2010). The production of HOONO has only been studied at room temperature (Mollner et al., 2010), where the branching is 87% to HNO_3 and 13% to HOONO. Significant extrapolations are involved at the temperatures and pressures of the upper troposphere. Estimates of the branching are 75% for HNO_3 and 25% for HOONO at T = 225 K and P = 230 hPa (Sander et al., 2011). In addition to R1a, some laboratory studies (Butkovskaya et al., 2005; Butkovskaya et al., 2007; Butkovskaya et al., 2009) have measured the yield of HNO_3 from the reaction of HO_2 and NO (R2b) and suggest that this minor branch has non-zero yield of less than 1%. Since the overall rate of HO_2 and NO is of order 10 – 100 times faster than the OH and NO_2 reaction in the atmosphere, this low yield, if correct, represents an important sink of NO_x and source of HNO_3. Laboratory measurements of yields in this range are extremely difficult as secondary reactions (e.g., R2a then R1a) in the gas phase or on the walls of the reaction vessel can be significant interferences.

Other sinks of NO_x are also important in the upper troposphere. For example, pernitric acid (HO_2NO_2) and methyl peroxy nitrate ($CH_3O_2NO_2$) are important short-lived NO_x reservoirs—less than 24 hours through thermal decomposition (R4), photolysis (R6), or reaction of HO_2NO_2 with OH (R7). For the conditions of the upper troposphere, several studies of the rate of HO_2 with NO_2 are available (Sander and Peterson, 1984; Kurylo and Ouellette, 1987; Christensen et al., 2004; Bacak et al., 2011) and one study for the rate of CH_3O_2 with NO_2 (Bacak et al., 2006) is available. Bacak et al., 2011) report that the HO_2NO_2 production rate is almost 50% slower than currently recommended (Sander et al., 2011) and observed in prior experiments (Sander and Peterson, 1984; Kurylo and Ouellette, 1987; Christensen et al., 2004).

(R6a) $RO_2NO_2\ (HO_2NO_2) + h\nu \xrightarrow{k_{6a}} NO_2 + RO_2^{\bullet}\ (HO_2^{\bullet})$

(R6b) $RO_2NO_2\ (HO_2NO_2) + h\nu \xrightarrow{k_{6b}} NO_3 + RO^{\bullet}\ (HO^{\bullet})$

(R7) $HO_2NO_2 + OH \xrightarrow{k_7} NO_2 + O_2 + H_2O$

Any increases in the upper tropospheric NO_x lifetime will lead to increases in O_3 concentration (Bacak et al., 2011; Seltzer et al., 2015). This leads to higher O_3 radiative impacts. Recently, Romps et al. (2014) described an analysis of lightning that predicts its increase in a warmer climate. The additional NO_x associated with lightning will result in higher O_3 than today in the upper troposphere and increases in its radiative forcing; thus, it is important to understand NO_x lifetime in the upper troposphere.

To investigate the rates of NO_x oxidation, we analyze a quasi-Lagrangian experiment that observed the temporal evolution of NO, NO_2, $CH_3O_2NO_2$, HO_2NO_2, PAN, PPN, the sum of alkyl and multifunctional nitrates, HNO_3, and submircron aerosol nitrate downwind of a lightning storm on June 21st, 2012. The observations were obtained during the Deep Convective Clouds and Chemistry (DC3) experiment (Barth et al., 2015). To assess the impacts of rate coefficients we derive on the chemistry of NO_x in the upper troposphere, we use a global chemical transport model to compare O_3, OH, HO_2, and NO_x for standard chemistry and the modified set of rate constants.

3.2 Instrumentation

The observations described here were made aboard the NASA DC-8 during the DC3 experiment (May − June, 2012; Barth et al., 2015). All data used in this study can be accessed through the NASA public archives for this mission (DC3 Data Archive). We use the Version 5 60 s merged files.

NO_2 was measured by the UC Berkeley thermal-dissociation laser-induced fluorescence (TD-LIF) instrument (Thornton et al., 2000). Briefly, a tunable dye laser pumped at 7 kHz by a Q-switched, frequency doubled Nd:YAG laser, produces ~20 ns pulses at 585 nm with a bandwidth of 0.06 cm^{-1}. The dye laser is tuned onto (9 s) and off (3 s) an isolated rovibronic feature of the jet-cooled (Cleary et al., 2002) NO_2 at 585 nm. The difference between the two signals is directly proportional to the NO_2 mixing ratios. At the pressures of this flight (230 hPa), the ratio of the resonant peak to the non-resonant background fluorescence is 10 to 1. The laser light is focused through two multi-pass White cells. The red-shifted fluorescence from the excited NO_2 molecules is detected using a red-sensitive photomultiplier tube (Hamamatsu H7421-50). Scattered light is removed using time gated detection and dielectric band pass filters that block light at wavelengths shorter than 700 nm. The instrument is calibrated at least every hour during a level flight leg or after a significant change in altitude using a 4.67 (±0.26) ppmv NO_2 standard (Praxair) diluted to ~ 2 – 8 ppbv in zero air. The accuracy and stability of the reference is compared against a library of other NO_2 standards in our laboratory on a regular basis. Fluorescence quenching by water vapor is accounted for (Thornton et al., 2000) using the diode laser hygrometer (DLH) measurements of H_2O (Diskin et al., 2002). Partial thermal decomposition of $CH_3O_2NO_2$ in the NO_2 sample (Browne et al., 2011) is corrected by concurrent measurements of $CH_3O_2NO_2$ using thermal-dissociation with laser-induced fluorescence detection of the NO_2 enhancement (Nault et al., 2015a). During this flight, the maximum correction to the NO_2 measurements due to thermal decomposition of $CH_3O_2NO_2$ is 10% with a median correction of 7% for the entire flight. The correction is described in Nault et al. (2015a).

The measurements of $CH_3O_2NO_2$, sum of all peroxy nitrates (ΣPNs = PAN + PPN + HO_2NO_2 + $CH_3O_2NO_2$), and sum of alkyl and multifunctional nitrates in the gas- and particle-phase ($\Sigma ANs_{(g+p)}$ = all molecules of the chemical form $RONO_2$) have been described elsewhere (Day et al., 2002; Wooldridge et al., 2010; Rollins et al., 2010; Nault et al., 2015a) and the specific configuration during DC3 by Nault et al. (2015a). Briefly, the $CH_3O_2NO_2$, ΣPNs, and $\Sigma ANs_{(g+p)}$ are detected by thermal conversion to NO_2 in heated quartz tubes (60°C, 200°C, and 400°C, respectively) and detected by laser-induced fluorescence of the NO_2 fragment. The concentrations of $CH_3O_2NO_2$ and ΣPNs are calculated from the difference in the signal between the ambient NO_2 measurements and the 60°C and 200°C channel, respectively. Similarly, the concentrations of $\Sigma ANs_{(g+p)}$ are calculated from the difference in the signal between the 200°C and 400°C channel.

The temperature selected for the thermal decomposition (60°C) of $CH_3O_2NO_2$ was selected to minimize the amount of HO_2NO_2 that thermally decomposed. At that temperature and with a residence time of 0.08 s, we calculated that ~10% of HO_2NO_2 thermally decomposes (Nault et al., 2015a). The $CH_3O_2NO_2$ measurements are corrected using HO_2NO_2 observed by chemical

ionization-mass spectrometry (Kim et al., 2007) as described by Nault et al. (2015a). The maximum correction is 10% with a median correction of 5% for the entire flight. Our estimates indicate that no other peroxy nitrates have important effects on the $CH_3O_2NO_2$ and $\sum$PNs measurements (Nault et al., 2015a).

In addition to the NO_2, $CH_3O_2NO_2$, ΣPNs, and $\Sigma ANs_{(g+p)}$ measurements, we use the measurements of NO and O_3 by chemiluminescence (Ryerson et al., 1999), OH and HO_2 by laser-induced fluorescence (Faloona et al., 2004), gas-phase nitric acid ($HNO_{3,g}$), CH_3OOH, $CH_3C(O)OOH$, and hydroxyacetone by chemical ionization-mass spectrometry (CIMS; Crounse et al., 2006; St. Clair et al., 2010), particle-phase inorganic nitrate (NO_3^-) and particulate organic nitrate ($\Sigma ANs_{(p)}$) by aerosol mass spectrometry (AMS; DeCarlo et al., 2006; Fry et al., 2013), the sum of gas- and particle-phase nitric acid ($HNO_{3(g+p)}$) by mist chamber-ion chromatography (IC; Talbot et al., 1997), hydrocarbons (i.e., ethane, propane, ethene, n-butane) by whole air sampling with gas-chromatography analsysis (Blake et al., 2003); PAN, PPN, and HO_2NO_2 by chemical ionization-mass spectrometry (Slusher et al., 2004; Kim et al., 2007), methyl vinyl ketone (MVK), methacrolein (MACR), acetone, acetaldehyde, isoprene, benzene, toluene, C10 terpenes (i.e., α-pinene) and C8 aromatics (i.e., m-xylene) by proton transfer reaction-mass spectrometry (Wisthaler et al., 2002), and CH_4 by tunable diode laser absorption spectroscopy (Sachse et al., 1987; Diskin et al., 2002; Table 3.1). Here, $HNO_{3(g+p)}$ is taken as the average of the CIMS and IC measurements. An intercomparison and treatment of the HO_2NO_2, peroxy nitrates, and $HNO_{3(g+p)}$ measurements are described in the Appendix A. Also, an intercomparison of photostationary steady state NO_2 versus measured NO_2 is described in the Appendix A.

3.3 Results

On 21 June 2012, the NASA DC-8 sampled the photochemistry of a decaying mesoscale convective system over the central United States (Figure 3.2) at a near constant temperature and pressure of 225 K and 230 hPa (~7.3×10^{18} molecules/cm^3). The decaying mesoscale convective system and flight are described in Barth et al. (2015). Briefly, the DC-8 flew 5 legs spaced at varied distances downwind of the convection (full flight Figure A3). Portions of the last three legs that we characterize as sampling the outflow in a quasi-Lagrangian sense are shown in Figure 3.2, along with our estimate of the location of the cloud outflow marked as the green dashed-dot line. We define time zero as the first point in our sampling at 13:35 UTC. We estimate this was less than 10 minutes after the air left the cloud. The observations used in our analysis are those that are in the portions of the flight track that were approximately perpendicular to the flow. As the outflow was a line source (green line in Figure 3.2), all points sampled can be thought of as having a common chemical origin and time evolution (entire green line) and time evolution from the source of the outflow. The specific data we use are measurements initialized at 13:35 UTC (7:35 local time) and continuing to 8100 s after the initial time (15:50 UTC). Using the distance between the legs (~50 and 100 km) and the wind speed (~25 m/s), we calculate that it takes the air ~2000 s to travel from a point in leg 1 to 2 and 4000 s from a point in leg 2 to 3, respectively. Based on this calculation, the observation time (relative to 13:35 UTC) and the transit time from that point are approximately equal, and we define the observation time difference as the time that the air parcel has evolved in the subsequent analysis.

Initializing the observations at the point observed at 13:35 UTC, we observed a decay in NO_x and production of $CH_3O_2NO_2$, HO_2NO_2, PAN, PPN, ΣPNs_i, $\Sigma ANs_{(g+p)}$, and $HNO_{3(g+p)}$ (Figure 3.3 and A4). NO and NO_2 decayed by 190(±70) and 90(±20) pptv from an initial median mixing ratio of 670 and 270 pptv, respectively. The uncertainty in the decay represents the inter-quartile of the change. This corresponds to a total loss rate of $2.6(\pm0.6)\times10^5$ molecules/cm^3/s, if we assume chemical loss of NO_x is constant and linear over the 8100 s between the initial and final observation. Over the same interval, the production of the four peroxy nitrates was 140(±25) ($CH_3O_2NO_2$), 20(±5) (HO_2NO_2), 15(±5) (PAN), and 5(±1) (PPN) pptv. The initial median mixing ratios for the four peroxy nitrates was 0 ($CH_3O_2NO_2$), 50 (HO_2NO_2), 210 (PAN), and 20 (PPN) pptv. The $\Sigma ANs_{(g+p)}$ concentration grew 45(±20) pptv, from an initial 105 pptv, or $4.1(\pm1.8)\times10^4$ molecules/cm^3/s, while $\sum ANs_{(p)}$ increased by 7(±2) pptv, from an initial 5 pptv. Finally, $HNO_{3(g+p)}$ increased by 40(±5) pptv, from an initial 38 pptv, or $3.6(\pm0.5)\times10^4$ molecules/cm^3/s. The loss rate of NO_x is, within the measurement uncertainty, identical to the production rate of the higher oxide species ($2.3(\pm0.3)\times10^5$ molecules/cm^3/s), indicating the observations of the decay of NO_x are consistent with the formation of NO_z.

Analysis of observations of ethene, ethyne, and toluene confirm the air mass is evolving in isolation with little mixing. These three hydrocarbons are selected since their only known source in the upper troposphere is convection (Bechara et al., 2010; Apel et al., 2012). OH was constant to within 25% in this segment of the flight at 9.5×10^6 molecules/cm^3. The OH concentration stayed constant during this time since its sources (e.g., CH_2O) and sinks (e.g., NO_x) decayed at similar rates. Using the measured decay of ethene—initial median mixing ratio of 43 pptv and final median mixing ratio of 14 pptv—and this OH concentration, we find a value of $1.0(\pm0.4)\times10^{-11}$ cm^3/molecules/s (Figure 3.4) for the rate constant for the reaction of ethene with OH. The 2σ uncertainty of 40% is determined by adding the uncertainty of the slope (±7%) and the uncertainty of the OH measurement (1σ ≈ 16%) in quadrature. This is nearly identical to the recommended rate constant of $8.9^{+2.1}_{-1.9}\times10^{-12}$ cm^3/molecules/s at 225 K and 230 hPa (Sander et al., 2011). Doing a similar analysis with the decay of ethyne (initial and final median values of 98 to 89 pptv, respectively) and toluene (initial and final median values of 25 pptv to 14 pptv, respectively), we find values of $6.3(\pm3.5)\times10^{-13}$ and $1.1(\pm0.4)\times10^{-11}$ cm^3/molecules/s (Figure A5), respectively. These ethyne and toluene rate constants are also nearly identical to the recommended rate constants of $7.0^{+1.1}_{-1.0}\times10^{-13}$ and $8.8^{+8.2}_{-4.3}\times10^{-12}$ cm^3/molecules/s, respectively (Atkinson, 1986; Sander et al., 2011). The 2σ is calculated the same as for the ethene rate constant. In addition to confirming the air parcel is evolving in isolation, the ability to calculate these three rate constants within the uncertainty of the recommended values support the combined assumptions made about the evolution of the air parcel as a quasi-Lagrangian air parcel for 8100 s. If we assume the uncertainty in the slopes of the calculations is largely driven by uncertainty in the elapsed time, then the uncertainty in time is 10 – 40%. However, other uncertainties likely contribute, indicating a smaller range for the uncertainty in reaction time is more likely. In conclusion, the analysis of the hydrocarbon decay confirms that the initial observations (t = 0) occurred at 13:35 UTC and confirms our time coordinates as time in seconds since 13:35 UTC.

3.4 Analysis

3.4.1 Nitric acid production

We apply the same assumptions to analysis of the rate of oxidation of NO_x, starting with an analysis of $HNO_{3(g+p)}$ production. The $HNO_{3(g+p)}$ production rate, $dHNO_{3(p+g)}/dt$, is calculated by subtracting the initial $HNO_{3(g+p)}$ concentrations at time 0, which is 2.8×10^8 molecules/cm^3 at 13:35 UTC, from $HNO_{3(g+p)}$ concentrations at time t. We use small time increments to account for other processes affecting the NO_2 available for reaction (R4 – R5 and photolysis). The measured $dHNO_{3(g+p)}/dt$ is plotted versus the corresponding NO_2 concentration at that time, t (Figure 3.5). Similar to the hydrocarbon rate constant calculation (Sect. 3.3), we assume any uncertainty in the time after the initial observation is incorporated in the uncertainty of the slope. We find that the rate constant is $6.2(\pm2.9)\times10^{-12}$ cm^3/molecules/s, with the 2σ uncertainty defined as for ethene. This rate constant (T = 225 K and P = 230 hPa) is slower than recommended by Atkinson et al. (2004) and Sander et al. (2011) and nearly identical to the recommendation of Henderson et al. (2012) who derived a slower rate based on observations of NO_x and HNO_3 concentrations in the upper troposphere during the Intercontinental Chemical Transport Experiment – North America (Figure 3.6). Though the rate constant we calculated is lower than Sander et al. (2011) by 30%, the value we calculated overlaps with the lower bound of the 2σ uncertainty, which is 6.1×10^{-12} cm^3/molecules/s from Sander et al. (2011).

Given that the standard k_{1a} rate constant alone results in more rapid production of HNO_3 than we observe, it is straightforward to conclude that any additional production from the reaction of HO_2 with NO to produce HNO_3 (R2b) must be accompanied by further slowing of the k_{1a} rate. In the air mass we are evaluating, HO_2 was constant to within 25% at 6.7×10^7 molecules/cm^3. If the k_{1a} rate were zero, than the measurements would give the k_{2b} of $1.9(\pm1.0)\times10^{-13}$ cm^3/molecules/s. If this were the case, we calculate a branching ratio of 1.7% for HNO_3 production in the HO_2 and NO reaction. On the other hand, if we assume the production by OH and NO_2 is 50% of the recommended value ($\sim4.4\times10^{-12}$ cm^3/molecules/s), then we find a branching ratio no larger than 0.8% for R2b. This is similar to the laboratory value (Butkovskaya et al., 2005; Butkovskaya et al., 2007; Butkovskaya et al., 2009). For the R2b branching ratios in the range of 0 to 0.7%, we find k_{1a} ranges from $6.2(\pm2.9)$ – $4.7(\pm2.6)\times10^{-12}$ cm^3/molecules/s, respectively.

3.4.2 Speciated peroxy nitrate production

The observed production rates of PAN, PPN, $CH_3O_2NO_2$, and HO_2NO_2 versus NO_2 are shown in Figure 3.7. The calculations to produce Figure 3.7 are similar to the $HNO_{3(g+p)}$ production and described in Sect. 3.4.2. Unlike HNO_3, we do not have observations of the respective radical species that produce the peroxy nitrates, except for HO_2NO_2. We use the observations (Table 3.1) to calculate the production rates of the respective radical species using the rate constants found in Table A1 – A3. For the case of PPN, we use the relationship observed by Singh et al. (2004) between acetaldehyde and propanal to estimate propanal, which was not observed. Then, we use the calculated radical production rate and observed slopes from Figure 3.7 to converge to a radical concentration and NO_2 rate constant. All the peroxy nitrate lifetimes are calculated to be longer than the length of the experiment (3.5, 13, and 464 hours for HO_2NO_2, $CH_3O_2NO_2$, and PAN/PPN, respectively). Also, the HO_2NO_2 produciton rate is calculated to be a factor of 1.5 to

3 higher than the rate; therefore, the losses of the peroxy nitrates are not important to the assessment of the speciated peroxy nitrate production rate constants.

The calculated rate constants for the speciated peroxy nitrates are compared with the recommended rate constants in Table 3.2. The uncertainty in the rate constants, ranging from ~ 50 – ~75%, is defined by the uncertainty in the slopes and the spread in the radical concentrations (±25% for the inter-quartiles) or the uncertainty in the HO_2 concentration (1σ ≈ 16%).We find agreement (less than 30% difference) between the recommended (Sander et al., 2011) and calculated rate constants for the peroxy nitrates except for HO_2NO_2. Our calculated rate constants support the current recommendations (Sander et al., 2011) for the production rates of PAN, PPN, and $CH_3O_2NO_2$ for the conditions of the upper troposphere and the findings of Bacak et al. (2011), that the HO_2NO_2 production is slower than the recommendation by ~50%. The lower HO_2NO_2 is also consistent with the conclusions of Kim et al. (2007), that the current recommendations (Sander et al., 2011) produced more HO_2NO_2 than observed in the upper troposphere. To our knowledge, this is the first time that the PAN and PPN production rates have been reported for the conditions representative of the upper troposphere.

3.4.3 Alkyl and multifunctional nitrate production

To evaluate the production of $\sum ANs_{(g+p)}$, we compare $\Sigma ANs_{(g+p)}$ and O_3 mixing ratios (Figure 3.8a). As described by Perring et al. (2013), the slope of a plot of O_3 versus $\Sigma ANs_{(g+p)}$ is approximately equal to 2/α, where α is the ratio of $k_{3a}/(k_{3a} + k_{3b})$, as seen in E1 – E3. This assumes all the hydrocarbons oxidized produce two O_3 molecules (γ = 2), meaning that 2 peroxy radicals are rapidly produced following the photooxidation of the hydrocarbon (Perring et al., 2013).

(E1) $$P(O_3) = \sum_i \gamma_i (1 - \alpha_i) k_{OH+RH_i} [OH][RH_i]$$

(E2) $$P\left(\sum ANs_{(g+p)}\right) = \sum_i \alpha_i k_{OH+RH_i} [OH][RH_i]$$

(E3) $$P(O_3) = \frac{\bar{\gamma}(1-\bar{\alpha})}{\bar{\alpha}} P\left(\sum ANs_{(g+p)}\right) \approx \frac{2}{\bar{\alpha}} P\left(\sum ANs_{(g+p)}\right)$$

From the O_3 versus $\sum ANs_{(g+p)}$ correlation, we calculate an effective branching ratio, $\overline{\alpha}$, (1σ) of 8(±2)%.

For comparison, we calculate the $\Sigma ANs_{(g+p)}$ production rate directly using the temperature and pressure dependent parameterization of $\Sigma ANs_{(g+p)}$ formation from Carter and Atkinson (1989) and the observations of the various hydrocarbons (Tables 3.1 and A4 and description of calculation in Appendix A). Lee et al. (2014a) showed that at 273 K, $\Sigma ANs_{(g+p)}$ production is 50% more efficient than at 300 K and even larger increases are calculated here for T = 225 K (250% more efficient). The direct calculation gives an average (1σ) $\overline{\alpha}$ of 7(±4)%. The uncertainty in $\overline{\alpha}$ includes uncertainty in the rate constants (~15%), the hydrocarbon concentrations (~10%), the OH concentration (~16%), and the temperature and pressure dependent α value (~30%). The calculated increase of ΣANs over the quasi-Lagrangian portion of the flight is 46(±18) pptv (Figure 3.8b).

In this air mass, the hydrocarbons that produce the largest fraction of the $\Sigma ANs_{(g+p)}$ (~70% or 34 pptv) are a group that have chemical lifetimes of less than 1 hour (MVK, MACR, isoprene, and monoterpene) and a group with longer lifetimes but still less than 6 hours (greater than C6 hydrocarbons). These short lifetimes suggest that the $\Sigma ANs_{(g+p)}$ production rate will not be sustained downwind of lightning NO_x injection into the upper troposphere and only impacts the NO_x lifetime in the near-field of the NO_x injection. Observations of $\Sigma ANs_{(g+p)}$ in the upper troposphere were typically ~90 pptv, which is a factor of 2 – 4 lower than the $\Sigma ANs_{(g+p)}$ mixing ratios in the outflow of convection, confirming that $\Sigma ANs_{(g+p)}$ production is primarily important in the near-field (Figure 3.3c).

The multifunctional organic nitrates produced after radical isomerization or from biogenic hydrocarbons at the low temperatures of the upper troposphere are expected to have low vapor pressures and condense onto aerosol particles. During the flight, an apparent production rate of 2.2×10^{-3} μg/m^3 (at ambient T and P), or 3 pptv, $\Sigma ANs_{(p)}$ was observed (Figure 3.9). We use the method described by Fry et al. (2013) to differentiate between $NO_3^-{}_{(p)}$ and $\sum ANs_{(p)}$. This accounts for approximately 7% of the $\Sigma ANs_{(g+p)}$ observed during the flight.

We calculate the vapor pressures of the individual $\Sigma ANs_{(g)}$ using the SIMPOL.1 model (Pankow and Asher, 2008) and the contribution to the aerosol phase using the equilibrium absorptive partitioning formalism (Pankow, 1994; E4 – E5 and Table A5). The largest contribution to the $\Sigma ANs_{(p)}$ are the monoterpene hydroxy nitrates, isoprene dihydroxy dinitrates, and hydroxy nitrates formed from the isomerization of n-hexane, methyl hexanes, and n-heptane (Table A5). Explanation of the variables is found in Appendix A.

(E4) $$K_p = \frac{R \cdot T \cdot f_{om}}{MW_{om} \cdot 10^6 \cdot \zeta \cdot p_{vap}}$$

(E5) $$m_{AN_{i,p}} = K_{p,i} \cdot m_{om} \cdot m_{AN_{i,g}}$$

The calculated $\Sigma ANs_{(p)}$ at the end of the experiment is 5.8×10^{-4} μg/m^3, which is a factor 4 lower than observations. Prior studies have concluded that the SIMPOL.1 model can overestimate the vapor pressures of multifunctional nitrates by up to 2 orders of magnitude, which is compounded by the need to estimate them at unusually low temperatures (225 K; Leungsakul et al., 2005; Fry et al., 2009; Fry et al., 2011). Given the prior discrepancy, a factor of 4 difference is not surprising. If the estimated vapor pressures are reduced by a factor of 3 (well within the uncertainties), then good model-measurement agreement is observed (Figure 3.9).

3.5 Atmospheric Implications

Our results indicate that both the HNO_3 and HO_2NO_2 production rate are slower in the upper troposphere than in current models, consistent with recent reports (Kim et al., 2007; Henderson et al., 2011; Seltzer et al., 2015). Production of $\Sigma ANs_{(g+p)}$ depends on temperature and, as a result, is more rapid than in some current models. Production of $CH_3O_2NO_2$, PAN, and PPN are observed to occur at the rates currently recommended, although many models do not include $CH_3O_2NO_2$. Incorporating all of these changes and using the observations during the DC3 experiment to constrain a steady state model, we find the NO_x lifetime increases by 20% (Figure

3.10), leading up to as much as ~10 hour increases in the NO_x lifetime, and consequently, to higher O_3 production.

Some recent model studies have added the R2b yield without adjustment of the HNO_3 production rate (Cariolle et al., 2008; Søvde et al., 2011; Gottschaldt et al., 2013). Not surprisingly, these models result in too little NO_x and too much HNO_3 compared to observations. One study (Seltzer et al., 2015) decreased the HNO_3 production rate based on the recommendations from Henderson et al. (2012), who analyzed upper tropospheric NO_x observations from the Intercontinental Chemical Transport Experiment – North America, and the authors did not include R2b. The slower HNO_3 production rate decreased the HNO_3 concentrations by ~5 – 20 pptv and increased the NO_x concentrations by a similar amount. Bacak et al. (2011) calculated the impact of the slower HO_2NO_2 production rate on HO_2NO_2 and NO_x. They report a decrease in HO_2NO_2 of 30 – 40% and an increase in NO_x of 5 – 20%.

To investigate the impacts of the slower HNO_3 and HO_2NO_2 production compared to current recommendations, we use GEOS-Chem v9-02b (details in Appendix A) to model the year 2012 (Figure 3.11). The largest NO_x increases (> 15 pptv for the entire year) occur over regions (central Africa, southeast United States, and northern India) of high lightning and deep convection (e.g., Miyazaki et al., 2014). The combined effects of slower HNO_3 and slower HO_2NO_2 production lead to larger changes in NO_x and O_3 concentrations than calculated with only a slower HNO_3 rate (Seltzer et al., 2015). The increases in NO_x concentrations are associated with decreases in HNO_3 and HO_2NO_2 concentrations (up to 20 and 15 pptv, respectively) and increases in OH, PAN, $CH_3O_2NO_2$, and O_3 concentrations (up to 0.04, 15, and 5 pptv and 5 ppbv, respectively). HO_2 concentrations change little due to the competing effects of decreased HO_2NO_2 production and increased NO concentrations. The increases in both PAN and $CH_3O_2NO_2$ concentrations are associated with O_3 increases. The increased production of these less stable NO_z species allows transport of NO_x and leads to O_3 production downwind of the NO_x source (Fischer et al., 2014).

3.6 Conclusions

We have directly measured the production rates of speciated peroxy nitrates, alkyl and multifuctional nitrates, and HNO_3 in the upper troposphere. Using these observations to infer rate constants for the reactions at the temperature and pressure of the upper troposphere, we find that the rate of OH and NO_2 (k_{1a}) to produce HNO_3 is slower than currently recommended, making peroxy nitrate production as important as HNO_3 production as a sink of NO_x in the near field of lightning NO_x injection. The observations indicate that any HNO_3 production from the reaction of HO_2 with NO is small, which suggests the combined effects of k_{1a} and k_{2b} should not exceed the estimate for k_{1a} when k_{2b} is assumed to be zero. We also calculate that the HO_2NO_2 production rate is ~50% slower than currently recommended, supporting conclusions of Bacak et al. (2011). We show that in the near field of deep convection, the effective average branching ratio to forming $\sum ANs_{(g+p)}$, $\overline{\alpha}$, is high (~8%) and dominated by short-lived hydrocarbons. Combining these ideas in a global chemical transport model, we demonstrate that decreases in the HNO_3 and HO_2NO_2 production rates lead to increases in the calculated upper tropospheric NO_x (10 – 14%), OH (10 – 13%), and O_3 (5 – 6%) concentrations.

Table 3.1. Measurements used in this analysis to calculate rate constants, peroxy radical concentrations, average α, and ΣANs production rate.

Instrument	Species
Chemiluminescence[a]	NO, O_3
Thermal-Dissociation Laser-Induced Fluorescence[b]	NO_2, $CH_3O_2NO_2$, ΣPNs, $\Sigma ANs_{(g+p)}$
Laser-Induced Fluorescence[c]	OH, HO_2
Chemical Ionization-Mass Spectrometry[d]	$HNO_{3,g}$, CH_3OOH, $CH_3C(O)OOH$, Hydroxyacetone
Aerosol Mass Spectrometry[e]	$NO_3^-{}_{(p)}$, $\Sigma ANs_{(p)}$
Mist Chamber-Ion Chromatography[f]	$HNO_{3(g+p)}$
Chemical Ionization-Mass Spectrometry[g]	PAN, PPN, HO_2NO_2
Spectral Radiometry[h]	Photolysis Rates
Whole Air Sampler[i]	Hydrocarbons
Proton Transfer Reaction Mass Spectrometry[j]	Acetaldehyde, Acetone, Benzene, C8 Aromatics, Isoprene, Monoterpenes, MVK + MACR, Toluene
Tunable Diode Laser Absorption Spectroscopy[k]	CH_4

[a] Ryerson et al. (1999).
[b] Thornton et al. (2000), Day et al. (2002), Wooldridge et al. (2010), Rollins et al. (2010), and Nault et al. (2015a).
[c] Faloona et al. (2004).
[d] Crounse et al. (2006) and St. Clair et al. (2010).
[e] DeCarlo et al. (2006) and Fry et al. (2013).
[f] Talbot et al. (1997).
[g] Slusher et al. (2004) and Kim et al. (2007).
[h] Shetter and Müller (1999).
[i] Blake et al. (2003).
[j] Wisthaler et al. (2002).
[k] Sachse et al. (1987) and Diskin et al. (2002).

Table 3.2. Calculated and recommended rate constants (±2σ uncertainty) for speciated peroxy nitrates at T = 225 K and P = 230 hPa.[a]

Species	Calculated Rate Constant	Sander et al. Recommendations[b]	Recent Laboratory Results
PAN	$1.3(\pm 0.8)\times 10^{-11}$	$1.3^{+0.4}_{-0.3} \times 10^{-11}$	N/A
PPN	$7.3(\pm 3.4)\times 10^{-12}$	$7.9^{+10.0}_{-4.4} \times 10^{-12}$	N/A
$CH_3O_2NO_2$	$7.2(\pm 5.7)\times 10^{-12}$	$5.7^{+3.9}_{-2.3} \times 10^{-12}$	$6.4(\pm 0.5)\times 10^{-12}$[c]
HO_2NO_2	$5.1(\pm 3.1)\times 10^{-13}$	$1.2^{+0.4}_{-0.3} \times 10^{-12}$	$6.7^{+2.2}_{-1.7} \times 10^{-13}$[d]

[a]Rate constants used to calculate the peroxy radical species are found in Tables A1 – A3.
[b] Sander et al. (2011).
[c] Bacak et al. (2006). Rate is measured at 223 K and 267 hPa.
[d] Bacak et al. (2011).

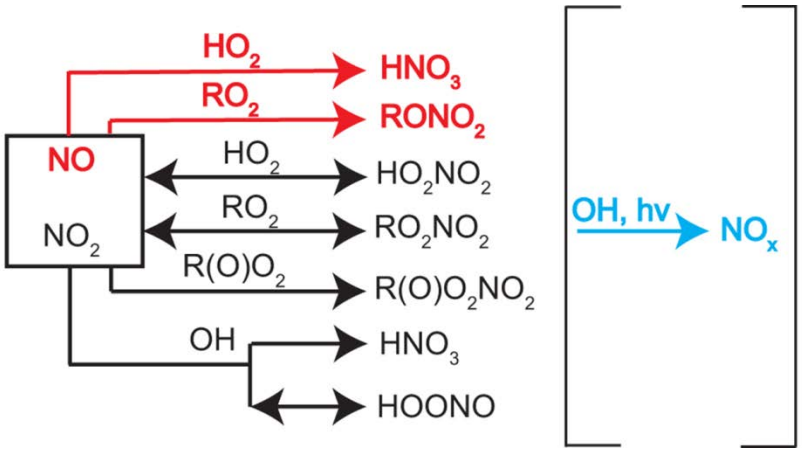

Figure 3.1. Daytime NO_x fate in the upper troposphere. Reactions or channels that are not NO_x sinks (e.g., R2a) are not included. Double arrows indicate important thermal decomposition reactions that occur in the upper troposphere. Arrows and compounds in red (black) indicate reactions and products with NO (NO_2), and the blue arrow and reactants (products) in the bracket correspond to all the products. The lifetime for conversion back NO_x in the upper troposphere by photolysis and reactions with OH is days for all species except HO_2NO_2 and HOONO. For these two species, the lifetime is hours in the upper troposphere.

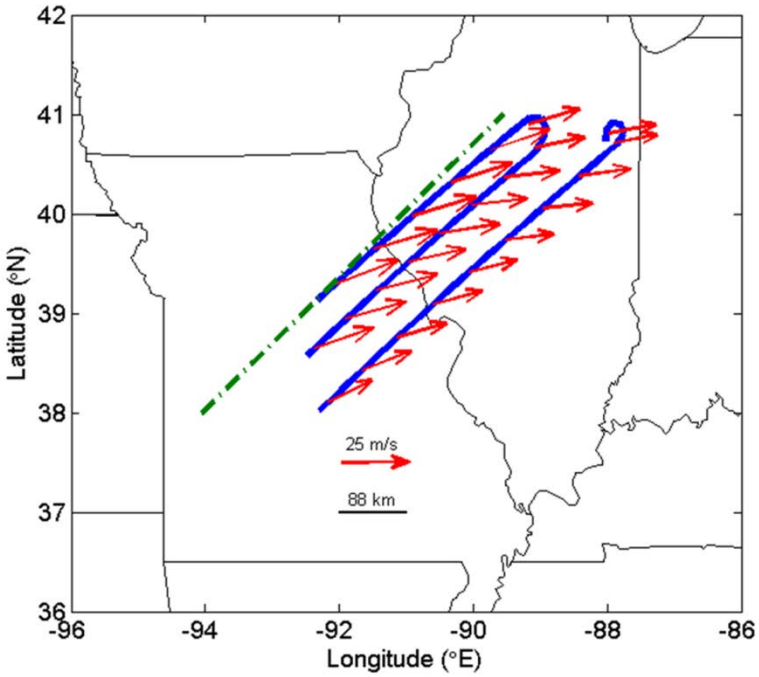

Figure 3.2. Portions of the NASA DC-8 flight path (blue) used to calculate all the rate constants. The wind direction and relative speed observed on the DC-8 for the 21 June 2012 flight is shown as red arrows. The edge of the cloud that marks time equals 0 for the Lagrangian observations is shown as the green dashed-dot line. Leg 1, 2, and 3 corresponds to the left most, center, and right most flight tracks. Red arrow and black horizontal line corresponds to 25 m/s wind speed and 88 km distance, respectively.

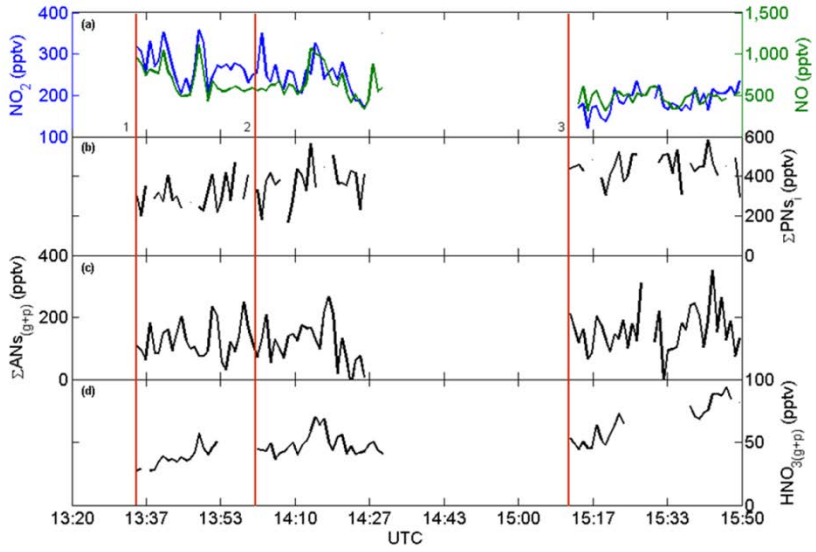

Figure 3.3. Time series of **(a)** NO and NO_2, **(b)** ΣPNs_i, **(c)** $\Sigma ANs_{(g+p)}$, and **(d)** $HNO_{3(g+p)}$, where $\Sigma PNs_i = CH_3O_2NO_2 + HO_2NO_2 + PAN + PPN$ and $HNO_{3(g+p)}$ is the average of the IC and CIMS data. Note, NO_2 is blue and the left y-axis and NO is green and the right y-axis in **(a)**. Measurements not shown between 14:30 and 15:10 UTC are when the DC-8 sampled air outside the Lagragian parcel. The vertical red lines correspond to the beginning of Legs 1, 2, and 3 in Figure 3.2.

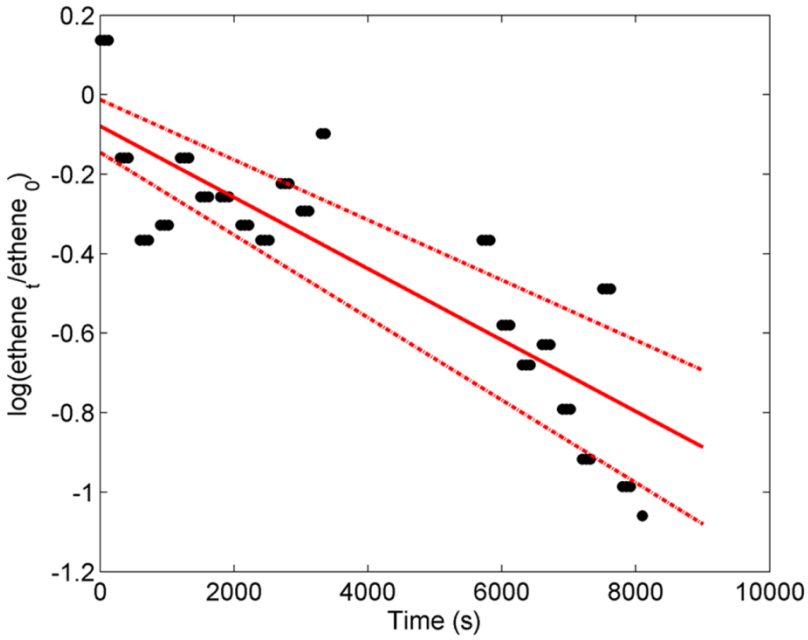

Figure 3.4. First order loss rate of ethene. The solid red line is the slope (-9.6×10^{-5} s^{-1}) and the dashed-dot red line is the 2σ uncertainty ($\pm1.4\times10^{-5}$ s^{-1}).

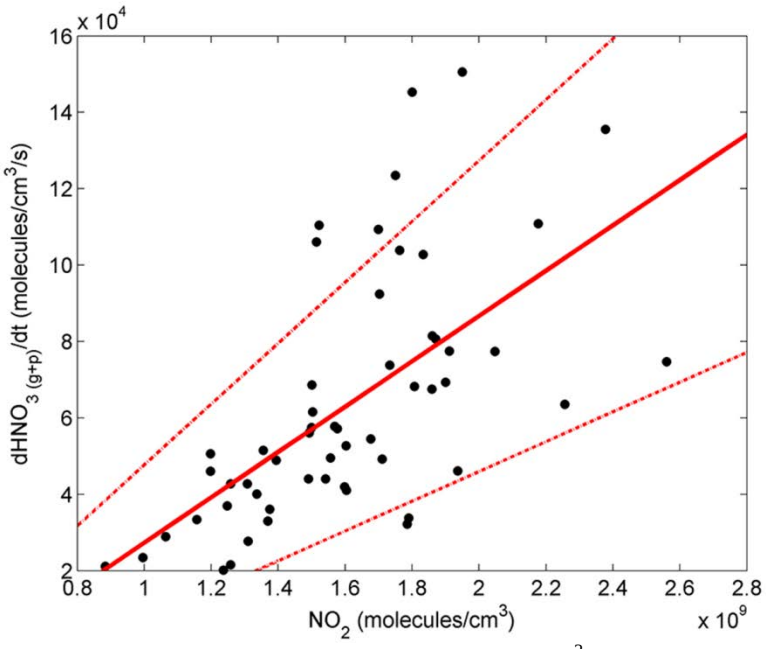

Figure 3.5. The observed $HNO_{3(g+p)}$ production rate (molecules/cm^3/s) versus NO_2 (molecules/cm^3). The solid red line is the slope (6.2×10^{-5} s^{-1}) and the dashed-dot line is the 2σ uncertainty ($\pm2.0\times10^{-5}$ s^{-1}).

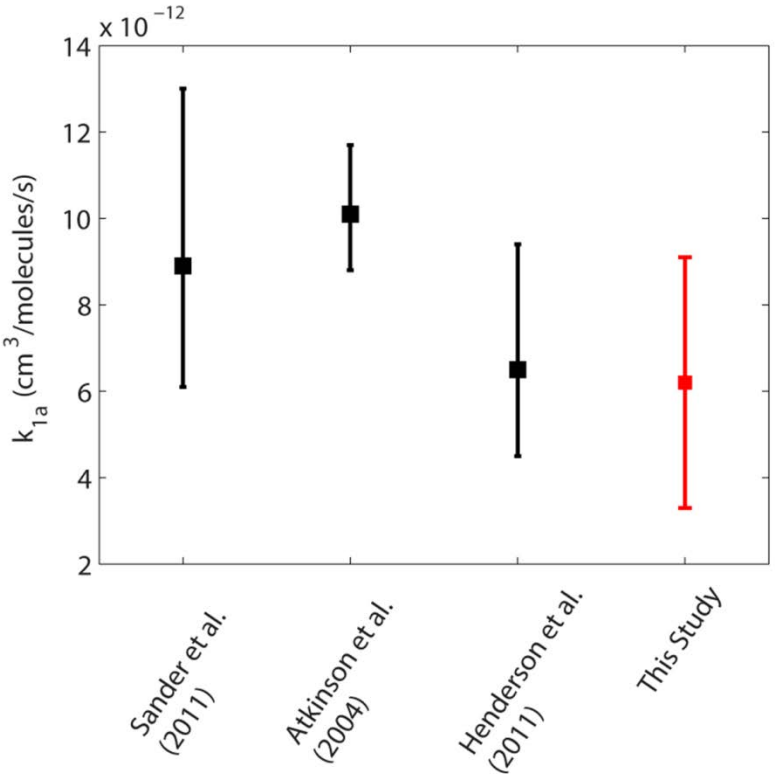

Figure 3.6. Comparison of k_{1a} rate constant at T = 225 K and M = 7.3×10^{18} molecules/cm^3 from Sander et al. (2011), Atkinson et al. (2004), Henderson et al. (2012) and this study (red). The range shows the 2σ uncertainty of the product of the rate constant and branching ratio for HNO_3 formation.

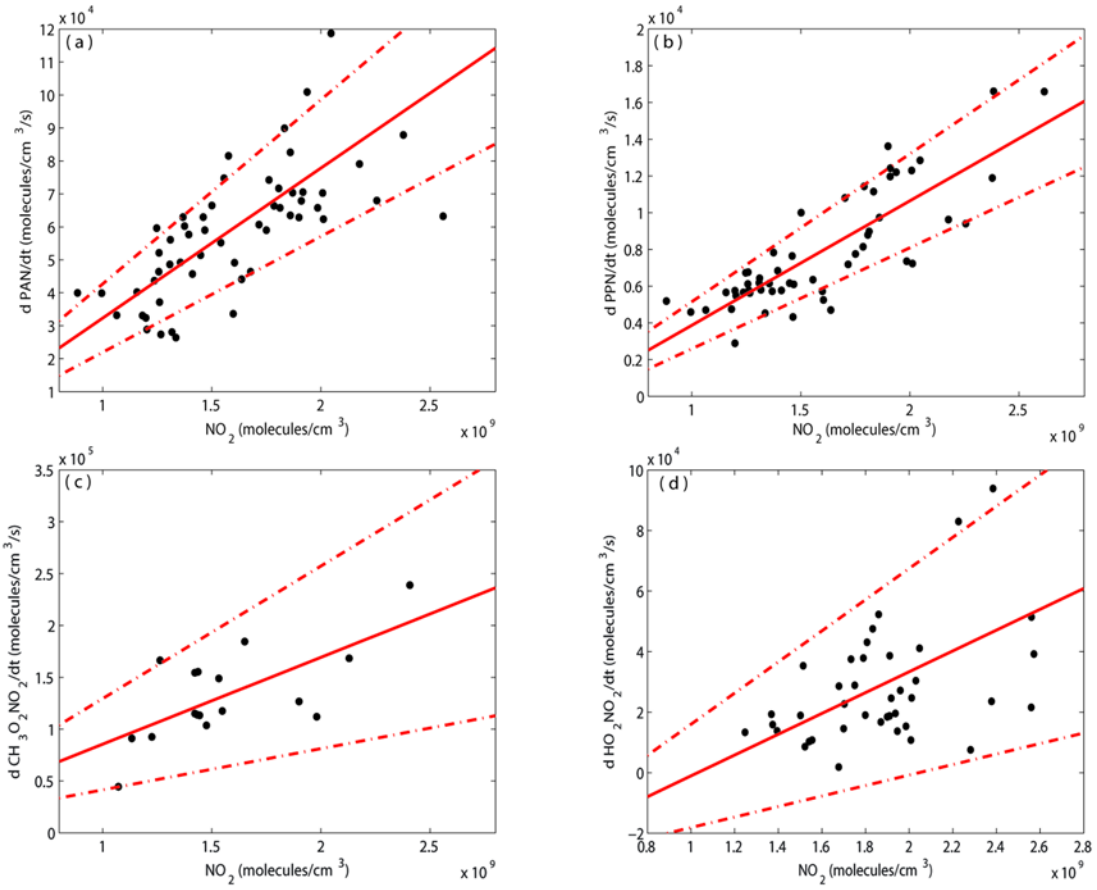

Figure 3.7. The observed **(a)** PAN, **(b)** PPN, **(c)** $CH_3O_2NO_2$, and **(d)** HO_2NO_2 production rate (molecules/cm^3/s) versus NO_2 (molecules/cm^3). The solid red line is the slope and the dashed-dot red lines are the 2σ uncertainty. The slopes are **(a)** $4.5(\pm1.0)\times10^{-5}$ s^{-1}, **(b)** $6.8(\pm1.2)\times10^{-6}$ s^{-1}, **(c)** $8.4(\pm4.8)\times10^{-5}$ s^{-1}, and **(d)** $3.4(\pm1.8)\times10^{-5}$ s^{-1}. For **(c)**, three minute averages are used to reduce the noise of the measurements.

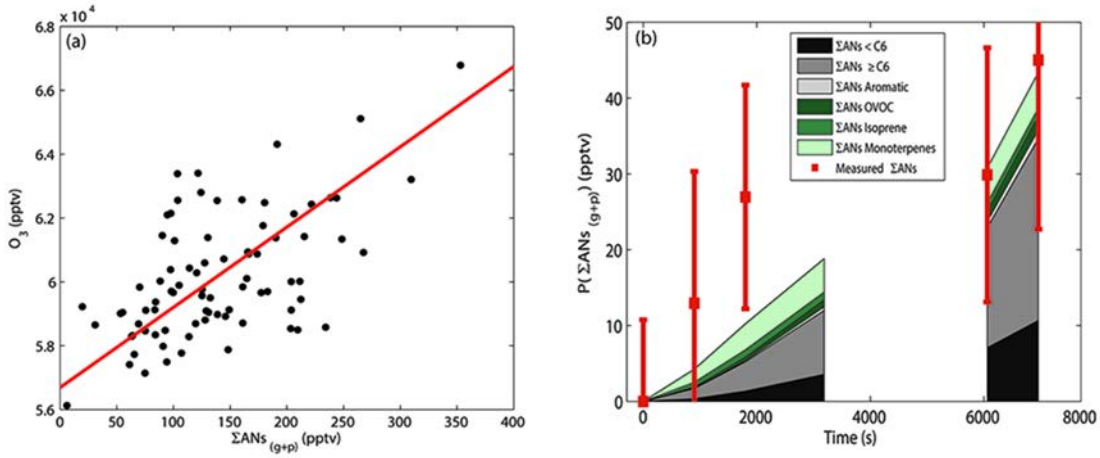

Figure 3.8. (a) The observed O_3 versus $\Sigma ANs_{(g+p)}$ during the flight. The slope (2σ uncertainty) is 25(±6). **(b)** The calculated cumulative production of alkyl and multifunctional nitrates (area plot in pptv) and the 15 minute average (±1σ of the mean) measured production (red error bars in pptv).

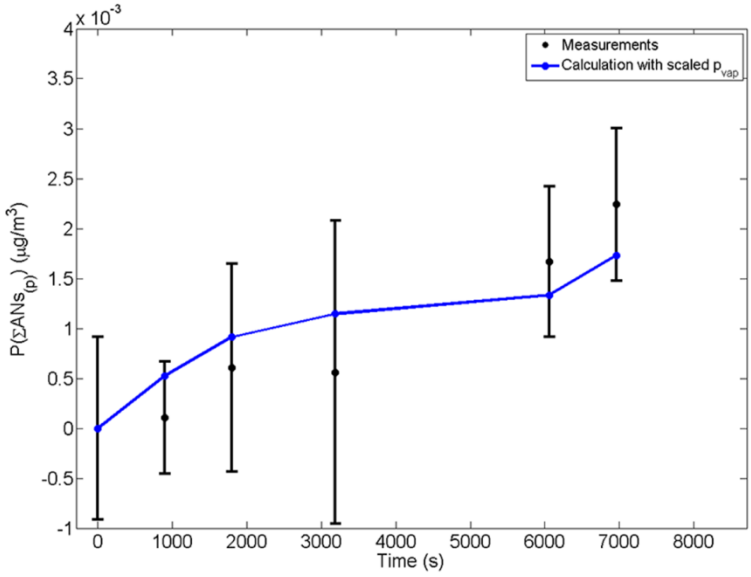

Figure 3.9. The observed (black at ambient T and P) and calculated (blue) cumulative production of the $\Sigma ANs_{(p)}$. The observations are 15 minute averages ($\pm 1\sigma$ of the spread) and the p_{vap} is reduced by a factor of 3.

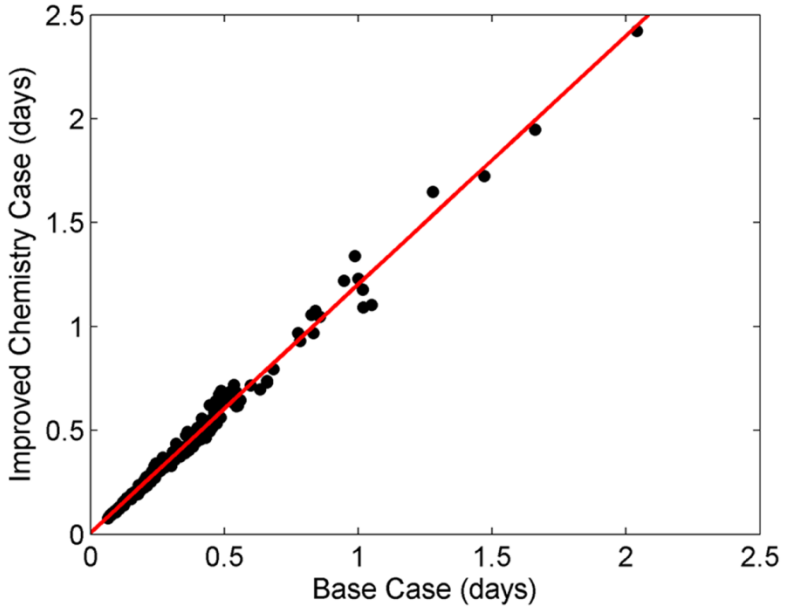

Figure 3.10. Comparison of the NO_x lifetime (NO_x lifetime = NO_x/Loss of NO_x) in the upper troposphere ($T \leq 230$ K) from a steady state model during the entire DC3 campaign. The base case uses the recommended rate constants from Sander et al. (2011) and the updated chemistry case uses the rate constants from Henderson et al. (2012) and Bacak et al. (2011). The slope ($\pm 1\sigma$) is 1.20($\pm$0.01).

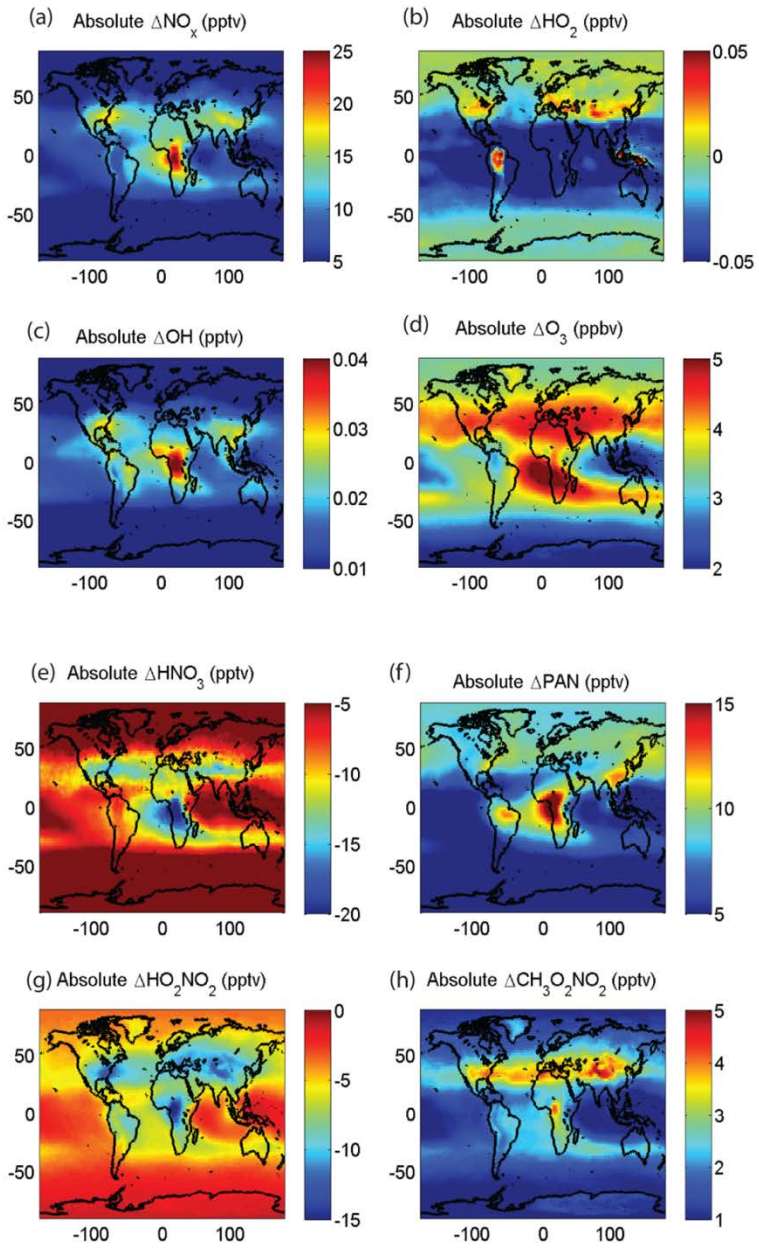

Figure 3.11. The absolute annual mean change in **(a)** NO_x, **(b)** HO_2, **(c)** OH, **(d)** O_3, **(e)** HNO_3, **(f)** PAN, **(g)** HO_2NO_2, and **(h)** $CH_3O_2NO_2$ in the upper troposphere (200 – 400 hPa). The mean change is calculated as (updated chemistry case – base case). Values above the tropopause are removed. Note the different scales for the color bars.

Chapter 4. Impacts of Updated Upper Tropospheric NO_x Chemistry on Lightning NO_x Emission Rates

4.1 Introduction

In the troposphere, NO_x ($NO_x \equiv NO + NO_2$) controls the oxidative capacity and the concentration of ozone, O_3 (Labrador et al., 2004; Labrador et al., 2005; Murray et al., 2013; Liaskos et al., 2015). In the upper troposphere, where O_3 is a powerful greenhouse gas (e.g., Martini et al., 2011; Seltzer et al., 2015), lightning NO_x is the primary source of NO_x (e.g., Schumann and Huntrieser, 2007), and the primary control over O_3 production rates. NO_x produced by lightning accounts for ~10% of the global NO_x input to the atmosphere (Schumann and Huntrieser, 2007). With warming climates, it has been predicted that lightning will increase (e.g., Romps et al., 2014), leading to higher NO_x emission rates.

The type of lightning (cloud-to-cloud versus cloud-to-ground) and location (maritime versus continental) are thought to lead to different lightning energies and thus different lightning NO_x emission rates (Schumann and Huntrieser, 2007 and references therein) and the vertical distribution of lightning NO_x production (e.g., Pickering et al., 1998; Ott et al., 2010). In even the highest resolution atmospheric models, mechanistic representations of lightning NO_x generation is not feasible. Instead, lightning NO_x is parameterized (e.g.,Pickering et al., 1998; DeCaria et al., 2000; DeCaria et al., 2005; Schumann and Huntrieser, 2007; Ott et al., 2010). The parameters carry considerable uncertainty as the limited observational data results in weak tests of the form of the parameterizations and the parameters chosen. Both the emission rate and vertical distribution of lightning NO_x have important impacts for the production and the concentration of upper tropospheric O_3 (Labrador et al., 2005).

Some studies have used direct observations, either *in situ* or by satellite, of NO_x downwind of lightning to calculate the emission rates from individual storms or from the average lightning strikes (e.g., Ridley et al., 1996; Beirle et al., 2004; Huntrieser et al., 2007; Huntrieser et al., 2009; Beirle et al., 2010; Bucsela et al., 2010; Huntrieser et al., 2011). In these studies, the enhancement in NO_x, compared to air not perturbed by lightning, is divided by the lightning flash rate. The results is an empirical estimate of moles of NO produced per lightning flash (mol NO $flash^{-1}$). As many of these studies are well downwind of the cloud, they often make an implicit assumption that the NO_x lifetime is significantly long (longer than 1 day).

To get a larger statistical data base, observations of upper tropospheric NO_x, HNO_3, and O_3 have been used in combination with observations of lightning flash rates to constrain the emission rate parameters in chemical transport models (e.g., Hudman et al., 2007; Martin et al., 2007; Schumann and Huntrieser, 2007; Allen et al., 2010; Jourdain et al., 2010; Martini et al., 2011; Allen et al., 2012; Cooper et al., 2014; Miyazaki et al., 2014; Liaskos et al., 2015). Recent literature has settled on lightning NO_x emission rates in the range of 2 – 8 Tg yr^{-1}, or 500 (260) mol NO $flash^{-1}$ for midlatitude (maritime and tropical) regions (e.g., Martin et al., 2007; Hudman et al., 2007; Schumann and Huntrieser, 2007). The uncertainty in the mol NO $flash^{-1}$ ranges from a factor of 0.13 to 2.7 (Schumann and Huntrieser, 2007; Miyazaki et al., 2014). In many of these studies, the parameterization of lightning NO_x results in model predictions that have less NO_x than observed and more HNO_3 compared to observations (Hudman et al., 2007;

Fang et al., 2010; Martini et al., 2011). HNO_3 is the oxidation product of NO_x and it is reasonable to think of lightning as contributing to the sum of both molecules. Assuming the observations are correct, this discrepancy in the partitioning of NO_x and HNO_3 indicates an error in upper tropospheric NO_x chemistry.

Several recent experiments have suggested changes in the kinetics of nitrogen oxides in the upper troposphere that affect calculations of the rate of conversion of NO_x to HNO_3. These include studies by Browne et al. (2011) and Nault et al. (2015a), who showed that methyl peroxy nitrate, $CH_3O_2NO_2$, chemistry is important to the upper troposphere, and by Henderson et al. (2011), Henderson et al. (2012), Seltzer et al. (2015), and Nault et al. (2015b), who showed that the rate of conversion of NO_2 to HNO_3 is overestimated for the temperatures and pressures characteristic of the upper troposphere. Modeled upper tropospheric NO_x remains largely unaffected because the amount of NO_x sequestered in $CH_3O_2NO_2$ is balanced by the slower conversion to HNO_3 (Nault et al., 2015b).

Another important sink (source) of upper tropospheric NO_x (HNO_3) is hydrolysis of dinitrogen pentoxide, N_2O_5, on aerosol (Jacob et al., 1996; Schultz et al., 1999; Schultz et al., 2000). N_2O_5 is produced at night through the reaction of the nitrate radical, $NO_3^{\bullet}$, with NO_2—lifetime of $NO_3^{\bullet}$ due to photolysis is less than 1 hour making this reaction unimportant during the day. The authors of recent laboratory and ambient observations, at conditions representative of the boundary layer, have concluded the hydrolysis rate constant is at least 1 order of magnitude higher than currently assumed (e.g., Brown et al., 2009; Bertram and Thornton, 2009; Wagner et al., 2013); however, the hydrolysis rate constant has not been studied for the conditions of the upper troposphere. Extrapolating the results from these recent studies would also indicate that the upper tropospheric hydrolysis rate constant should be at least 1 order of magnitude lower (Stavrakou et al., 2013). The lower hydrolysis rate constant would further decrease modeled HNO_3, and this would also impact the interpretation of lightning NO_x emission rates.

In this study, we update the GEOS-Chem model to represent some of these changes in upper tropospheric chemistry—inclusion of $CH_3O_2NO_2$ chemistry and slower HNO_3 production rate constant from the reaction of OH with NO_2. These changes are evaluated to determine how it impacts our interpretation of lightning NO_x emission rates subject to simultaneous constraints of the NO_x and HNO_3 observations. We assess the lightning NO_x emission rate that is consistent with observations and discuss remaining discrepancies between observations and models for upper tropospheric nitrogen oxides.

4.2 Methods

4.2.1 Model Description

GEOS-Chem version 09-02b (Bey et al., 2001; http://geos-chem.org) is used at 2°×2.5° resolution. The standard chemistry and model is described by Mao et al. (2013). Four separate chemistry combinations were analyzed (Table 4.1): one with current recommendations for HNO_3 production rate constant (Sander et al., 2011) and no $CH_3O_2NO_2$ chemistry (Base case, or Case 1), one with current recommendations for HNO_3 production rate constant (Sander et al., 2011) and with $CH_3O_2NO_2$ chemistry (Base case + $CH_3O_2NO_2$, or Case 2), one with 10 – 30% slower

HNO_3 production rate constant (Henderson et al., 2012; Nault et al., 2015b) and no $CH_3O_2NO_2$ chemistry (Slower case, or Case 3), and one with 10 – 30% slower HNO_3 production rate constant (Henderson et al., 2012; Nault et al., 2015b) and with $CH_3O_2NO_2$ chemistry (Slower case + $CH_3O_2NO_2$, or Case 4). We evaluated the model by comparison to observations from *in situ* and space-based platforms. For the case with optimized kinetics, we assessed a range of lightning NO_x parameters to find ones that gave reasonable representations of NO_x and HNO_3 observations (Case 5). Models were allowed to spin-up from January 2011 to December 2011, and, then, the 2012 calendar year was used for analysis. Model output was sampled at 12:00 – 14:00 local standard time for comparison to satellite observations and 16:00 – 20:00 local standard time for comparison with *in situ* observations.

We used the lightning NO_x emissions profile recommended by Pickering et al. (1998). The profile was changed to increase the amount of lightning NO_x produced in the upper troposphere since recent studies (e.g., Allen et al., 2012; Seltzer et al., 2015) concluded that the Ott et al. (2010) profile placed too much NO_x in the middle troposphere and not enough NO_x in the upper troposphere.

We calculate the NO_2 column from the modeled surface to modeled tropopause height to compare to OMI NO_2 tropospheric columns. For the HNO_3, we evaluate the mean HNO_3 mixing ratio from ~ 250 hPa to modeled tropopause height, which corresponds to the peak tropospheric sensitivity of the MLS HNO_3 measurements (e.g., Miyazaki et al., 2014; Cooper et al., 2014). For the comparison to the DC-8 *in situ* observations, the modeled NO_x, HNO_3, and O_3 mixing ratios are averaged between 200 and 350 hPa for the corresponding grid cell and date.

4.2.2 Airborne Observations

Airborne observations from the Deep Convective Clouds and Chemistry (DC3) experiment are used in the analysis. The observations are discussed in detail by Barth et al. (2015). Briefly, the NASA DC-8 aircraft sampled fresh lightning NO_x emissions and the chemical aging of the lightning NO_x emissions, over the continental United States, between May and June, 2012. The observations (DC3 Data Archive) used in this study include NO and O_3 from chemilumiscence (Ryerson et al., 1999), NO_2 from laser-induced fluorescence (Thornton et al., 2000; Nault et al., 2015a), and HNO_3 from mist chamber-ion chromatography (Talbot et al., 1997) and chemical ionization-mass spectrometry (Crounse et al., 2006). We take the average of the two HNO_3 measurements for this study since there was a 10% difference between the two measurements (Nault et al., 2015b). The observations used to compare to the GEOS-Chem output are constrained between 200 and 350 hPa with O_3/CO less than 1.5 (removes stratospheric influences) and NO_x/HNO_3 less than 5 (removes fresh lightning NO_x emissions). A minimum of 10 1-minute averaged observations are required to ensure enough spatial coverage of the 2°×2.5° grid cell. Only observations with a NO_x/HNO_3 ratio less than 5 are used since higher ratios are associated with the near field of convective emissions and the large model grid cell size dilutes fresh lightning NO_x emissions (e.g., Cooper et al., 2014). During DC3, 30% of upper tropospheric (P = 200 – 350 hPa) observations had NO_x/HNO_3 ratios greater than 5, which cannot be captured by GEOS-Chem at this spatial resolution since the convective spatial scale during DC3 was significantly smaller GEOS-Chem.

4.2.3 Satellite Observations

The Ozone Monitoring Instrument (OMI) aboard the NASA Aura satellite is used and is described in detail by Levelt et al. (2006). The UV/Vis spectrometer observes solar irradiance and sunlight reflected from Earth's surface in the 270 – 500 nm wavelength range. The instrument, with a field of view of 2600 km swath with a ground pixel size between 13 × 24 km^2 at nadir to 24 × 128 km^2 at the edge of the swath, achieves near global coverage daily with an overpass time at approximately 13:40 local time. There are currently two products for global NO_2 column densities for OMI—the NASA Standard Product 2 (Bucsela et al., 2013) and the Dutch OMI NO_2 (DOMINO) Product (Boersma et al., 2011). The Level 3 daily gridded NASA Standard Product (OMNO2d) is used here (Krotkov). Since no matching daily product is available for DOMINO, the ungridded Level 2 product was used. Prior studies (e.g., Lamsal et al., 2010; Russell et al., 2011) have indicated that the two products can disagree by 20 – 40%; therefore, we take the average of the two products for this study. For both products, observations are first filtered for the presence of clouds and the effects of the row anomaly. Pixels with a cloud fraction greater than 30% are removed. The row anomaly is an obstruction that affects the observed radiances of ~20 rows of pixels on the OMI instrument. The affected pixels are flagged in both products and are removed. Pixels are matched to GEOS-Chem grid cells if the pixel center falls within the grid cell, and a weighted average of all such observations is taken. The weight used is provided in the OMNO2d product and described in the OMNO2d readme (http://disc.sci.gsfc.nasa.gov/Aura/data-holdings/OMI/documents/v003/OMNO2_readme_v003.pdf). For the DOMINO product, the weight for each pixel is calculated as the reciprocal of the area. This gives the greatest weight to near-nadir pixels that are most representative of the area of interest (http://disc.sci.gsfc.nasa.gov/Aura/data-holdings/OMI/documents/v003/OMNO2_readme_v003.pdf)

To minimize the influence of surface NO_x sources (soil, anthropogenic, and biomass burning), which cannot be easily separated from lightning NO_x emissions from a total column nadir satellite observation, we focus on regions where the model predicts the lightning NO emissions are more than 60% of the NO_x source. Observations over South America, Northern Africa, Southern Africa, and Southeast Asia (Table 4.2) during their summer months meet this criterion.

4.3 Sensitivity in modeled NO_2 and HNO_3 from lightning emissions

4.3.1 Changes in NO_2 column densities

$CH_3O_2NO_2$ chemistry (Case 2 – Case 1) decreases the average NO_2 column density between -0.2 to 0×10^{14} molecules/cm^2 (−2 to 0% change), with an average change of -0.08×10^{14} molecules/cm^2 (−1% change), during the months of June through August (Fig. 4.1). The most negative changes occur in the southeastern United States, where the most lightning flashes occur along with injection of isoprene and isoprene products, which undergoes photooxidation to produce methyl peroxy radicals, $CH_3O_2^{\bullet}$, the precursor to $CH_3O_2NO_2$ (Hudman et al., 2007; Martini et al., 2011; Apel et al., 2012; Barth et al., 2015). Since $CH_3O_2NO_2$ chemistry is important as temperature decreases and the $CH_3O_2NO_2$ lifetime maximizes where the lightning NO_x emission rate is maxima in the upper troposphere (Pickering et al., 1998; Browne et al.,

2011; Nault et al., 2015a), the inclusion of $CH_3O_2NO_2$ chemistry strongly impacts and removes NO_x emitted by lightning NO_x production. The small decrease in the column density results from adding another NO_x sink; however, $CH_3O_2NO_2$ is only important as a NO_x sink at temperatures less than 255 K (Browne et al., 2011; Nault et al., 2015a). At these low temperatures, NO constitutes a large fraction of the NO_x budget due to the temperature dependent conversion of NO to NO_2 (e.g., Schumann and Huntrieser, 2007); therefore, the impact to the total NO_2 column density is small.

The inclusion of slower HNO_3 production rate constant (Case 3 – Case 1) increases the averaged NO_2 column density by 0.5 to 3×10^{14} molecules/cm^2 (6 – 16% increase), with an average of 1.3×10^{14} molecules/cm^2, or 12% increase (Fig. 4.1). The largest increases are located both in areas of high surface emissions from urban (e.g., Chicago area) or agricultural regions (e.g., central United States, Hudman et al., 2010) and high lightning flash rates (e.g, southeastern United States). The increase in the NO_2 column density stems from increasing the NO_x lifetime throughout the entire column; however, the change in the NO_x lifetime is smallest near the surface (~10%) while it is largest near the tropopause (~40%; Mollner et al., 2010; Henderson et al., 2012).

When $CH_3O_2NO_2$ chemistry and slower HNO_3 production rate constants are both included (Case 4 – Case 1), the NO_2 column density increases by nearly the same amount as Case 3 – Case 1. Small differences of order 10% are found in southeastern United States, where there is lightning and $CH_3O_2^{\bullet}$ precursors are collocated. The net changes in the column NO_2 density due to updating upper tropospheric NO_x chemistry are small, and would not impact the interpretations of prior studies of lightning NO_x.

4.3.2 Changes in upper tropospheric HNO_3 mixing ratios

Unlike the changes in the NO_2 column densities, all Cases (2 through 4) – Case 1 show a net decrease in averaged upper tropospheric HNO_3 mixing ratios (Fig. 4.1). The smallest decrease occurs for Case 2 – Case 1 (average decrease is −22 pptv or −5%). In this instance, including $CH_3O_2NO_2$ removes a source of NO_x that would otherwise be oxidized to produce HNO_3. The small change is similar to the results from Browne et al. (2011), where they found a decrease in upper tropospheric HNO_3 of 15 to 40 pptv in a model with versus a model without $CH_3O_2NO_2$ chemistry. The largest decrease occurs for Case 4 – Case 1 (average decrease is −71 pptv or −20%). Here, both the extra sink of NO_x, $CH_3O_2NO_2$, and decreasing the production of HNO_3 by using a lower rate constant reduces the upper tropospheric HNO_3 mixing ratios. Similar to the changes in the NO_2 column densities, the largest changes occur over areas of higher lightning flash rates. The decreases in modeled upper tropospheric HNO_3 are large and important as this compound has established the maximum lightning NO_x emission rates consistent with observations in prior studies (e.g., Hudman et al., 2007; Fang et al., 2010; Martini et al., 2011; Cooper et al., 2014).

4.3.3 Changes in other regions of the world

The sensitivity of the modeled tropospheric NO_2 column density and upper tropospheric HNO_3 mixing ratios to different chemistry cases (Table 4.1) were evaluated over North America during

the months of June through August. For other regions of the world (Table 4.2), the sensitivity of the modeled tropospheric NO_2 column density (Fig. 4.2) and upper tropospheric HNO_3 mixing ratios (Fig. 4.3) were investigated for Case 1 versus Case 4 (Table 4.1) for the respective summer months of those regions—June through August for Northern Africa and Southeast Asia and December through February for Southern Africa and South America.

Similar to North America, there are net increases in the NO_2 column densities that range from 0 – 1.9×10^{14} molecules/cm^2 over the different regions (Fig. 4.2). The mean percent (absolute) change for the different regions is less than North America, at 6% (3×10^{13} molecules/cm^2) for South America and 9% for the other regions (6.2×10^{13}, 3.9×10^{13}, and 5.9×10^{13} molecules/cm^2 for Northern Africa, Southeast Asia, and Southern Africa, respectively). These regions are considered tropical or marine for the lightning NO_x emission parameterizaton. These regions typically have lower mol NO flash^{-1} than midlatitude regions (North America) since the energy per lightning flash is lower (Pickering et al., 1998; Ott et al., 2010). The lower lightning NO_x production rate leads to lower changes in the NO_2 column density compared to North America.

With the lower mol NO flash^{-1}, the modeled absolute mean HNO_3 changes were smaller than over North America—−48, −22, −63, and −54 pptv for Northern Africa, Southeast Asia, Southern Africa, and South America, respectively. The smallest change occurs over Southeast Asia. Cooper et al. (2014) determined that models have too low lightning NO_x emission rates over Southeast Asia when the authors compared modeled HNO_3 to *in situ* and satellite observations. Similar to North America, the changes are negative and large (mean percent change is 20%). These large changes thus have impacts on the established maximum lightning NO_x emission rates.

4.4 Implications for lightning NO_x emission rates

4.4.1 Comparison to upper tropospheric observations during DC3

In Fig. 4.4, we compare the modeled-to-observed ratios for upper tropospheric NO_x and HNO_3 from two prior studies (Hudman et al., 2007; Martini et al., 2011) with the modeled-to-observed results from Case 1, Case 4, and Case 5 (Table 4.1) during DC3. For the two prior studies, the modeled NO_x mixing ratios are biased low compared to observations, and modeled HNO_3 mixing ratios are biased high compared to observations. The increases in NO_x and HNO_3 between Hudman et al. (2007) and Martini et al. (2011) stems from using observations to prescribe the location and intensity of lightning flash rates rather than increasing the NO mol flash^{-1}. Models now use observed flash rates since the models typically did not correctly locate the lightning or its intensities (e.g., Hudman et al., 2007; Murray et al., 2012).

Similar to the two prior studies, the Case 1 ratios for NO_x and HNO_3 have similar discrepancies, indicating a consistent bias in the description of the upper tropospheric NO_x chemistry (Henderson et al., 2011). By updating the upper tropospheric NO_x chemistry (Case 4), the modeled-to-observed ratios for HNO_3 decreases by 15% from 1.45 to 1.23, showing better agreement. The NO_x ratio changes are 1% or 0.78 to 0.79. The small change in NO_x is due to $CH_3O_2NO_2$ removing the excess NO_x that was available from the slower HNO_3 production rate (Fig. 4.1).

Since chemistry alone does not improve the NO_x modeled-to-measured agreement, as suggested by Henderson et al. (2011), we investigate if updating the chemistry along with increasing lightning NO_x emission rates results in better agreement. Many studies have suggested that increasing lightning NO_x emission rates would be necessary for better agreement between observed and modeled upper tropospheric NO_x (Allen et al., 2010; Jourdain et al., 2010; Martini et al., 2011; Liaskos et al., 2015); however, a typical constraint for increasing lightning NO_x emission rates is the agreement of modeled and observed HNO_3. For example, in Martini et al. (2011), the authors found that increasing the lightning NO_x emission of their model from 240 to 480 mol NO $flash^{-1}$ led to lower biases between measured and modeled NO_x; however, the increase in lightning NO_x emissions increased the bias between measured and modeled HNO_3 (Fig. 4.4). Similarly, the lightning NO_x emission recommended by Hudman et al. (2007) was tuned so that the modeled HNO_3 was slightly higher than the upper 1σ spread of the measurements whereas the modeled NO_x just agreed with the lower 1σ spread of the measurements (Fig. 4.4). When the lightning NO_x emissions for Case 1 were increased by 33% to compare against the DC3 observations, the NO_x ratio improved to 0.92, but the HNO_3 ratio increased to 1.70 (not shown). This HNO_3 ratio is well above the 1σ spread of the HNO_3 observations (Fig. 4.4).

We find that increasing the lightning NO_x emission rates by 33%, with the updated chemistry (Case 4), led to the best agreement between observed and modeled NO_x and HNO_3 during the DC3 mission. The NO_x ratio increases to 0.96 while the HNO_3 ratio increases 1.45.

The NO_x to HNO_3 ratios can also be utilized to improve our understanding of upper tropospheric NO_x chemistry and the time since an air mass has been impacted by lightning NO_x emissions (Bertram et al., 2007; Henderson et al., 2011). Higher ratios indicate fresh emissions due to lightning NO_x emissions and rain-out of HNO_3 while lower ratios represent aged air from the chemical conversion of NO_x to HNO_3. Comparison of observations to Case 1, which has a smaller range of NO_x/HNO_3 than observation, indicates the modeled air is older (lower ratios) than observations. It also further proves that the current model does not accurately describe NO_x chemistry and lightning NO_x emission rates (Fig. 4.5). Using updated chemistry (Case 4) has a larger range of NO_x/HNO_3 than Case 1; however, the model still calculates older (lower ratios) air than observations. The updated chemistry with increased lightning NO_x emission rates (Case 5), though, shows a similar range as Case 4. This results from the model producing too much HNO_3 even though the model better represents NO_x (Fig. 4.4). Lower modeled HNO_3 would increase the ratio, resulting in the model calculating fresher air that we observed during DC3.

This bias in HNO_3 suggests that either the loss processes—uptake to cloud particles, uptake to aerosols, photolysis, photooxidation of HNO_3, or transport from upper troposphere—are too low or production—hydrolysis of N_2O_5 on aerosols or transport into upper troposphere—is too high. As previously mentioned, the hydrolysis rate constant is likely an order of magnitude too high. Over North America during summer, the 24 hour averaged N_2O_5 mixing ratio increases by 38% from Case 1 to Case 5. Using the averaged N_2O_5 mixing ratios between 01:00 and 03:00 local time from Case 5, spatially coincident with DC3 observations, a correlation between higher 1 hr N_2O_5 hydrolysis production rates and too high modeled HNO_3 compared to observations is apparent while there is no correlation between too high modeled HNO_3 and the HNO_3 production rate from the reaction of OH with NO_2 (Fig. 4.6). This suggests that the modeled N_2O_5

hydrolysis rate is too fast. Assuming N_2O_5 mixing ratios remain constant during night, the 1 hr production rates result in 40 – 110 pptv HNO_3 (assuming an 8 – 12 hr night). This would explain a large fraction of the averaged difference between modeled and observed HNO_3 (160 pptv). Assuming that the rate is at least one order of magnitude too high (e.g., Brown et al., 2009), the amount of HNO_3 produced decreases to 4 – 11 pptv, which would bring the modeled and observed HNO_3 into better agreement.

4.4.2 Comparisons to satellite observations

Comparison of modeled NO_2 column densities with satellite observations indicate that, in general, the updated chemistry improves the agreement between model and observations and that increased lightning NO_x emission rates are necessary to further reduce the average bias between model and observations (Table 4.3). In Southeast Asia and South America, the comparison indicates that the lightning NO_x emissions could increase even more than done in this study to reduce the bias, which is in agreement with the conclusion of Cooper et al. (2014) and comparison of satellite NO_2 observations with modeled results from Liaskos et al. (2015). However, in South Africa, the negative bias at higher lightning NO_x emission rates means that the current lightning NO_x emissions properly describe the observations. These differences in the biases for different regions agree with the conclusion from Cooper et al. (2014) that the lightning NO_x emission rates for different regions are not uniformed even though current models assume the same mol NO flash^{-1} for similar regions. The authors in this study concluded, using Case 1 chemistry and HNO_3 satellite observations, that Southeast Asian lightning NO_x emissions need to increase whereas the other regions of the world has the correct lightning NO_x emission rates. By updating the upper tropospheric NO_x chemistry, this leads to other locations also needing higher lightning NO_x emission rates, similar to the comparison to the DC3 observations in the prior section.

A similar comparison with satellite HNO_3 observations was not done. Various studies have indicated inconsistent biases and little correlation between satellite observations with *in situ*, or other satellite observations, of upper tropospheric HNO_3 (Froidevaux et al., 2006; Santee et al., 2007; Kinnison et al., 2008; Wolff et al., 2008; Cooper et al., 2011). These inconsistencies for all the HNO_3 satellite observations would not provide valuable constraints on whether the inclusion of updated chemistry and increased lightning NO_x emission rates in the model correctly depict observations.

4.4.3 Impacts of shorter NO_x lifetime on direct lightning NO_x observations

As previously mentioned, an assumption to calculate mol NO flash^{-1} directly from observations (*in situ* or satellite) is that the NO_x lifetime is sufficiently long—greater than 1 day. Nault et al. (2015b) showed that the NO_x lifetime directly downwind of lightning is typically shorter than 1 day due to production of peroxy nitrates and nitric acid. With many observations occurring typically occurring ~3 hours after the lightning flash (e.g., Huntrieser et al., 2007; Beirle et al., 2010; Huntrieser et al., 2011), the lifetimes found in Nault et al. (2015b) indicates that approximately 10 – 70% of the NO_x is chemically removed prior to sampling. Due to this assumption, many of the *in situ* and remote sensing studies that directly measure the lightning

NO_x emission rates are lower, by 3 to 100%, than the studies that use *in situ* or satellite observations with chemical transport models (Miyazaki et al., 2014).

As an example, Beirle et al. (2004) calculated a lightning NO_x emission rate of 100(30 – 500) mol NO_x flash^{-1} over Australia, a region classified as tropical in GEOS-Chem (corresponds to 260 mol NO flash^{-1}). The average value from this study is 60 – 80% lower than the currently accepted average values of 260 – 500 mol NO flash^{-1}. In this study, the authors assumed a NO_x lifetime of 2 – 6 days. If the lifetime is reduced to 0.5 days, the mean lifetime observed by Nault et al. (2015b), the emission rate increases to 750(250 – 1000) mol NO_x flash^{-1}. Using the shorter lifetime indicates and agrees with lightning NO_x emission rates should increase by at least 33%. Even if a lifetime of 1 day is assumed, the emission rate increases to 370(125 – 500) mol NO_x flash^{-1}, which is still in agreement with higher emission rates.

4.4.4 Impacts on O_3

Similar to recent studies (e.g., Martini et al., 2011; Liaskos et al., 2015), Case 1 model calculates higher O_3 than measured during DC3 by nearly 16% (Fig. 4.7a). Using the improved NO_x chemistry and increasing lightning NO_x emission rates (Case 5), the modeled O_3 only increases by 5%, but this leads to a 21% discrepancy between observations and model results. This indicates, similar to the HNO_3 comparison, that the modeled loss or production processes for upper tropospheric O_3 does not properly describe the chemistry. An important control on the O_3 production is NO_x and water vapor concentration. An increase of water vapor with high NO_x concentration leads to more photooxidation of hydrocarbons, which increases the radical cycling to produce more O_3 (Klonecki and Levy, 1997). Sauvage et al. (2007) found that an update to meteorological fields increased the amount of water in the upper troposphere. This led to higher modeled upper tropospheric O_3 mixing ratios. For this study, the modeled water vapor mixing ratio is higher than observed at high NO_x mixing ratios (Fig. 4.8); therefore, we conclude the higher modeled water vapor in the presence of high NO_x and hydrocarbons from deep convection has led to higher modeled than observed O_3 mixing ratios in Fig. 4.7a.

For the entire year, the percent increase over various regions of the world are typically less than 10% after incorporating updated chemistry and increasing lightning NO_x emission rates (Fig. 4.7b). The only region with a change larger than 10% is Southeastern Asia. The percent changes in O_3 in Fig. 4.7b are smaller than the percent changes observed in prior studies after increasing lightning NO_x emission rates (e.g., Martini et al., 2011; Liaskos et al., 2015). The smaller decreases in O_3 in this study stem from the removal of NO_x from $CH_3O_2NO_2$ production (Browne et al., 2011) that competes with longer NO_x lifetime from slower HNO_3 production (Seltzer et al., 2015). The incorporation of the improved upper tropospheric NO_x chemistry minimizes the gross error in modeled O_3 concentrations for gross lightning NO_x emission rates greater than 8 Tg N yr^{-1} that Martin et al. (2007) predicted could occur.

4.5 Conclusions

We have incorporated updated upper tropospheric NO_x chemistry into the GEOS-Chem global chemical transport model to investigate the impact on lightning NO_x emission rates. Including

$CH_3O_2NO_2$ chemistry and slower daytime HNO_3 production rate from the reaction of OH with NO_2 decreases modeled upper tropospheric HNO_3 mixing ratios as much as 71 pptv over North America while minimally impacting modeled upper tropospheric NO_2 column densities. The decrease in modeled upper tropospheric HNO_3 is significant as this value has been typically used to constrain modeled lightning NO_x emission rates, and these lightning emission rates have largely underestimated observed upper tropospheric NO_x mixing ratios. With the updated chemistry, we find that increasing the lightning NO_x emission rates by 33% better simulates the observed upper tropospheric NO_x mixing ratios compared to observations during the DC3 airborne campaign. Comparison to satellite observations indicates that the lightning NO_x emission rate is variable, depending on the location, similar to the conclusion of Cooper et al. (2014). Most regions need at least a 33% increase in lightning NO_x emission rates to agree with observations. Sources of modeled HNO_3 and O_3 higher than observations are explored after increasing lightning NO_x emission rates, and we suggest that N_2O_5 hydrolysis rates to produce HNO_3 and too high modeled water vapor mixing ratios, which promotes O_3 production, lead to the disagreement between observations and models.

Table 4.1. Description of the different chemical sensitivity cases used in this study.

Case	Name	Description
1	Base case	Sander et al. (2011) recommended OH + NO_2 rate constant to produce HNO_3 without $CH_3O_2NO_2$ chemistry
2	Base case + $CH_3O_2NO_2$	Sander et al. (2011) recommended OH + NO_2 rate constant to produce HNO_3 with $CH_3O_2NO_2$ chemistry
3	Slower case	Henderson et al. (2012) recommended OH + NO_2 rate constant to produce HNO_3 without $CH_3O_2NO_2$ chemistry
4	Slower case + $CH_3O_2NO_2$	Henderson et al. (2012) recommended OH + NO_2 rate constant to produce HNO_3 with $CH_3O_2NO_2$ chemistry
5	Increased lightning NO_x emission rates	Case 4 with 33% increased lightning NO_x emission rate

Table 4.2. Coordinates of the different regions used in this study.

Region	Longitude	Latitude
North America	120 – 65°W	20 – 60°N
South America	77 – 39°W	35°S – 10°N
Northern Africa	15°W – 48°E	3 – 25°N
Southern Africa	10 – 48°E	30°S – 3°N
Southeast Asia	95 – 146°E	9°S – 26°N

Table 4.3. Percent biases of the NO_2 column density from the averaged OMNO2d and DOMINO product over South America, Northern Africa, Southern Africa, and Southeast Asia during their respective summer months (June – August for Northern Africa and Southeast Asia and December – February for South America and Southern Africa). The Cases are defined in Table 4.1. The percent mean bias is calculated as (observations – Case 5)/observations × 100.

	% Mean Bias NO_2 Column Density		
	Case 1	Case 4	Case 5
South America	41	38	25
Northern Africa	16	9	−5
Southern Africa	4	−4	−22
Southeast Asia	48	44	39

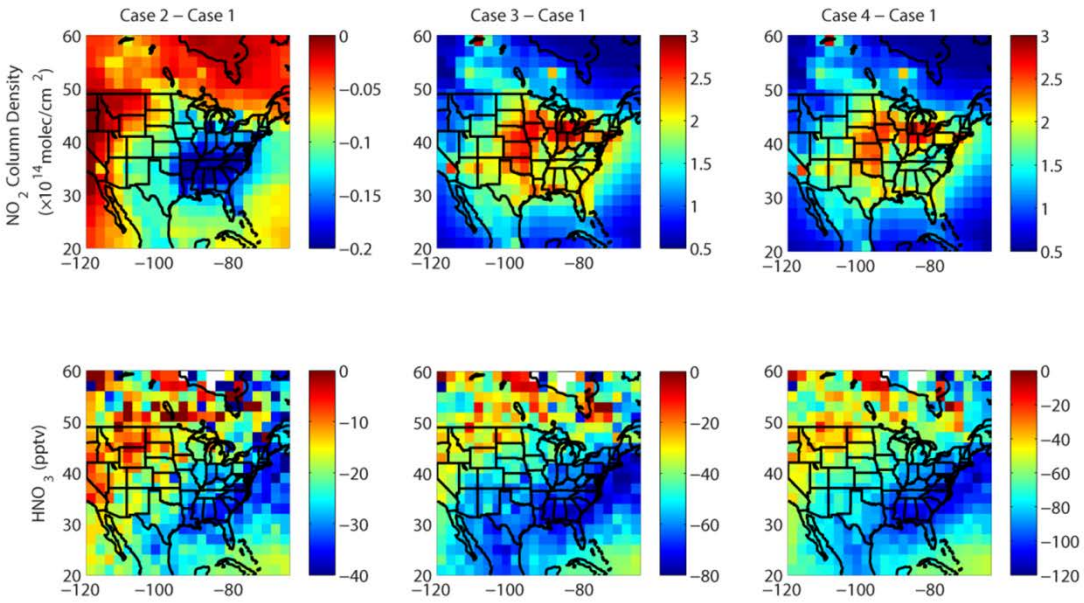

Figure 4.1. Changes in modeled NO_2 column density ($\times 10^{14}$ molec./cm^2, first row) and upper tropospheric HNO_3 mixing ratios (pptv, second row) between Case 1 and Case 2 (first column), Case 3 (second column) and Case 4 (third column). Description of each case is found in Table 4.1. Note the differences in scale for each figure.

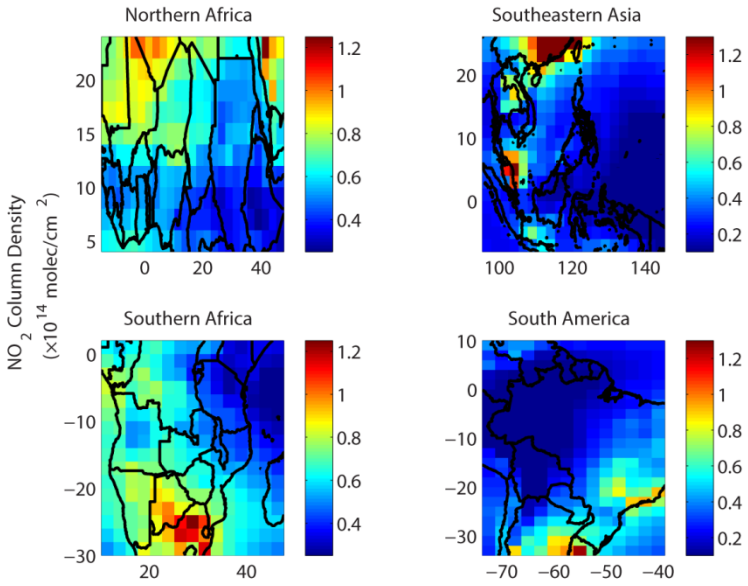

Figure 4.2. Changes in modeled NO_2 column density ($\times 10^{14}$ molec./cm^2) between Case 1 and Case 4 for Northern Africa, Southeastern Asia, Southern Africa, and South America. The changes correspond to the months June through August for Northern Africa and Southeastern Asia and December through February for Southern Africa and South America. Description of each case is found in Table 4.1 and definitions of the regions are found in Table 4.2. Note the differences in scale for each figure.

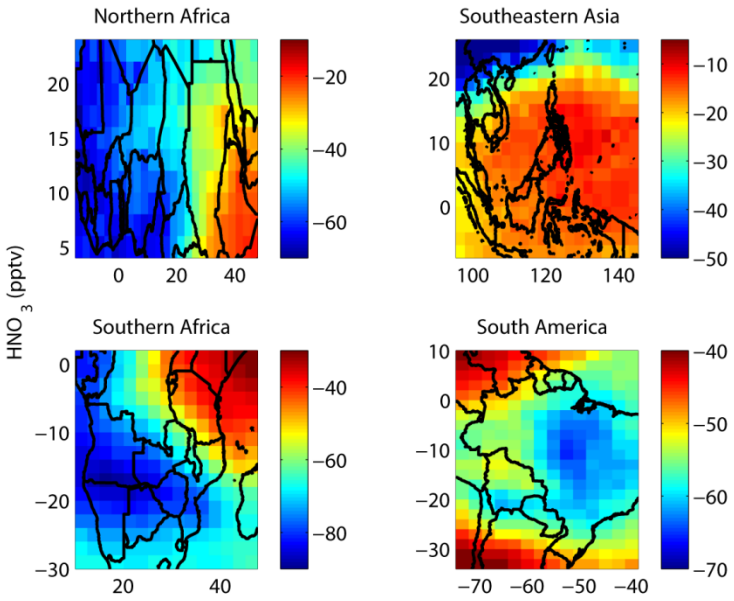

Figure 4.3. Changes in modeled upper tropospheric HNO_3 mixing ratios (pptv) between Case 1 and Case 4 for Northern Africa, Southeastern Asia, Southern Africa, and South America. The changes correspond to the months June through August for Northern Africa and Southeastern Asia and December through February for Southern Africa and South America. Description of each case is found in Table 4.1 and definitions of the regions are found in Table 4.2. Note the differences in scale for each figure.

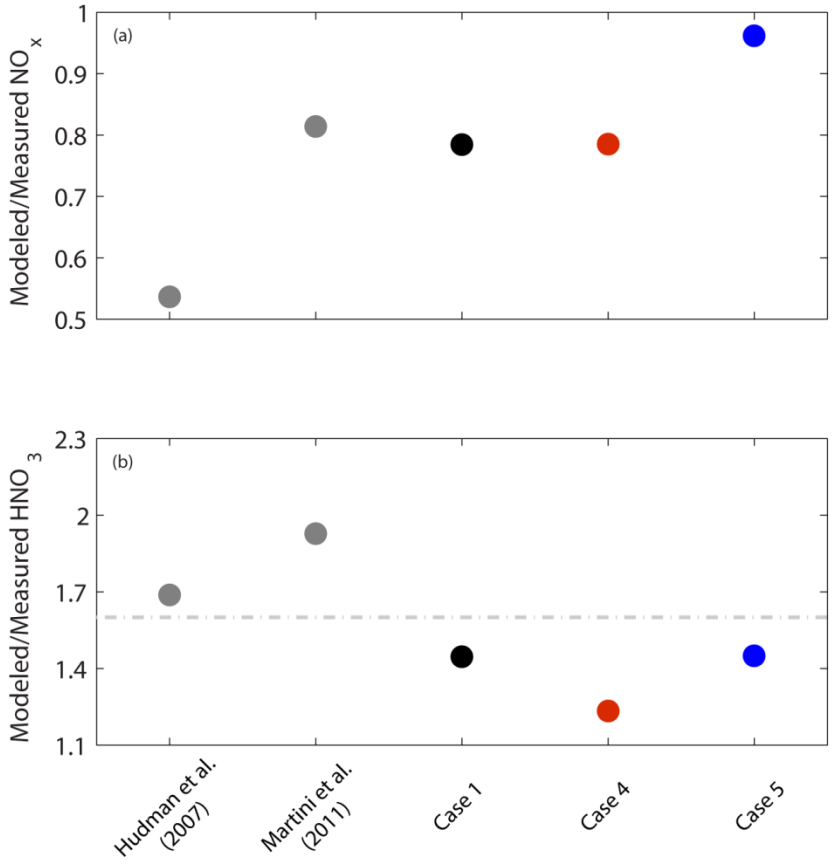

Figure 4.4. Comparison between modeled and measured ratio of upper tropospheric **(a)** NO_x and **(b)** HNO_3. Values reported from Hudman et al. (2007) and Martini et al. (2011) are shown in dark grey as comparison to the values from Case 1 (black), Case 4 (red) and Case 5 (blue). Description of the cases is found in Table 4.1. The light grey dashed-dot line in **(b)** represents the upper 1σ of observations during DC3. Note, the measured NO_x and HNO_3 from Hudman et al. (2007) and Martini et al. (2011) are adjusted as recommended by Browne et al. (2011) and Bertram et al. (2007), respectively, assuming the upper limit that 35% of the NO_2 signal is thermally decomposed $CH_3O_2NO_2$.

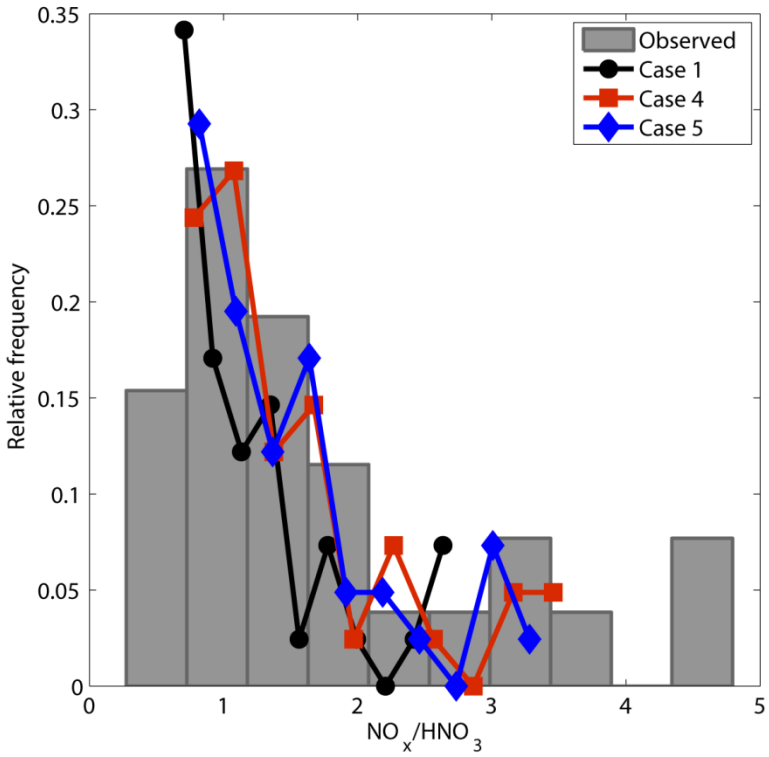

Figure 4.5. Relative frequency of NO_x/HNO_3 ratios observed during DC3 (grey bars) and calculated in Case 1 (black line), Case 4 (red line) and Case 5 (blue line) models.

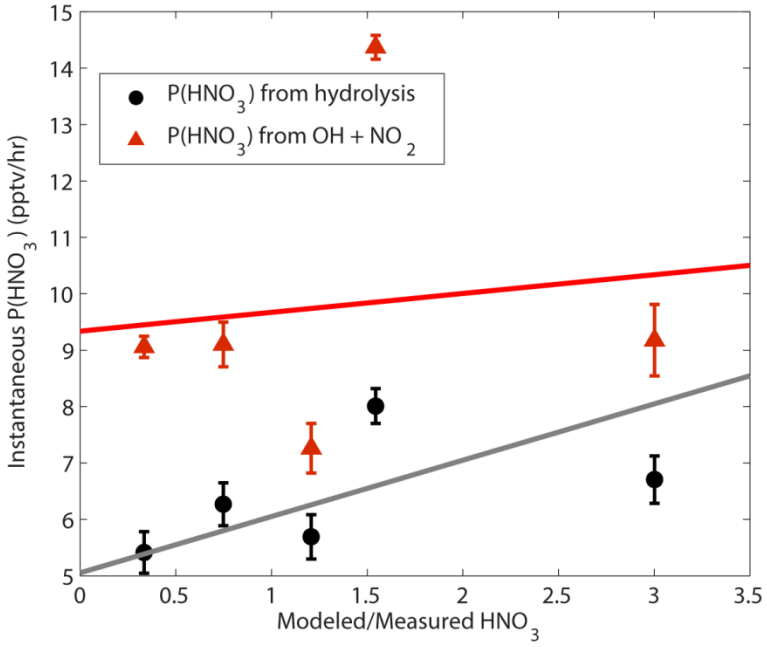

Figure 4.6. Mean binned scatter plot of instantaneous 1 hr HNO_3 production rate (pptv/s) from modeled N_2O_5 hydrolysis (black) and modeled reaction of OH with NO_2 (red) versus the modeled-to-measured ratio from DC3 observations. The bars represent 1σ standard deviation about the mean of the production. A hydrolysis rate of 4×10^{-5} s^{-1} (Evans and Jacob, 2005) is assumed, and the slower OH and NO_2 rate constant (Henderson et al., 2012) is used. The R^2 for the grey (N_2O_5 hydrolysis) and red (OH with NO_2 reaction) is 0.23 and 0.02, respectively.

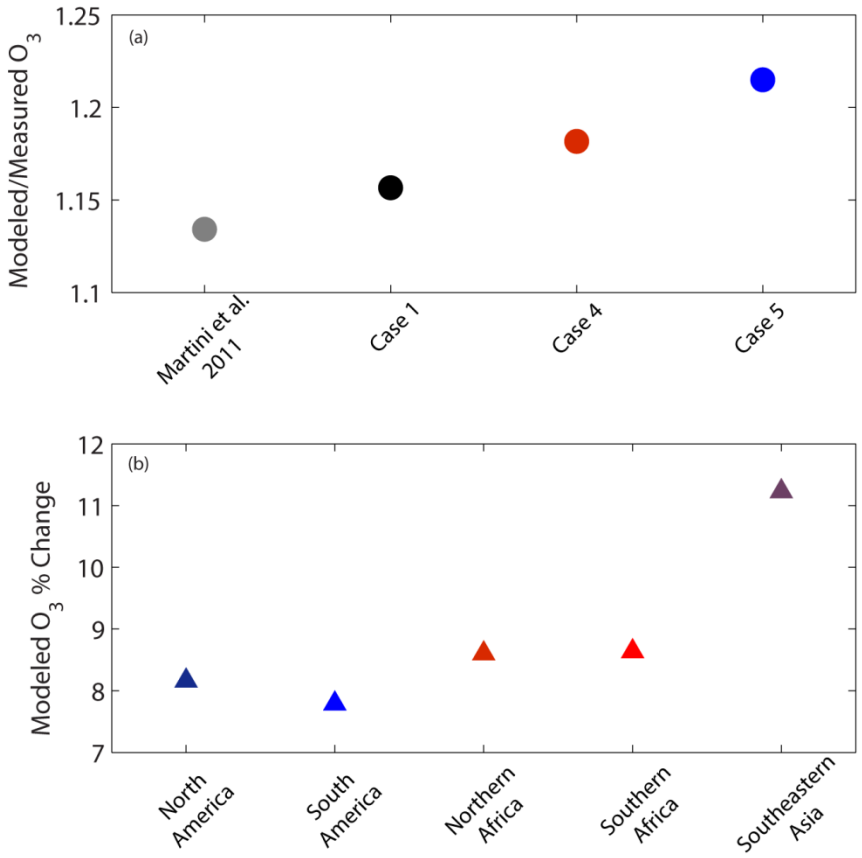

Figure 4.7. Comparison between modeled and observed O_3 during DC3 **(a)**. Modeled annually averaged percent in upper tropospheric (350 hPa – tropopause) O_3 concentration, by region, between Case 1 and Case 5, where percent change is (Case 5 – Case 1)/Case 1 × 100.

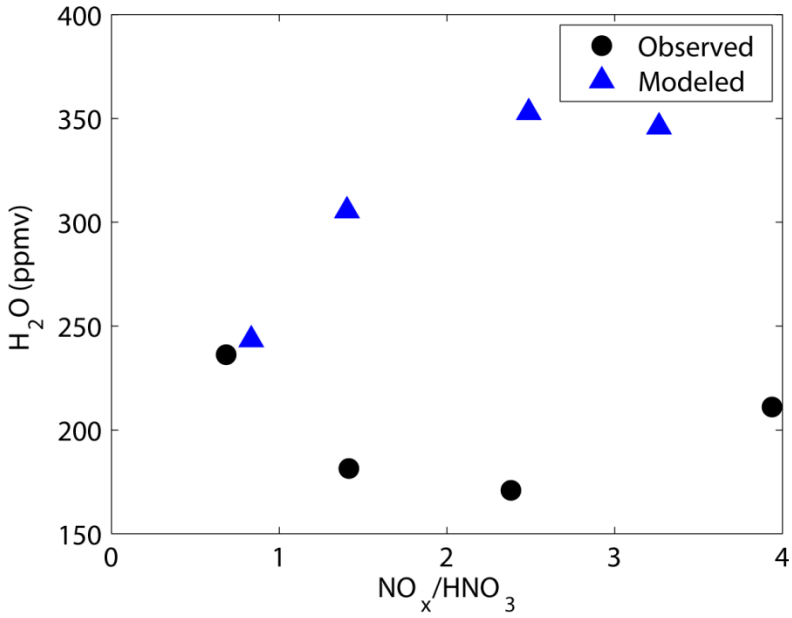

Figure 4.8. Binned mean observed (black) and modeled (blue) upper tropospheric (200 – 350 hPa) versus relative age of air mass (NO_x/HNO_3).

Chapter 5. Conclusions

The chemistry of the upper troposphere controls O_3 production rates, an important greenhouse gas. Understanding the chemistry, including the rate constants and the reaction products, in this remote region of the atmosphere is challenging due to the low temperatures and pressures characteristic of the upper troposphere.

In this dissertation, I have focused on an improved understanding of upper tropospheric NO_x chemistry using observations obtained during two airborne field campaigns: Deep Convective Clouds and Chemistry (DC3) and Studies of Emissions and Atmospheric Composition, Clouds and Climate Coupling by Regional Surveys (SEAC4RS). Briefly, I measured atmospheric $CH_3O_2NO_2$ for the first time and demonstrated that it is an important reservoir of NO_x at the cold temperatures of the upper troposphere ($T < 255$ K). Then, I directly measured the upper tropospheric production rates of all the NO_x oxidative products and showed that while several rate expressions for NO_x and hydrocarbon oxidation are consistent with observations, some of the key rate coefficients for NO_x oxidation that are extrapolated to the temperature and pressure of the upper troposphere are between 30 – 50% too fast, and should be measured in the laboratory for confirmation at the relevant lower temperatures and pressures. Finally, implementing the updated chemistry from Chapters 2 and 3, I evaluated the representation of lightning NO_x emission rates in a model (GEOS-Chem) and suggest that these rates should increase by at least 33% to be more consistent with *in situ* and space-based observations.

The changes to kinetic and emission parameters described above affect our understanding of upper tropospheric NO_x and O_3 chemistry. When these changes are included in a model, the result for upper tropospheric O_3 predictions is that they are between 5 to 10% higher. This is a combination of 3 effects, the increased emissions of NO_x from lightning, the longer lifetime to conversion to HNO_3, and the role of $CH_3O_2NO_2$ in spreading NO_x further from the lightning source. The revised model predicts an increase in ozone instantaneous radiative forcing of approximately 4 – 12%, using the relationship of O_3 mixing ratios to the instantaneous radiative forcing from Aghedo et al. (2011). Lightning flash rates will increase with warming temperatures, as predicted by Romps et al. (2014), which will lead to more upper tropospheric O_3 in the future.

These results raise further questions about our understanding of upper tropospheric chemistry:

(1) What is the seasonal and diurnal behavior of $CH_3O_2NO_2$ in the upper troposphere? From the modeling results of Browne et al. (2011), $CH_3O_2NO_2$ showed a strong seasonal dependence with the highest mixing ratios in summer and the lowest mixing ratios in winter. In Chapter 2, the comparison of the $CH_3O_2NO_2$ profile between DC3 and SEAC4RS showed that $CH_3O_2NO_2$ mixing ratios increased from late spring to late summer, indicating that we currently understand the chemistry and precursors of $CH_3O_2NO_2$ during these two seasons. Measurements in other seasons are needed to evaluate the accuracy of this prediction to ensure we understand $CH_3O_2NO_2$ chemistry and precursors, furthering our understanding of upper tropospheric NO_x chemistry and lifetime and thus O_3 concentrations.

The measurements for the two campaigns described in this dissertation were biased toward fresh lightning NO_x emissions, which promote $CH_3O_2NO_2$ production. In the upper troposphere, $CH_3O_2NO_2$ has a short photolytic and thermal lifetime (typically less than 1 day). In the far field from emissions, we would expect to observe a daily cycle in $CH_3O_2NO_2$, similar to that of HO_2NO_2 (e.g., Wennberg et al., 1999; Kim et al., 2007). Observing this pattern in $CH_3O_2NO_2$ simultaneously with HO_2NO_2 would test our understanding of upper tropospheric NO_x and HO_x chemistry.

(2) What is the chemical fate of peroxynitrous acid (HOONO), the minor product produced from the reaction of OH with NO_2? To date, there is little insight about the chemical fate of HOONO. It is currently thought to chemically behave similarly to HO_2NO_2; however, majority of our understanding of this compound is theoretical (e.g., Golden and Smith, 2000; Golden et al., 2003). If this is true, HOONO is a non-negligible reservoir of NO_x, and would impact the NO_x lifetime in a similar fashion to HO_2NO_2 and lead to lower NO_x lifetimes than I found in Chapter 3. However, if HOONO is significantly more unstable and has shorter lifetime than what would be described by HO_2NO_2 chemistry, HOONO would not greatly change my results about the NO_x lifetime in Chapter 3. Alternatively, HOONO could not be very reactive to OH or have similar cross-sections as HO_2NO_2, which would increase the HOONO lifetime and would decrease the upper tropospheric NO_x lifetime in Chapter 3.

(3) What is the hydrolysis rate leading to the production of HNO_3 in the upper troposphere? In Chapter 3, I provided further evidence that the daytime HNO_3 production rate should decrease by ~30% in the upper troposphere. The slower production rate decreases modeled HNO_3 mixing ratios, leading to better agreement between observations and model calculations (Chapter 4; Seltzer et al., 2015). However, the ratio of NO_x to HNO_3 in the model is still lower than in the observations. In Chapter 4, I hypothesized that the most likely reason for the too high modeled HNO_3 mixing ratios is the hydrolysis rate that converts dinitrogen pentoxide, N_2O_5, to 2 HNO_3, used in models is too fast. The reaction is well known to be fast in the stratosphere. However, recent boundary layer observations have indicated that the rate depends strongly on aerosol composition which is more varied in the troposphere than the stratosphere. On some aerosol types, the generic rate assumed in models is at least 1 order of magnitude too fast (e.g., Brown et al., 2009). Direct observations of NO_3 and N_2O_5 have not been made in the upper troposphere. Measurements of N_2O_5 during day and night in the upper troposphere would be important contributions to understanding the NO_x and HNO_3 budgets in the region.

An alternative to the hydrolysis rate being too high is that the loss rates of HNO_3 are too low. Prior studies have attempted to use observations to constrain the photolysis and photooxidation rates for HNO_3 in the upper troposphere and lower stratosphere; however, the results did not provide any evidence if the rates are too slow (e.g., Cohen et al., 2000). Similarly, the transport and dilution rates or uptake to aerosols or cloud droplets could be too slow. Understanding these processes will provide opportunities to further evaluate upper tropospheric NO_x chemistry and lightning NO_x emission rates.

(4) What is the branching ratio and fate of alkyl and multifunctional nitrates in the upper troposphere? In Chapter 3, I provided some of the first measurements and evaluations of the production and fate of upper tropospheric alkyl and multifunctional nitrates. However, the

branching ratios I used to calculate the production rates is highly parameterized (Carter and Atkinson, 1989), and there have been minimal studies evaluating the branching ratios for different alkyl and multifunctional nitrates at the temperatures and pressures characteristic of the upper troposphere (Butkovskaya et al., 2010; Butkovskaya et al., 2012). Since I have shown that the production of alkyl and multifunctional nitrates are an important NO_x sink (~20% of the sink) in the near-field of lightning NO_x emissions, evaluation of these branching ratios are necessary to better understand upper tropospheric NO_x lifetime and evaluation of lightning NO_x emission rates. If the branching ratios are different than the calculated values from Carter and Atkinson (1989), it will change our understanding of the near-field NO_x lifetime and O_3 production rates.

In conclusion, my dissertation has provided important progress in understanding upper tropospheric NO_x chemistry and emissions. The upper troposphere encompasses a large fraction of the atmosphere and represents an important region for the radiative forcing of O_3. The results indicate that the typical approach of extrapolating results from boundary layer conditions to the upper troposphere does not properly describe upper tropospheric chemistry, which impacts NO_x, HO_x, O_3 and our interpretation of lightning NO_x emission rates. Future work should focus on the production and loss rate constants for short-lived species, specifically N_2O_5 and HOONO, which is necessary to understand upper tropospheric NO_x, HO_x, and O_3 chemistry. Also, the use of future geostationary satellites will provide excellent opportunities to investigate the evolution and chemistry of upper tropospheric lightning NO_x emissions, providing further evaluation of our understanding of the kinetics, products, and emission rates.

References

Aghedo, A. M., Bowman, K. W., Worden, H. M., Kulawik, S. S., Shindell, D. T., Lamarque, J. F., Faluvegi, G., Parrington, M., Jones, D. B. A. and Rast, S.: The vertical distribution of ozone instantaneous radiative forcing from satellite and chemistry climate models, J. Geophys. Res., 116, D01305, doi:10.1029/2010JD014243, 2011.

Allen, D., Pickering, K., Duncan, B. and Damon, M.: Impact of lightning NO emissions on North American photochemistry as determined using the Global Modeling Initiative (GMI) model, J. Geophys. Res., 115, doi:10.1029/2010JD014062, 2010.

Allen, D. J., Pickering, K. E., Pinder, R. W., Henderson, B. H., Appel, K. W. and Prados, A.: Impact of lightning-NO on eastern United States photochemistry during the summer of 2006 as determined using the CMAQ model, Atmos. Chem. Phys., 12, 1737-1758, doi:10.5194/acp-12-1737-2012, 2012.

Apel, E. C., Olson, J. R., Crawford, J. H., Hornbrook, R. S., Hills, A. J., Cantrell, C. A., Emmons, L. K., Knapp, D. J., Hall, S., Mauldin III, R. L., Weinheimer, A. J., Fried, A., Blake, D. R., Crounse, J. D., Clair, J. M. S., Wennberg, P. O., Diskin, G. S., Fuelberg, H. E., Wisthaler, A., Mikoviny, T., Brune, W. and Riemer, D. D.: Impact of the deep convection of isoprene and other reactive trace species on radicals and ozone in the upper troposphere, Atmos. Chem. Phys., 12, 1135-1150, doi:10.5194/acp-12-1135-2012, 2012.

Atkinson, R.: Kinetics and Mechanisms of the Gas-Phase Reactions of the Hydroxyl Radical with Organic-Compounds Under Atmospheric Conditions, Chem. Rev., 86, 69-201, doi:10.1021/cr00071a004, 1986.

Atkinson, R.: Kinetics of the gas-phase reactions of OH radicals with alkanes and cycloalkanes, Atmos. Chem. Phys., 3, 2233-2307, doi:10.5194/acp-3-2233-2003, 2003.

Atkinson, R., Baulch, D., Cox, R., Crowley, J., Hampson, R., Hynes, R., Jenkin, M., Rossi, M. and Troe, J.: Evaluated kinetic and photochemical data for atmospheric chemistry: Volume I - gas phase reactions of O_x, HO_x, NO_x and SO_x species, Atmos. Chem. Phys., 4, 1461-1738, doi:10.5194/acp-6-3625-2006, 2004.

Atkinson, R., Baulch, D. L., Cox, R. A., Crowley, J. N., Hampson, R. F., Hynes, R. G., Jenkin, M. E., Rossi, M. J. and Troe, J.: Evaluated kinetic and photochemical data for atmospheric chemistry: Volume II - gas phase reactions of organic species, Atmos. Chem. Phys., 6, 3625-4055, doi:10.5194/acp-6-3625-2006, 2006.

Bacak, A., Bardwell, M., Raventos-Duran, M., Percival, C., Hamer, P. and Shallcross, D.: Kinetics of the CH_3O_2 + NO_2 reaction: A temperature and pressure dependence study using chemical ionisation mass spectrometry, Chem. Phys. Lett., 419, 125-129, doi:10.1016/j.cplett.2005.11.070, 2006.

Bacak, A., Cooke, M. C., Bardwell, M. W., McGillen, M. R., Archibald, A. T., Huey, L. G., Tanner, D., Utembe, S. R., Jenkin, M. E., Derwent, R. G., Shallcross, D. E. and Percival, C. J.: Kinetics of the HO_2 + NO_2 Reaction: On the impact of new gas-phase kinetic data for the formation of HO_2NO_2 on HO_x, NO_x and HO_2NO_2 levels in the troposphere, Atmos. Environ., 45, 6414-6422, doi:10.1016/j.atmosenv.2011.08.008, 2011.

Barth, M. C., Cantrell, C. A., Brune, W. H., Rutledge, S. A., Crawford, J. H., Huntrieser, H., Carey, L. D., MacGorman, D., Weisman, M., Pickering, K. E., Bruning, E., Anderson, B., Apel, E., Biggerstaff, M., Campos, T., Campuzano-Jost, P., Cohen, R., Crounse, J., Day, D. A., Diskin, G., Flocke, F., Fried, A., Garland, C., Heikes, B., Honomichl, S., Hornbrook, R., Huey, L. G., Jimenez, J. L., Lang, T., Lichtenstern, M., Mikoviny, T., Nault, B., O'Sullivan, D., Pan, L. L., Peischl, J., Pollack, I., Richter, D., Riemer, D., Ryerson, T., Schlager, H., St. Clair, J., Walega, J., Weibring, P., Weinheimer, A., Wennberg, P., Wisthaler, A., Wooldridge, P. J. and Ziegler, C.: The Deep Convective Clouds and Chemistry (DC3) Field Campaign, Bull. Am. Meteorol. Soc., 96, 1281-1309, doi:10.1175/BAMS-D-13-00290.1, 2015.

Bechara, J., Borbon, A., Jambert, C., Colomb, A. and Perros, P. E.: Evidence of the impact of deep convection on reactive Volatile Organic Compounds in the upper tropical troposphere during the AMMA experiment in West Africa, Atmos. Chem. Phys., 10, 10321-10334, doi:10.5194/acp-10-10321-2010, 2010.

Beirle, S., Platt, U., Wenig, M. and Wagner, T.: NO_x production by lightning estimated with GOME, Trace Constituents in the Troposphere and Lower Stratosphere, 34, 793-797, doi:10.1016/j.asr.2003.07.069, 2004.

Beirle, S., Huntrieser, H. and Wagner, T.: Direct satellite observation of lightning-produced NO_x, Atmos. Chem. Phys., 10, 10965-10986, doi:10.5194/acp-10-10965-2010, 2010.

Bertram, T. H., Perring, A. E., Wooldridge, P. J., Crounse, J. D., Kwan, A. J., Wennberg, P. O., Scheuer, E., Dibb, J., Avery, M., Sachse, G., Vay, S. A., Crawford, J. H., McNaughton, C. S., Clarke, A., Pickering, K. E., Fuelberg, H., Huey, G., Blake, D. R., Singh, H. B., Hall, S. R., Shetter, R. E., Fried, A., Heikes, B. G. and Cohen, R. C.: Direct Measurements of the Convective Recycling of the Upper Troposphere, Science, 315, 816-820, doi:10.1126/science.1134548, 2007.

Bertram, T. H. and Thornton, J. A.: Toward a general parameterization of N_2O_5 reactivity on aqueous particles: the competing effects of particle liquid water, nitrate and chloride, Atmos. Chem. Phys., 9, 8351-8363, doi:10.5194/acp-9-8351-2009, 2009.

Bey, I., Jacob, D., Yantosca, R., Logan, J., Field, B., Fiore, A., Li, Q., Liu, H., Mickley, L. and Schultz, M.: Global modeling of tropospheric chemistry with assimilated meteorology: Model description and evaluation, J. Geophys. Res., 106, 23073-23095, doi:10.1029/2001JD000807, 2001.

Blake, N. J., Blake, D. R., Simpson, I. J., Meinardi, S., Swanson, A. L., Lopez, J. P., Katzenstein, A. S., Barletta, B., Shirai, T., Atlas, E., Sachse, G., Avery, M., Vay, S., Fuelberg, H. E., Kiley, C.

M., Kita, K. and Rowland, F. S.: NMHCs and halocarbons in Asian continental outflow during the Transport and Chemical Evolution over the Pacific (TRACE-P) Field Campaign: Comparison with PEM-West B, J. Geophys. Res., 108, 8806, doi:10.1029/2002JD003367, 2003.

Boersma, K. F., Eskes, H. J., Dirksen, R. J., van, d. A., Veefkind, J. P., Stammes, P., Huijnen, V., Kleipool, Q. L., Sneep, M., Claas, J., Leitão, J., Richter, A., Zhou, Y. and Brunner, D.: An improved tropospheric NO_2 column retrieval algorithm for the Ozone Monitoring Instrument, Atmos. Meas. Tech., 4, 1905-1928, doi:10.5194/amt-4-1905-2011, 2011.

Bradshaw, J., Davis, D., Crawford, J., Chen, G., Shetter, R., Muller, M., Gregory, G., Sachse, G., Blake, D., Heikes, B., Singh, H., Mastromarino, J. and Sandholm, S.: Photofragmentation two-photon laser-induced fluorescence detection of NO_2 and NO: Comparison of measurements with model results based on airborne observations during PEM-Tropics A, Geophys. Res. Lett., 26, 471-474, doi:10.1029/1999GL900015, 1999.

Brown, S. S., Dube, W. P., Fuchs, H., Ryerson, T. B., Wollny, A. G., Brock, C. A., Bahreini, R., Middlebrook, A. M., Neuman, J. A., Atlas, E., Roberts, J. M., Osthoff, H. D., Trainer, M., Fehsenfeld, F. C. and Ravishankara, A. R.: Reactive uptake coefficients for N_2O_5 determined from aircraft measurements during the Second Texas Air Quality Study: Comparison to current model parameterizations, J. Geophys. Res., 114, D00F10, doi:10.1029/2008JD011679, 2009.

Browne, E. C., Perring, A. E., Wooldridge, P. J., Apel, E., Hall, S. R., Huey, L. G., Mao, J., Spencer, K. M., Clair, J. M. S., Weinheimer, A. J., Wisthaler, A. and Cohen, R. C.: Global and regional effects of the photochemistry of $CH_3O_2NO_2$: evidence from ARCTAS, Atmos. Chem. Phys., 11, 4209-4219, doi:10.5194/acp-11-4209-2011, 2011.

Bucsela, E. J., Pickering, K. E., Huntemann, T. L., Cohen, R. C., Perring, A., Gleason, J. F., Blakeslee, R. J., Albrecht, R. I., Holzworth, R., Cipriani, J. P., Vargas-Navarro, D., Mora-Segura, I., Pacheco-Hernandez, A. and Laporte-Molina, S.: Lightning-generated NO_x seen by the Ozone Monitoring Instrument during NASA's Tropical Composition, Cloud and Climate Coupling Experiment (TC4), J. Geophys. Res., 115, D00J10, doi:10.1029/2009JD013118, 2010.

Bucsela, E. J., Krotkov, N. A., Celarier, E. A., Lamsal, L. N., Swartz, W. H., Bhartia, P. K., Boersma, K. F., Veefkind, J. P., Gleason, J. F. and Pickering, K. E.: A new stratospheric and tropospheric NO_2 retrieval algorithm for nadir-viewing satellite instruments: applications to OMI, Atmos. Meas. Tech., 6, 2607-2626, doi:10.5194/amt-6-2607-2013, 2013.

Butkovskaya, N. I., Kukui, A., Pouvesle, N. and Le Bras, G.: Formation of Nitric Acid in the Gas-Phase HO_2 + NO Reaction: Effects of Temperature and Water Vapor, J. Phys. Chem. A, 109, 6509-6520, doi:10.1021/jp051534v, 2005.

Butkovskaya, N., Kukui, A. and Le Bras, G.: HNO_3 Forming Channel of the HO_2 + NO Reaction as a Function of Pressure and Temperature in the Ranges of 72-600 Torr and 223-323 K, J. Phys. Chem. A, 111, 9047-9053, doi:10.1021/jp074117m, 2007.

Butkovskaya, N., Rayez, M., Rayez, J., Kukui, A. and Le Bras, G.: Water Vapor Effect on the HNO_3 Yield in the HO_2 + NO Reaction: Experimental and Theoretical Evidence, J. Phys. Chem. A, 113, 11327-11342, doi:10.1021/jp811428p, 2009.

Butkovskaya, N., Kukui, A. and Le Bras, G.: Pressure and Temperature Dependence of Ethyl Nitrate Formation in the $C_2H_5O_2$ + NO Reaction, J. Phys. Chem. A, 114, 956-964, doi:10.1021/jp910003a, 2010.

Butkovskaya, N., Kukui, A. and Le Bras, G.: Pressure and Temperature Dependence of Methyl Nitrate Formation in the CH_3O_2+NO Reaction, J. Phys. Chem. A, 116, 5972-5980, doi:10.1021/jp210710d, 2012.

Cantrell, C. A.: Technical Note: Review of methods for linear least-squares fitting of data and application to atmospheric chemistry problems, Atmos. Chem. Phys., 8, 5477-5487, doi:10.5194/acp-8-5477-2008, 2008.

Cariolle, D., Evans, M. J., Chipperfield, M. P., Butkovskaya, N., Kukui, A. and Le Bras, G.: Impact of the new HNO_3-forming channel of the HO_2 + NO reaction on tropospheric HNO_3, NO_x, HO_x and ozone, Atmos. Chem. Phys., 8, 4061-4068, doi:10.5194/acp-8-4061-2008, 2008.

Carter, W. and Atkinson, R.: Alkyl Nitrate Formation from the Atmospheric Photooxidation of Alkanes - a Revised Estimation Method, J. Atmos. Chem., 8, 165-173, doi:10.1007/BF00053721, 1989.

Christensen, L. E., Okumura, M., Sander, S. P., Friedl, R. R., Miller, C. E. and Sloan, J. J.: Measurements of the rate constant of $HO_2 + NO_2 + N_2 \rightarrow HO_2NO_2 + N_2$ using near-infrared wavelength-modulation spectroscopy and UV-visible absorption spectroscopy, J. Phys. Chem. A, 108, 80-91, doi:10.1021/jp035905o, 2004.

Cleary, P. A., Wooldridge, P. J. and Cohen, R. C.: Laser-induced fluorescence detection of atmospheric NO_2 with a commercial diode laser and a supersonic expansion, Appl. Opt., 41, 6950-6956, doi:10.1364/AO.41.006950, 2002.

Cohen, R., Perkins, K., Koch, L., Stimpfle, R., Wennberg, P., Hanisco, T., Lanzendorf, E., Bonne, G., Voss, P., Salawitch, R., Del Negro, L., Wilson, J., McElroy, C. and Bui, T.: Quantitative constraints on the atmospheric chemistry of nitrogen oxides: An analysis along chemical coordinates, J. Geophys. Res., 105, 24283-24304, doi:10.1029/2000JD900290, 2000.

Cooper, M., Martin, R. V., Sauvage, B., Boone, C. D., Walker, K. A., Bernath, P. F., McLinden, C. A., Degenstein, D. A., Volz-Thomas, A. and Wespes, C.: Evaluation of ACE-FTS and OSIRIS Satellite retrievals of ozone and nitric acid in the tropical upper troposphere: Application to ozone production efficiency, J. Geophys. Res., 116, D12306, doi:10.1029/2010JD015056, 2011.

Cooper, M., Martin, R. V., Wespes, C., Coheur, P., Clerbaux, C. and Murray, L. T.: Tropospheric nitric acid columns from the IASI satellite instrument interpreted with a chemical

transport model: Implications for parameterizations of nitric oxide production by lightning, J. Geophys. Res., 119, 10068-10079, doi:10.1002/2014JD021907, 2014.

Crounse, J. D., McKinney, K. A., Kwan, A. J. and Wennberg, P. O.: Measurement of Gas-Phase Hydroperoxides by Chemical Ionization Mass Spectrometry, Anal. Chem., 78, 6726-6732, doi:10.1021/ac0604235, 2006.

Crounse, J. D., Knap, H. C., Ornso, K. B., Jorgensen, S., Paulot, F., Kjaergaard, H. G. and Wennberg, P. O.: Atmospheric Fate of Methacrolein. 1. Peroxy Radical Isomerization Following Addition of OH and O_2, J. Phys. Chem. A, 116, 5756-5762, doi:10.1021/jp211560u, 2012.

Davis, D., Chen, G., Chameides, W., Bradshaw, J., Sandholm, S., Rodgers, M., Schendal, J., Madronich, S., Sachse, G., Gregory, G., Anderson, B., Barrick, J., Shipham, M., Collins, J., Wade, L. and Blake, D.: A Photostationary State Analysis of the NO_2-NO System Based on Airborne Observations from the Subtropical Tropical North and South-Atlantic, J. Geophys. Res., 98, 23501-23523, doi:10.1029/93JD02412, 1993.

Day, D., Wooldridge, P., Dillon, M., Thornton, J. and Cohen, R.: A thermal dissociation laser-induced fluorescence instrument for in situ detection of NO_2, peroxy nitrates, alkyl nitrates, and HNO_3, J. Geophys. Res., 107, 4046, doi:10.1029/2001JD000779, 2002.

DC3 Data Archive: National Aeronautical and Space Agency, Deep Convective Clouds and Chemistry, DC-8, Version 5, doi:10.5067/Aircraft/DC3/DC8/Aerosol-TraceGas, access: September 20 2014.

DeCaria, A. J., Pickering, K. E., Stenchikov, G. L., Scala, J. R., Stith, J. L., Dye, J. E., Ridley, B. A. and Laroche, P.: A cloud-scale model study of lightning-generated NO_x in an individual thunderstorm during STERAO-A, J. Geophys. Res., 105, 11601-11616, doi:10.1029/2000JD900033, 2000.

DeCaria, A. J., Pickering, K. E., Stenchikov, G. L. and Ott, L.: Lightning-generated NO_x and its impact on tropospheric ozone production: A three-dimensional modeling study of a Stratosphere-Troposphere Experiment: Radiation, Aerosols and Ozone (STERAO-A) thunderstorm, J. Geophys. Res., 110, doi:10.1029/2004JD005556, 2005.

DeCarlo, P. F., Kimmel, J. R., Trimborn, A., Northway, M. J., Jayne, J. T., Aiken, A. C., Gonin, M., Fuhrer, K., Horvath, T., Docherty, K. S., Worsnop, D. R. and Jimenez, J. L.: Field-deployable, high-resolution, time-of-flight aerosol mass spectrometer, Anal. Chem., 78, 8281-8289, doi:10.1021/ac061249n, 2006.

Diskin, G. S., Podolske, J. R., Sachse, G. W. and Slate, T. A.: Open-path airborne tunable diode laser hygrometer, in: Diode Lasers and Applications in Atmospheric Sensing, edited by: Fried, A., SPIE Proceedings, 4817, 196-204, doi:10.1117/12.453736, 2002.

Evans, M. and Jacob, D.: Impact of new laboratory studies of N_2O_5 hydrolysis on global model budgets of tropospheric nitrogen oxides, ozone, and OH, Geophys. Res. Lett., 32, L09813, doi:10.1029/2005GL022469, 2005.

Faloona, I., Tan, D., Lesher, R., Hazen, N., Frame, C., Simpas, J., Harder, H., Martinez, M., Di Carlo, P., Ren, X. and Brune, W.: A laser-induced fluorescence instrument for detecting tropospheric OH and HO_2: Characteristics and calibration, J. Atmos. Chem., 47, 139-167, doi:10.1023/B:JOCH.0000021036.53185.0e, 2004.

Fang, Y., Fiore, A. M., Horowitz, L. W., Levy II, H., Hu, Y. and Russell, A. G.: Sensitivity of the NO_y budget over the United States to anthropogenic and lightning NO_x in summer, J. Geophys. Res., 115, D18312, doi:10.1029/2010JD014079, 2010.

Fischer, E. V., Jacob, D. J., Yantosca, R. M., Sulprizio, M. P., Millet, D. B., Mao, J., Paulot, F., Singh, H. B., Roiger, A., Ries, L., Talbot, R. W., Dzepina, K. and Deolal, S. P.: Atmospheric peroxyacetyl nitrate (PAN): a global budget and source attribution, Atmos. Chem. Phys., 14, 2679-2698, doi:10.5194/acp-14-2679-2014, 2014.

Folkins, I. and Chatfield, R.: Impact of acetone on ozone production and OH in the upper troposphere at high NO_x, J. Geophys. Res., 105, 11585-11599, doi:10.1029/2000JD900067, 2000.

Froidevaux, L., Livesey, N., Read, W., Jiang, Y., Jimenez, C., Filipiak, M., Schwartz, M., Santee, M., Pumphrey, H., Jiang, J., Wu, D., Manney, G., Drouin, B., Waters, J., Fetzer, E., Bernath, P., Boone, C., Walker, K., Jucks, K., Toon, G., Margitan, J., Sen, B., Webster, C., Christensen, L., Elkins, J., Atlas, E., Lueb, R. and Hendershot, R.: Early validation analyses of atmospheric profiles from EOS MLS on the Aura satellite, IEEE Trans. Geosci. Remote Sens., 44, 1106-1121, doi:10.1109/TGRS.2006.864366, 2006.

Fry, J. L., Kiendler-Scharr, A., Rollins, A. W., Wooldridge, P. J., Brown, S. S., Fuchs, H., Dubé, W. P., Mensah, A., dal Maso, M., Tillmann, R., Dorn, H. -., Brauers, T. and Cohen, R. C.: Organic nitrate and secondary organic aerosol yield from NO_3 oxidation of beta-pinene evaluated using a gas-phase kinetics/aerosol partitioning model, Atmos. Chem. Phys., 9, 1431-1449, doi:10.5194/acp-9-1431-2009, 2009.

Fry, J. L., Kiendler-Scharr, A., Rollins, A. W., Brauers, T., Brown, S. S., Dorn, H. -., Dubé, W. P., Fuchs, H., Mensah, A., Rohrer, F., Tillmann, R., Wahner, A., Wooldridge, P. J. and Cohen, R. C.: SOA from limonene: role of NO_3 in its generation and degradation, Atmos. Chem. Phys., 11, 3879-3894, doi:10.5194/acp-11-3879-2011, 2011.

Fry, J. L., Draper, D. C., Zarzana, K. J., Campuzano-Jost, P., Day, D. A., Jimenez, J. L., Brown, S. S., Cohen, R. C., Kaser, L., Hansel, A., Cappellin, L., Karl, T., Roux, A. H., Turnipseed, A., Cantrell, C., Lefer, B. L. and Grossberg, N.: Observations of gas- and aerosol-phase organic nitrates at BEACHON-RoMBAS 2011, Atmos. Chem. Phys., 13, 8585-8605, doi:10.5194/acp-13-8585-2013, 2013.

Golden, D. M. and Smith, G. P.: Reaction of OH + NO_2 + M: A New View, J. Phys. Chem. A, 104, 3991-3997, doi:10.1021/jp9939928, 2000.

Golden, D. M., Barker, J. R. and Lohr, L. L.: Master Equation Models for the Pressure- and Temperature-Dependent Reactions HO + NO_2 → $HONO_2$ and HO + NO_2 → HOONO, J. Phys. Chem. A, 107, 11057-11071, doi:10.1021/jp0353183, 2003.

Goldenbaum, G. and Dickerson, R.: Nitric-Oxide Production by Lightning Discharges, J. Geophys. Res., 98, 18333-18338, doi:10.1029/93JD01018, 1993.

Gottschaldt, K., Voigt, C., Joeckel, P., Righi, M., Deckert, R. and Dietmüller, S.: Global sensitivity of aviation NO_x effects to the HNO_3-forming channel of the HO_2 + NO reaction, Atmos. Chem. Phys., 13, 3003-3025, doi:10.5194/acp-13-3003-2013, 2013.

Henderson, B. H., Pinder, R. W., Crooks, J., Cohen, R. C., Hutzell, W. T., Sarwar, G., Goliff, W. S., Stockwell, W. R., Fahr, A., Mathur, R., Carlton, A. G. and Vizuete, W.: Evaluation of simulated photochemical partitioning of oxidized nitrogen in the upper troposphere, Atmos. Chem. Phys., 11, 275-291, doi:10.5194/acp-11-275-2011, 2011.

Henderson, B. H., Pinder, R. W., Crooks, J., Cohen, R. C., Carlton, A. G., Pye, H. O. T. and Vizuete, W.: Combining Bayesian methods and aircraft observations to constrain the $HO^{\cdot}$ + NO_2 reaction rate, Atmos. Chem. Phys., 12, 653-667, doi:10.5194/acp-12-653-2012, 2012.

Hudman, R. C., Jacob, D. J., Turquety, S., Leibensperger, E. M., Murray, L. T., Wu, S., Gilliland, A. B., Avery, M., Bertram, T. H., Brune, W., Cohen, R. C., Dibb, J. E., Flocke, F. M., Fried, A., Holloway, J., Neuman, J. A., Orville, R., Perring, A., Ren, X., Sachse, G. W., Singh, H. B., Swanson, A. and Wooldridge, P. J.: Surface and lightning sources of nitrogen oxides over the United States: Magnitudes, chemical evolution, and outflow, J. Geophys. Res., 112, D12S05, doi:10.1029/2006JD007912, 2007.

Hudman, R. C., Russell, A. R., Valin, L. C. and Cohen, R. C.: Interannual variability in soil nitric oxide emissions over the United States as viewed from space, Atmos. Chem. Phys., 10, 9943-9952, doi:10.5194/acp-10-9943-2010, 2010.

Huntrieser, H., Schlager, H., Roiger, A., Lichtenstern, M., Schumann, U., Kurz, C., Brunner, D., Schwierz, C., Richter, A. and Stohl, A.: Lightning-produced NO_x over Brazil during TROCCINOX: airborne measurements in tropical and subtropical thunderstorms and the importance of mesoscale convective systems, Atmos. Chem. Phys., 7, 2987-3013, 2007.

Huntrieser, H., Schlager, H., Lichtenstern, M., Roiger, A., Stock, P., Minikin, A., Hoeller, H., Schmidt, K., Betz, H. -., Allen, G., Viciani, S., Ulanovsky, A., Ravegnani, F. and Brunner, D.: NO_x production by lightning in Hector: first airborne measurements during SCOUT-O3/ACTIVE, Atmos. Chem. Phys., 9, 8377-8412, doi:10.5194/acp-9-8377-2009, 2009.

Huntrieser, H., Schlager, H., Lichtenstern, M., Stock, P., Hamburger, T., Hoeller, H., Schmidt, K., Betz, H., Ulanovsky, A. and Ravegnani, F.: Mesoscale convective systems observed during

AMMA and their impact on the NO_x and O_3 budget over West Africa, Atmos. Chem. Phys., 11, 2503-2536, doi:10.5194/acp-11-2503-2011, 2011.

Jacob, D. J., Heikes, B. G., Fan, S. M., Logan, J. A., Mauzerall, D. L., Bradshaw, J. D., Singh, H. B., Gregory, G. L., Talbot, R. W., Blake, D. R. and Sachse, G. W.: Origin of ozone and NO_x in the tropical troposphere: A photochemical analysis of aircraft observations over the South Atlantic basin, J. Geophys. Res., 101, 24235-24250, doi:10.1029/96JD00336, 1996.

Jaeglé, L., Jacob, D., Brune, W. and Wennberg, P.: Chemistry of HO_x radicals in the upper troposphere, Atmos. Environ., 35, 469-489, doi:10.1016/S1352-2310(00)00376-9, 2001.

Jiménez, E., Gierczak, T., Stark, H., Burkholder, J. and Ravishankara, A.: Reaction of OH with HO_2NO_2 (peroxynitric acid): Rate coefficients between 218 and 335 K and product yields at 298 K, J. Phys. Chem. A, 108, 1139-1149, doi:10.1021/jp0363489, 2004.

Jourdain, L., Kulawik, S. S., Worden, H. M., Pickering, K. E., Worden, J. and Thompson, A. M.: Lightning NO_x emissions over the USA constrained by TES ozone observations and the GEOS-Chem model, Atmos. Chem. Phys., 10, 107-119, doi:10.5194/acp-10-107-2010, 2010.

Kim, S., Huey, L. G., Stickel, R. E., Tanner, D. J., Crawford, J. H., Olson, J. R., Chen, G., Brune, W. H., Ren, X., Lesher, R., Wooldridge, P. J., Bertram, T. H., Perring, A., Cohen, R. C., Lefer, B. L., Shetter, R. E., Avery, M., Diskin, G. and Sokolik, I.: Measurement of HO_2NO_2 in the free troposphere during the intercontinental chemical transport experiment - North America 2004, J. Geophys. Res., 112, D12S01, doi:10.1029/2006JD007676, 2007.

Kinnison, D. E., Gille, J., Barnett, J., Randall, C., Harvey, V. L., Lambert, A., Khosravi, R., Alexander, M. J., Bernath, P. F., Boone, C. D., Cavanaugh, C., Coffey, M., Craig, C., Dean, V. C., Eden, T., Ellis, D., Fahey, D. W., Francis, G., Halvorson, C., Hannigan, J., Hartsough, C., Hepplewhite, C., Krinsky, C., Lee, H., Mankin, B., Marcy, T. P., Massie, S., Nardi, B., Packman, D., Popp, P. J., Santee, M. L., Yudin, V. and Walker, K. A.: Global observations of HNO_3 from the High Resolution Dynamics Limb Sounder (HIRDLS): First results, J. Geophys. Res., 113, D16S44, doi:10.1029/2007JD008814, 2008.

Kliner, D., Daube, B., Burley, J. and Wofsy, S.: Laboratory investigation of the catalytic reduction technique for measurement of atmospheric NO_y, J. Geophys. Res., 102, 10759-10776, doi:10.1029/96JD03816, 1997.

Klonecki, A. and Levy, H.: Tropospheric chemical ozone tendencies in $CO\text{-}CH_4\text{-}NO_y\text{-}H_2O$ system: Their sensitivity to variations in environmental parameters and their application to a global chemistry transport model study, J. Geophys. Res., 102, 21221-21237, doi:10.1029/97JD01805, 1997.

Krotkov, N. A.: OMI/Aura NO_2 Cloud-Screened Total and Tropospheric Column Daily L3 Global 0.25deg Lat/Lon Grid, version 003, NASA Goddard Space Flight Center, doi:10.5067/Aura/OMI/DATA3007, access: Nov. 9 2015.

Kurylo, M. J. and Ouellette, P. A.: Rate Constants for the Reaction $HO_2 + NO_2 + N_2 \rightarrow HO_2NO_2 + N_2$ - the Temperature-Dependence of the Falloff Parameters, J. Phys. Chem., 91, 3365-3368, doi:10.1021/j100296a052, 1987.

Labrador, L. J., von Kuhlmann, R. and Lawrence, M. G.: Strong sensitivity of the global mean OH concentration and the tropospheric oxidizing efficiency to the source of NO_x from lightning, Geophys. Res. Lett., 31, L06102, doi:10.1029/2003GL019229, 2004.

Labrador, L. J., von Kuhlmann, R. and Lawrence, M. G.: The effects of lightning-produced NO_x and its vertical distribution on atmospheric chemistry: sensitivity simulations with MATCH-MPIC, Atmos. Chem. Phys., 5, 1815-1834, doi:10.5194/acp-5-1815-2005, 2005.

Lamsal, L. N., Martin, R. V., van Donkelaar, A., Celarier, E. A., Bucsela, E. J., Boersma, K. F., Dirksen, R., Luo, C. and Wang, Y.: Indirect validation of tropospheric nitrogen dioxide retrieved from the OMI satellite instrument: Insight into the seasonal variation of nitrogen oxides at northern midlatitudes, J. Geophys. Res., 115, D05302, doi:10.1029/2009JD013351, 2010.

Lee, D., Kohler, I., Grobler, E., Rohrer, F., Sausen, R., GallardoKlenner, L., Olivier, J., Dentener, F. and Bouwman, A.: Estimations of global NO_x emissions and their uncertainties, Atmos. Environ., 31, 1735-1749, doi:10.1016/S1352-2310(96)00327-5, 1997.

Lee, L., Wooldridge, P. J., Gilman, J. B., Warneke, C., de Gouw, J. and Cohen, R. C.: Low temperatures enhance organic nitrate formation: evidence from observations in the 2012 Uintah Basin Winter Ozone Study, Atmos. Chem. Phys., 14, 12441-12454, doi:10.5194/acp-14-12441-2014, 2014a.

Lee, L., Teng, A. P., Wennberg, P. O., Crounse, J. D. and Cohen, R. C.: On Rates and Mechanisms of OH and O_3 Reactions with Isoprene-Derived Hydroxy Nitrates, J. Phys. Chem. A, 118, 1622-1637, doi:10.1021/jp4107603, 2014b.

Leungsakul, S., Jaoui, M. and Kamens, R. M.: Kinetic mechanism for predicting secondary organic aerosol formation from the reaction of d-limonene with ozone, Environ. Sci. Technol., 39, 9583-9594, doi:10.1021/es0492687, 2005.

Levelt, P. F., Van den Oord, G. H. J., Dobber, M. R., Malkki, A., Visser, H., de Vries, J., Stammes, P., Lundell, J. O. V. and Saari, H.: The Ozone Monitoring Instrument, IEEE Trans. Geosci. Remote Sens., 44, 1093-1101, doi:10.1109/TGRS.2006.872333, 2006.

Levy, H., Moxim, W. J., Klonecki, A. A. and Kasibhatla, P. S.: Simulated tropospheric NO_x: Its evaluation, global distribution and individual source contributions, J. Geophys. Res., 104, 26279-26306, doi:10.1029/1999JD900442, 1999.

Liang, Q., Rodriguez, J. M., Douglass, A. R., Crawford, J. H., Olson, J. R., Apel, E., Bian, H., Blake, D. R., Brune, W., Chin, M., Colarco, P. R., da Silva, A., Diskin, G. S., Duncan, B. N., Huey, L. G., Knapp, D. J., Montzka, D. D., Nielsen, J. E., Pawson, S., Riemer, D. D., Weinheimer, A. J. and Wisthaler, A.: Reactive nitrogen, ozone and ozone production in the

Arctic troposphere and the impact of stratosphere-troposphere exchange, Atmos. Chem. Phys., 11, 13181-13199, doi:10.5194/acp-11-13181-2011, 2011.

Liaskos, C. E., Allen, D. J. and Pickering, K. E.: Sensitivity of tropical tropospheric composition to lightning NO_x production as determined by replay simulations with GEOS-5, J. Geophys. Res., 120, 8512-8534, doi:10.1002/2014JD022987, 2015.

Mao, J., Paulot, F., Jacob, D. J., Cohen, R. C., Crounse, J. D., Wennberg, P. O., Keller, C. A., Hudman, R. C., Barkley, M. P. and Horowitz, L. W.: Ozone and organic nitrates over the eastern United States: Sensitivity to isoprene chemistry, J. Geophys. Res., 118, 11256-11268, doi:10.1002/jgrd.50817, 2013.

Marmo, B. P., Carlton, A. G. and Henderson, B. H.: Partitioning of HNO_3, H_2O_2 and SO_2 to cloud ice: Simulations with CMAQ, Atmos. Environ., 88, 239-246, doi:10.1016/j.atmosenv.2013.12.041, 2014.

Martin, R. V., Sauvage, B., Folkins, I., Sioris, C. E., Boone, C., Bernath, P. and Ziemke, J.: Space-based constraints on the production of nitric oxide by lightning, J. Geophys. Res., 112, D09309, doi:10.1029/2006JD007831, 2007.

Martini, M., Allen, D. J., Pickering, K. E., Stenchikov, G. L., Richter, A., Hyer, E. J. and Loughner, C. P.: The impact of North American anthropogenic emissions and lightning on long-range transport of trace gases and their export from the continent during summers 2002 and 2004, J. Geophys. Res. 116, D07305, doi:10.1029/2010JD014305, 2011.

Miyazaki, K., Eskes, H. J., Sudo, K. and Zhang, C.: Global lightning NO_x production estimated by an assimilation of multiple satellite data sets, Atmos. Chem. Phys., 14, 3277-3305, doi:10.5194/acp-14-3277-2014, 2014.

Mollner, A. K., Valluvadasan, S., Feng, L., Sprague, M. K., Okumura, M., Milligan, D. B., Bloss, W. J., Sander, S. P., Martien, P. T., Harley, R. A., McCoy, A. B. and Carter, W. P. L.: Rate of Gas Phase Association of Hydroxyl Radical and Nitrogen Dioxide, Science, 330, 646-649, doi:10.1126/science.1193030, 2010.

Monks, P. S., Granier, C., Fuzzi, S., Stohl, A., Williams, M. L., Akimoto, H., Amann, M., Baklanov, A., Baltensperger, U., Bey, I., Blake, N., Blake, R. S., Carslaw, K., Cooper, O. R., Dentener, F., Fowler, D., Fragkou, E., Frost, G. J., Generoso, S., Ginoux, P., Grewe, V., Guenther, A., Hansson, H. C., Henne, S., Hjorth, J., Hofzumahaus, A., Huntrieser, H., Isaksen, I. S. A., Jenkin, M. E., Kaiser, J., Kanakidou, M., Klimont, Z., Kulmala, M., Laj, P., Lawrence, M. G., Lee, J. D., Liousse, C., Maione, M., McFiggans, G., Metzger, A., Mieville, A., Moussiopoulos, N., Orlando, J. J., O'Dowd, C. D., Palmer, P. I., Parrish, D. D., Petzold, A., Platt, U., Poeschl, U., Prevot, A. S. H., Reeves, C. E., Reimann, S., Rudich, Y., Sellegri, K., Steinbrecher, R., Simpson, D., ten Brink, H., Theloke, J., van der Werf, G. R., Vautard, R., Vestreng, V., Vlachokostas, C. and von Glasow, R.: Atmospheric composition change - global and regional air quality, Atmos. Environ., 43, 5268-5350, doi:10.1016/j.atmosenv.2009.08.021, 2009.

Murphy, J. G., Thornton, J. A., Wooldridge, P. J., Day, D. A., Rosen, R. S., Cantrell, C., Shetter, R. E., Lefer, B. and Cohen, R. C.: Measurements of the sum of HO_2NO_2 and $CH_3O_2NO_2$ in the remote troposphere, Atmos. Chem. Phys., 4, 377-384, doi:10.5194/acp-4-377-2004, 2004.

Murray, L. T., Jacob, D. J., Logan, J. A., Hudman, R. C. and Koshak, W. J.: Optimized regional and interannual variability of lightning in a global chemical transport model constrained by LIS/OTD satellite data, J. Geophys. Res., 117, D20307, doi:10.1029/2012JD017934, 2012.

Murray, L. T., Logan, J. A. and Jacob, D. J.: Interannual variability in tropical tropospheric ozone and OH: The role of lightning, J. Geophys. Res., 118, 11468-11480, doi:10.1002/jgrd.50857, 2013.

Myre, G., Shindell, D., Breon, F. -., Collins, W., Fuglestvedt, J., Huang, J., Koch, D., Lamarque, J. -., Lee, D., Mendoza, B., Nakajima, T., Robock, A., Stephens, G., Takemura, T. and Zhang, H.: Anthropogenic and Natural Radiative Forcing, in: Climate Change 2013: The Physical Science Basis. Contribution of Working Group I to the Fifth Assessment Report of the Intergovernmental Panel on Climate Change, Stocker, T. F., Qin, D., Plattner, G. -., Tignor, M., Allen, S. K., Boschung, J., Nauels, A., Xia, Y., Bex, V. and Midgley, P. M. (Eds.), Cambridge University Press, Cambridge, United Kingdom and New York, NY, USA, 659, 2013.

Nault, B. A., Garland, C., Pusede, S. E., Wooldridge, P. J., Ullmann, K., Hall, S. R. and Cohen, R. C.: Measurements of $CH_3O_2NO_2$ in the upper troposphere, Atmos. Meas. Tech., 8, 987 - 997, doi:10.5194/amt-8-987-2015, 2015a.

Nault, B. A., Garland, C., Wooldridge, P. J., Brune, W. H., Campuzano-Jost, P., Crounse, J. D., Day, D. A., Dibb, J., Hall, S. R., Huey, L. G., Jimenez, J. L., Liu, X., Mao, J., Mikoviny, T., Peischl, J., Pollack, I. B., Ren, X., Ryerson, T. B., Scheuer, E., Ullmann, K., Wennberg, P. O., Wisthaler, A., Zhang, L. and Cohen, R. C.: Observational Constraints on the Oxidation of NO_x in the Upper Troposphere, J. Phys. Chem. A, doi:10.1021/acs.jpca.5b07824, 2015b.

Neumaier, M., Ruhnke, R., Kirner, O., Ziereis, H., Stratmann, G., Brenninkmeijer, C. A. M. and Zahn, A.: Impact of acetone (photo) oxidation on HO_x production in the UT/LMS based on CARIBIC passenger aircraft observations and EMAC simulations, Geophys. Res. Lett., 41, 3289-3297, doi:10.1002/2014GL059480, 2014.

Ott, L. E., Pickering, K. E., Stenchikov, G. L., Allen, D. J., DeCaria, A. J., Ridley, B., Lin, R., Lang, S. and Tao, W.: Production of lightning NO_x and its vertical distribution calculated from three-dimensional cloud-scale chemical transport model simulations, J. Geophys. Res., 115, D04301, doi:10.1029/2009JD011880, 2010.

Pankow, J. F.: An Absorption-Model of Gas-Particle Partitioning of Organic-Compounds in the Atmosphere, Atmos. Environ., 28, 185-188, doi:10.1016/1352-2310(94)90093-0, 1994.

Pankow, J. F. and Asher, W. E.: SIMPOL.1: a simple group contribution method for predicting vapor pressures and enthalpies of vaporization of multifunctional organic compounds, Atmos. Chem. Phys., 8, 2773-2796, doi:10.5194/acp-8-2773-2008, 2008.

Paulot, F., Crounse, J. D., Kjaergaard, H. G., Kroll, J. H., Seinfeld, J. H. and Wennberg, P. O.: Isoprene photooxidation: new insights into the production of acids and organic nitrates, Atmos. Chem. Phys., 9, 1479-1501, doi:10.5194/acp-9-1479-2009, 2009.

Perring, A. E., Pusede, S. E. and Cohen, R. C.: An Observational Perspective on the Atmospheric Impacts of Alkyl and Multifunctional Nitrates on Ozone and Secondary Organic Aerosol, Chem. Rev., 113, 5848-5870, doi:10.1021/cr300520x, 2013.

Pickering, K. E., Wang, Y., Tao, W., Price, C. and Müller, J.: Vertical distributions of lightning NO_x for use in regional and global chemical transport models, J. Geophys. Res., 103, 31203-31216, doi:10.1029/98JD02651, 1998.

Praske, E., Crounse, J. D., Bates, K. H., Kurten, T., Kjaergaard, H. G. and Wennberg, P. O.: Atmospheric Fate of Methyl Vinyl Ketone: Peroxy Radical Reactions with NO and HO_2, J. Phys. Chem. A, 119, 4562-4572, doi:10.1021/jp5107058, 2015.

Ridley, B., Dye, J., Walega, J., Zheng, J., Grahek, F. and Rison, W.: On the production of active nitrogen by thunderstorms over New Mexico, J. Geophys. Res., 101, 20985-21005, doi:10.1029/96JD01706, 1996.

Rollins, A. W., Smith, J. D., Wilson, K. R. and Cohen, R. C.: Real Time In Situ Detection of Organic Nitrates in Atmospheric Aerosols, Environ. Sci. Technol., 44, 5540-5545, doi:10.1021/es100926x, 2010.

Romps, D. M., Seeley, J. T., Vollaro, D. and Molinari, J.: Climate change. Projected increase in lightning strikes in the United States due to global warming, Science, 346, 851-854, doi:10.1126/science.1259100, 2014.

Russell, A. R., Perring, A. E., Valin, L. C., Bucsela, E. J., Browne, E. C., Min, K., Wooldridge, P. J. and Cohen, R. C.: A high spatial resolution retrieval of NO_2 column densities from OMI: method and evaluation, Atmos. Chem. Phys., 11, 8543-8554, doi:10.5194/acp-11-8543-2011, 2011.

Ryerson, T., Huey, L., Knapp, K., Neuman, J., Parrish, D., Sueper, D. and Fehsenfeld, F.: Design and initial characterization of an inlet for gas-phase NO_y measurements from aircraft, J. Geophys. Res., 104, 5483-5492, doi:10.1029/1998JD100087, 1999.

Sachse, G. W., Hill, G. F., Wade, L. O. and Perry, M. G.: Fast-Response, High-Precision Carbon Monoxide Sensor using a Tunable Diode Laser Absorption Technique, J. Geophys. Res., 92, 2071-2081, doi:10.1029/JD092iD02p02071, 1987.

Sander, S. P. and Peterson, M. E.: Kinetics of the Reaction $HO_2 + NO_2 + M \rightarrow HO_2NO_2 + M$, J. Phys. Chem., 88, 1566-1571, doi:10.1021/j150652a025, 1984.

Sander, S. P., Abbatt, J. P. D., Barker, J. R., Burkholder, J. B., Friedl, R. R., Golden, D. M., Huie, R. E., Kolb, C. E., Kurylo, M. J., Moortgat, G. K., Orkin, V. L. and Wine, P. H.: Chemical Kinetics and Photochemical Data for Use in Atmospheric Studies, Evaluation No. 17, JPL Publication 10-6, Jet Propulsion Laboratory, Pasadena, 2011.

Santee, M. L., Lambert, A., Read, W. G., Livesey, N. J., Cofield, R. E., Cuddy, D. T., Daffer, W. H., Drouin, B. J., Froidevaux, L., Fuller, R. A., Jarnot, R. F., Knosp, B. W., Manney, G. L., Perun, V. S., Snyder, W. V., Stek, P. C., Thurstans, R. P., Wagner, P. A., Waters, J. W., Muscari, G., de Zafra, R. L., Dibb, J. E., Fahey, D. W., Popp, P. J., Marcy, T. P., Jucks, K. W., Toon, G. C., Stachnik, R. A., Bernath, P. F., Boone, C. D., Walker, K. A., Urban, J. and Murtagh, D.: Validation of the Aura Microwave Limb Sounder HNO_3 measurements, J. Geophys. Res., 112, D24S40, doi:10.1029/2007JD008721, 2007.

Saunders, S., Jenkin, M., Derwent, R. and Pilling, M.: Protocol for the development of the Master Chemical Mechanism, MCM v3 (Part A): tropospheric degradation of non-aromatic volatile organic compounds, Atmos. Chem. Phys., 3, 161-180, doi:10.5194/acp-3-161-2003, 2003.

Sauvage, B., Martin, R. V., van Donkelaar, A., Liu, X., Chance, K., Jaeglé, L., Palmer, P. I., Wu, S. and Fu, T. -.: Remote sensed and in situ constraints on processes affecting tropical tropospheric ozone, Atmos. Chem. Phys., 7, 815-838, doi:10.5194/acp-7-815-2007, 2007.

Schultz, M., Jacob, D., Wang, Y., Logan, J., Atlas, E., Blake, D., Blake, N., Bradshaw, J., Browell, E., Fenn, M., Flocke, F., Gregory, G., Heikes, B., Sachse, G., Sandholm, S., Shetter, R., Singh, H. and Talbot, R.: On the origin of tropospheric ozone and NO_x over the tropical South Pacific, J. Geophys. Res., 104, 5829-5843, doi:10.1029/98JD02309, 1999.

Schultz, M., Jacob, D., Bradshaw, J., Sandholm, S., Dibb, J., Talbot, R. and Singh, H.: Chemical NO_x budget in the upper troposphere over the tropical South Pacific, J. Geophys. Res., 105, 6669-6679, doi:10.1029/1999JD900994, 2000.

Schumann, U. and Huntrieser, H.: The global lightning-induced nitrogen oxides source, Atmos. Chem. Phys., 7, 3823-3907, doi:10.5194/acp-7-3823-2007, 2007.

Seltzer, K. M., Vizuete, W. and Henderson, B. H.: Evaluation of updated nitric acid chemistry on ozone precursors and radiative effects, Atmos. Chem. Phys., 15, 5973 - 5986, doi:10.5194/acp-15-5973-2015, 2015.

Shetter, R. E. and Müller, M.: Photolysis frequency measurements using actinic flux spectroradiometry during the PEM-Tropics mission: Instrumentation description and some results, J. Geophys. Res., 104, 5647-5661, doi:10.1029/98JD01381, 1999.

Singh, H., Salas, L., Chatfield, R., Czech, E., Fried, A., Walega, J., Evans, M., Field, B., Jacob, D., Blake, D., Heikes, B., Talbot, R., Sachse, G., Crawford, J., Avery, M., Sandholm, S. and Fuelberg, H.: Analysis of the atmospheric distribution, sources, and sinks of oxygenated volatile organic chemicals based on measurements over the Pacific during TRACE-P, J. Geophys. Res., 109, D15S07, doi:10.1029/2003JD003883, 2004.

Slusher, D. L., Huey, L. G., Tanner, D. J., Flocke, F. M. and Roberts, J. M.: A thermal dissociation-chemical ionization mass spectrometry (TD-CIMS) technique for the simultaneous measurement of peroxyacyl nitrates and dinitrogen pentoxide, J. Geophys. Res., 109, D19315, doi:10.1029/2004JD004670, 2004.

Søvde, O. A., Hoyle, C. R., Myhre, G. and Isaksen, I. S. A.: The HNO_3 forming branch of the HO_2 + NO reaction: pre-industrial-to-present trends in atmospheric species and radiative forcings, Atmos. Chem. Phys., 11, 8929-8943, doi:10.5194/acp-11-8929-2011, 2011.

Spencer, K. M., McCabe, D. C., Crounse, J. D., Olson, J. R., Crawford, J. H., Weinheimer, A. J., Knapp, D. J., Montzka, D. D., Cantrell, C. A., Hornbrook, R. S., Mauldin,R.L.,,III and Wennberg, P. O.: Inferring ozone production in an urban atmosphere using measurements of peroxynitric acid, Atmos. Chem. Phys., 9, 3697-3707, doi:10.5194/acp-9-3697-2009, 2009.

Sprengnether, M. M., Demerjian, K. L., Dransfield, T. J., Clarke, J. S., Anderson, J. G. and Donahue, N. M.: Rate Constants of Nine C6-C9 Alkanes with OH from 230 to 379 K: Chemical Tracers for [OH], J. Phys. Chem. A, 113, 5030-5038, doi:10.1021/jp810412m, 2009.

St. Clair, J. M., McCabe, D. C., Crounse, J. D., Steiner, U. and Wennberg, P. O.: Chemical ionization tandem mass spectrometer for the in situ measurement of methyl hydrogen peroxide, Rev. Sci. Instrum., 81, 094102, doi:10.1063/1.3480552, 2010.

Stavrakou, T., Müller, J. -., Boersma, K. F., van, d. A., Kurokawa, J., Ohara, T. and Zhang, Q.: Key chemical NO_x sink uncertainties and how they influence top-down emissions of nitrogen oxides, Atmos. Chem. Phys., 13, 9057-9082, doi:10.5194/acp-13-9057-2013, 2013.

Talbot, R., Dibb, J., Lefer, B., Scheuer, E., Bradshaw, J., Sandholm, S., Smyth, S., Blake, D., Blake, N., Sachse, G., Collins, J. and Gregory, G.: Large-scale distributions of tropospheric nitric, formic, and acetic acids over the western Pacific basin during wintertime, J. Geophys. Res., 102, 28303-28313, doi:10.1029/96JD02975, 1997.

Teng, A. P., Crounse, J. D., Lee, L., St Clair, J. M., Cohen, R. C. and Wennberg, P. O.: Hydroxy nitrate production in the OH-initiated oxidation of alkenes, Atmos. Chem. Phys., 15, 4297-4316, doi:10.5194/acp-15-4297-2015, 2015.

Thornton, J. A., Wooldridge, P. J. and Cohen, R. C.: Atmospheric NO_2: In situ laser-induced fluorescence detection at parts per trillion mixing ratios, Anal. Chem., 72, 528-539, doi:10.1021/ac9908905, 2000.

Tyndall, G., Cox, R., Granier, C., Lesclaux, R., Moortgat, G., Pilling, M., Ravishankara, A. and Wallington, T.: Atmospheric chemistry of small organic peroxy radicals, J. Geophys. Res., 106, 12157-12182, doi:10.1029/2000JD900746, 2001.

Wagner, N. L., Riedel, T. P., Young, C. J., Bahreini, R., Brock, C. A., Dubé, W. P., Kim, S., Middlebrook, A. M., Özturk, F., Roberts, J. M., Russo, R., Sive, B., Swarthout, R., Thornton, J. A., VandenBoer, T. C., Zhou, Y. and Brown, S. S.: N_2O_5 uptake coefficients and nocturnal NO_2 removal rates determined from ambient wintertime measurements, J. Geophys. Res., 118, 9331-9350, doi:10.1002/jgrd.50653, 2013.

Wennberg, P., Salawitch, R., Donaldson, D., Hanisco, T., Lanzendorf, E., Perkins, K., Lloyd, S., Vaida, V., Gao, R., Hintsa, E., Cohen, R., Swartz, W., Kusterer, T. and Anderson, D.: Twilight observations suggest unknown sources of HOx, Geophys. Res. Lett., 26, 1373-1376, doi:10.1029/1999GL900255, 1999.

Wilson, E., Hamilton, W., Kennington, H., Evans, B., Scott, N. and DeMore, W.: Measurement and estimation of rate constants for the reactions of hydroxyl radical with several alkanes and cycloalkanes, J. Phys. Chem. A, 110, 3593-3604, doi:10.1021/jp055841c, 2006.

Wisthaler, A., Hansel, A., Dickerson, R. R. and Crutzen, P. J.: Organic trace gas measurements by PTR-MS during INDOEX 1999, J. Geophys. Res., 107, 8024, doi:10.1029/2001JD000576, 2002.

Wolff, M. A., Kerzenmacher, T., Strong, K., Walker, K. A., Toohey, M., Dupuy, E., Bernath, P. F., Boone, C. D., Brohede, S., Catoire, V., von Clarmann, T., Coffey, M., Daffer, W. H., De Maziere, M., Duchatelet, P., Glatthor, N., Griffith, D. W. T., Hannigan, J., Hase, F., Hoepfner, M., Huret, N., Jones, N., Jucks, K., Kagawa, A., Kasai, Y., Kramer, I., Kuellmann, H., Kuttippurath, J., Mahieu, E., Manney, G., McElroy, C. T., McLinden, C., Mebarki, Y., Mikuteit, S., Murtagh, D., Piccolo, C., Raspollini, P., Ridolfi, M., Ruhnke, R., Santee, M., Senten, C., Smale, D., Tetard, C., Urban, J. and Wood, S.: Validation of HNO_3, $ClONO_2$, and N_2O_5 from the Atmospheric Chemistry Experiment Fourier Transform Spectrometer (ACE-FTS), Atmos. Chem. Phys., 8, 3529-3562, doi:10.5194/acp-8-3529-2008, 2008.

Wooldridge, P. J., Perring, A. E., Bertram, T. H., Flocke, F. M., Roberts, J. M., Singh, H. B., Huey, L. G., Thornton, J. A., Wolfe, G. M., Murphy, J. G., Fry, J. L., Rollins, A. W., LaFranchi, B. W. and Cohen, R. C.: Total Peroxy Nitrates (ΣPNs) in the atmosphere: the Thermal Dissociation-Laser Induced Fluorescence (TD-LIF) technique and comparisons to speciated PAN measurements, Atmos. Meas. Tech., 3, 593-607, doi:10.5194/amt-3-593-2010, 2010.

Appendix A. Observational Constraints on the Oxidation of NO_x in the Upper Troposphere

A.1 Measurement Intercomparisons

During DC3, the NASA DC-8 payload included measurements of speciated ($CH_3O_2NO_2$, HO_2NO_2, PAN, and PPN) and total peroxy nitrates, gas-phase, and gas- and particle-phase HNO_3, allowing for intercomparions of the total peroxy nitrates and $HNO_{3(g+p)}$ for the entire mission. Also, the NSF National Center for Atmospheric Research GV and DC-8 conducted 5 wing tip-to-wing tip intercomparisons, allowing comparison of two HO_2NO_2 measurements. The results are shown in Figure A1. Finally, the DC-8 payload included measurements of temperature, pressure, NO_2 photolysis rate, HO_2, and O_3 (Table 3.1). These measurements are used to calculate photostationary steady state (PSS) NO_2 (E1) to compare against measured NO_2 (Fig. A2). The PSS NO_2 is calculated for observations where $NO_x/NO_y < 0.4$ (removes emissions), solar zenith angle < 80° (removes nighttime observations), $O_3/CO < 1.25$ (removes stratospheric intrusion), and at all temperatures due to the lack of observations meeting these criteria in the upper troposphere. We assumed that $[RO_2] \approx [HO_2]$. The rate constants are from Sander et al. (2011).

(E1) $$\left[NO_{2,PSS}\right] = \frac{k_{NO+O_3}[O_3][NO]+2\cdot k_{NO+HO_2}[HO_2][NO]}{j_{NO_2}}$$

The difference between the two HO_2NO_2 measurements is 35%. We scale the DC-8 observations to the average of the two measurements. For the peroxy nitrates, the difference between the speciated sum and total peroxy nitrates is 4%. There is a 10% difference between the two $HNO_{3(g+p)}$ measurements. We take the average of the two measurements as the $HNO_{3(g+p)}$.

A.2 Calculation of Alkyl and Multifunctional Nitrate

To calculate the speciated ΣANs production, we use 15 minute averaged observations of the hydrocarbons. The hydrocarbons, OH rate constants, and α are listed in Table A4. We also include the fraction of time the peroxy radical reacts with NO versus other species (~80%) in the calculation of the speciated ΣANs production. The α also includes any contribution from secondary organic nitrate formation after radical isomerization (e.g., Lee et al., 2014a). For hydrocarbons at or near the limit of detection (indicated in Table A4), we take the median mixing ratio observed during Leg 2 and calculate what the concentration should be in Leg 3, using the median OH concentration during Leg 2 (2.5×10^6 molecules/cm^3) and the time between sampling Leg 2 and Leg 3 (~ 4000 s). Then, we use that calculated mixing ratio as the initial mixing ratio for the rest of the flight. For the hydrocarbons that do not have a temperature dependent rate constant reported (i.e., methylhexane), we use a temperature dependent rate constant that has a similar value at 298 K. Finally, for isoprene nitrate, we use the branching ratios for the different peroxy radicals from Paulot et al. (2009) and we use the recommended rate constants and mechanism from Lee et al. (2014b) to produce other isoprene nitrate species (i.e., isoprene dinitrate, ethanal nitrate, etc.) from the first generation isoprene nitrates.

A.3 Calculation of Alkyl and Multifunctional Nitrate in Aerosol-Phase

Here are the following definitions for the values used in E4 – E5 in Chapter 3 to calculate the partitioning into aerosol. R is the gas constant (8.206×10^{-5} atm m^3 K^{-1} mol^{-1}), T is temperature (225 K), f_{om} is the weight fraction of organic material in the total aerosol (0.8 for this experiment), MW_{om} is the molecular weight of the absorbing organic material (assumed to be 180 g/mol), ζ is the activity coefficient of the compound of interest in the condensed phase (assumed to be 1 for this experiment), p_{vap} is the subcooled vapor pressure of interest (atm), 10^6 (μg/g) is a conversion factor, m_{om} is the mass of the background organic aerosol (ranged from 0.015 – 0.030 μg/m^3 at ambient T and P), and $m_{AN_{i,g}}$ and $m_{AN_{i,p}}$ are the masses of the speciated alkyl and multifunctional nitrates in the gas- and particle-phase, respectively. The units of K_p are m^3 μg^{-1}.

A.4 Description of GEOS-Chem Model

GEOS-Chem version 09-02b (Bey et al., 2001, http://geos-chem.org) is used at 2×2.5 degree resolution. The standard chemistry is described by Mao et al. (2013) and includes $CH_3O_2NO_2$ chemistry as recommended by Browne et al. (2011). Two separate runs were conducted: one with current recommendations (Sander et al., 2011; Mao et al., 2013, Base Case) and one with the slower recommendations (Bacak et al., 2011; Henderson et al., 2012, Updated Chemistry Case) for the HNO_3 and HO_2NO_2 production rate constant. Both models were run from January 2011 to December 2012, and only results from January – December 2012 are analyzed to minimize memory from the initialization of the model. We use the output between 200 – 400 hPa (upper troposphere) and remove output defined as being above the meteorological tropopause.

Table A1. Reactions and rate constants at T = 225 K and P = 230 hPa used to calculate PAN production rate and $CH_3C(O)O_2$ concentrations.

Reaction	Rate Constant (cm^3/molecules/s)
$CH_3C(O)OOH + OH \rightarrow CH_3C(O)O_2 + H_2O$	9.2×10^{-12}[a]
$CH_3C(O)H + OH + O_2 \rightarrow CH_3C(O)O_2 + H_2O$	2.2×10^{-11}[b]
$CH_3C(O)O_2 + HO_2 \rightarrow$ Products	4.4×10^{-11}[b]
$CH_3C(O)CH_3 + h\nu + O_2 \rightarrow CH_3C(O)O_2 + CH_3O_2$	Measured
$CH_3C(O)CH_3 + OH \xrightarrow{80\%} CH_3C(O)O_2 +$ products	1.4×10^{-13}[a]
$CH_2CHC(O)CH_3 + h\nu \rightarrow CH_3C(O)O_2 +$ products	Assumed same as methyl vinyl ketone photolysis[c]
$CH_2CHC(O)CH_3 + OH \xrightarrow{60\%} CH_3C(O)O_2 +$ products	3.9×10^{-11}[b,c,d]
$CH_2C(CH_2)C(O)H + h\nu \xrightarrow{35\%} CH_3C(O)O_2 +$ products	Assumed same as butanal photolysis[c,d]
$CH_2C(CH_2)C(O)H + h\nu \xrightarrow{30\%} CH_3C(O)O_2 +$ products	Assumed same as butanal photolysis[c,d]
$CH_2C(CH_2)C(O)H + OH \xrightarrow{15\%} CH_3C(O)O_2 +$ products	4.3×10^{-11}[b,c,d]
$CH_3C(O)CH_2OH + h\nu \rightarrow CH_3C(O)O_2 +$ products	Assumed same as acetone photolysis[c]
$CH_3C(O)O_2 + NO \rightarrow CH_3O_2 + CO_2 + NO_2$	2.7×10^{-11}[a]
$C_2H_5C(O)CH_3 + h\nu \rightarrow CH_3C(O)O_2 +$ products	Measured

[a]Sander et al. (2011)
[b]Atkinson et al. (2006)
[c]We assumed that 40% of MACR+MVK measurements from the PTR-MS is MACR and 60% is MVK.
[d]The percent over the arrow includes the branching between reacting with NO, HO_2, and NO_2.

Table A2. Reactions and rate constants used to calculate PPN production rate and $C_2H_5C(O)O_2$ concentrations.

Reaction	Rate Constant (cm^3/molecules/s)
$C_2H_5CHO + OH + O_2 \rightarrow C_2H_5C(O)O_2 + H_2O$	3.0×10^{-11} [a]
$C_2H_5C(O)O_2 + HO_2 \rightarrow$ Products	4.4×10^{-11} [b]
$C_2H_5C(O)O_2 + NO \rightarrow CH_3O_2 + CO_2 + NO_2$	2.7×10^{-11} [b]

[a] Atkinson et al. (2006).
[b] Sander et al. (2011).

Table A3. Reactions and rate constants used to calculate $CH_3O_2NO_2$ production rate and CH_3O_2 concentrations.

Reaction	Rate Constant (cm^3/molecules/s)
$CH_4 + OH + O_2 \rightarrow CH_3O_2 + H_2O$	9.2×10^{-16}[a]
$CH_3C(O)O_2 + NO \rightarrow CH_3O_2 + CO_2 + NO_2$	2.7×10^{-11}[a]
$CH_3C(O)CH_3 + h\nu + O_2 \rightarrow CH_3C(O)O_2 + CH_3O_2$	Measured
$CH_3OOH + OH \xrightarrow{70\%} CH_3O_2 + H_2O$	9.2×10^{-12}[a]
$CH_3C(O)OH + h\nu + O_2 \rightarrow CH_3O_2 + HCO$	Measured
$CH_3O_2 + NO \rightarrow CH_3O + NO_2$	1.1×10^{-11}[a]
$CH_3O_2 + HO_2 \rightarrow$ Products	1.1×10^{-11}[a]
$CH_3C(O)OOH + h\nu \rightarrow CH_3O_2 +$ product	Assumed same as methyl hydrogen peroxide
$CH_3C(O)O_2 + HO_2 \xrightarrow{45\%} CH_3O_2 + OH +$ product	4.4×10^{-11}[a]

[a]Sander et al. (2011).

Table A4. Species, rate constants, average α, and classification used to calculate alkyl nitrate production (E2 in Chapter 3 and Fig. 3.8b) at T = 225 K and P = 230 hPa.

Parent Compound	Rate constant (cm^3/molecules/s)	Initial Concentration (pptv)	α	Classification in Fig. 3.8b
Alkanes				
Methane	9.2×10^{-16}[d]	1.85×10^{6}	0.0014	ΣANs < C6
Ethane	8.1×10^{-14}[e]	1880	0.0036	ΣANs < C6
Propane	5.7×10^{-13}[e]	880	0.0189	ΣANs < C6
i-Butane	1.6×10^{-12}[e]	136	0.0479	ΣANs < C6
n-Butane	1.5×10^{-12}[e]	308	0.0426	ΣANs < C6
i-Pentane	2.6×10^{-12}[f]	85	0.0535	ΣANs < C6
n-Pentane	2.8×10^{-12}[g]	71	0.1436	ΣANs < C6
Cyclopentane	3.6×10^{-12}[g]	6	0.1030	ΣANs < C6
2-Methylpentane	4.9×10^{-12}[h]	10	0.1821	ΣANs ≥ C6
3-Methylpentane	4.9×10^{-12}[h]	9	0.1354	ΣANs ≥ C6
n-Hexane	4.9×10^{-12}[g]	8	0.4486	ΣANs ≥ C6
Methyl Cyclopentane[a]	6.9×10^{-12}[i]	9	0.1937	ΣANs ≥ C6
Cyclohexane[a]	5.3×10^{-12}[g]	12	0.2096	ΣANs ≥ C6
2,3-Dimethylbutane[a]	5.6×10^{-12}[g]	4	0.0735	ΣANs ≥ C6
n-Heptane[a]	6.7×10^{-12}[g]	12	0.5052	ΣANs ≥ C6
2-Methylhexane[a]	6.7×10^{-12}[j]	7.5	0.3933	ΣANs ≥ C6
3-Methylhexane[a]	6.7×10^{-12}[j]	21	0.4003	ΣANs ≥ C6
2,4-Dimethylpentane[a]	2.6×10^{-12}[k]	4	0.3134	ΣANs ≥ C6
2,3-Dimethylpentane[a]	2.6×10^{-12}[k]	6	0.3134	ΣANs ≥ C6
2,2,4-Trimethylpentane[a]	2.6×10^{-12}[k]	11	0.3134	ΣANs ≥ C6
Alkenes				
Ethene	8.9×10^{-12}[e]	34	0.0068[m]	ΣANs < C6
Isoprene[a]	1.5×10^{-10}[e]	15	0.1135	ΣANs Isoprene
α-Pinene[a]	8.5×10^{-11}[e]	10	0.4991	ΣANs Monoterpenes
OVOCs				
Acetone	1.4×10^{-13}[d]	1490	0.0091	ΣANs OVOC
MVK[b]	3.9×10^{-11}[l]	39	0.0184[n]	ΣANs OVOC
MACR[b,c]	4.3×10^{-11}[l]	26	0.0113	ΣANs OVOC
Aromatics				
Benzene	9.9×10^{-13}[l]	33	0.0063[o]	ΣANs Aromatic
Toluene	8.2×10^{-12}[l]	21	0.0052[o]	ΣANs Aromatic
C8 Aromatics	1.6×10^{-11}[l]	8	0.0700[o]	ΣANs Aromatic

[a]Measurements at or near limit of detection. Calculated the initial concentration using observations from Leg 2.

[b]We assumed that 40% of MACR+MVK measurements from the PTR-MS is MACR and 60% is MVK.
[c]We assumed the reaction of $MACRO_2$ with NO is faster than isomerization (~0.04 s^{-1} versus 0.005 s^{-1}); therefore, it will produce 2 multifunctional nitrates (Crounse et al., 2012).
[d]Sander et al. (2011)
[e]Atkinson et al. (2006)
[f]Wilson et al. (2006)
[g]Atkinson (2003)
[h]Assumed same as n-hexane
[i]Sprengnether et al. (2009)
[j]Assumed same as n-heptane
[k]Assumed same as i-pentane
[l]Saunders et al. (2003)
[m]Scaled to Teng et al. (2015).
[n]Scaled to Praske et al. (2015).
[o]Scaled to Perring et al. (2013).

Table A5. Species, corrected vapor pressure (atm), percent of gas–phase condensing onto the aerosol particle, and percent contribution of each species to the total calculated $\Sigma ANs_{(p)}$. The vapor pressure is calculated using SIMPOL.1 (Pankow and Asher, 2008) and divided by 3 (Leungsakul et al., 2005; Fry et al., 2009; Fry et al., 2011).

Parent Compound	Corrected Vapor Pressure (atm)	% Gas–Phase Condensing onto Aerosol Particle	% Contribution to Calculated $\Sigma ANs_{(p)}$
Alkanes			
Methane	5.2×10^{-4}	< 1	< 1
Ethane	9.7×10^{-5}	< 1	< 1
Propane	1.8×10^{-5}	< 1	< 1
i-Butane	3.3×10^{-6}	< 1	< 1
n-Butane	3.3×10^{-6}	< 1	< 1
i-Pentane 1st Generation	6.2×10^{-7}	< 1	< 1
i-Pentane 2nd Generation	5.1×10^{-10}	< 1	< 1
n-Pentane 1st Generation	6.2×10^{-7}	< 1	< 1
n-Pentane 2nd Generation	5.1×10^{-10}	< 1	< 1
Cyclopentane 1st Generation	1.2×10^{-5}	< 1	< 1
Cyclopentane 2nd Generation	7.0×10^{-9}	< 1	< 1
2-Methylpentane 1st Generation	1.2×10^{-7}	< 1	< 1
2-Methylpentane 2nd Generation	9.4×10^{-11}	4	< 1
3-Methylpentane 1st Generation	1.2×10^{-7}	< 1	< 1
3-Methylpentane 2nd Generation	9.4×10^{-11}	4	< 1
n-Hexane 1st Generation	1.2×10^{-7}	< 1	< 1
n-Hexane 2nd Generation	9.4×10^{-11}	4	3
Methyl Cyclopentane	4.0×10^{-7}	< 1	< 1
Cyclohexane 1st Generation	2.1×10^{-6}	< 1	< 1
Cyclohexane 2nd Generation	1.3×10^{-9}	< 1	< 1
2,3-Dimethylbutane	1.2×10^{-7}	< 1	< 1
n-Heptane 1st Generation	2.2×10^{-8}	< 1	< 1
n-Heptane 2nd Generation	1.8×10^{-11}	24	19
2-Methylhexane 1st Generation	2.2×10^{-8}	< 1	< 1
2-Methylhexane 2nd Generation	1.8×10^{-11}	24	19
3-Methylhexane 1st Generation	2.2×10^{-8}	< 1	< 1
3-Methylhexane 2nd Generation	1.8×10^{-11}	24	19
2,4-Dimethylpentane	2.2×10^{-8}	< 1	< 1
2,3-Dimethylpentane	2.2×10^{-8}	< 1	< 1
2,2,4-Trimethylpentane	4.0×10^{-9}	< 1	< 1

Table A5. Continued. Species, corrected vapor pressure (atm), percent of gas–phase condensing onto the aerosol particle, and percent contribution of each species to the total calculated $\Sigma ANs_{(p)}$. The vapor pressure is calculated using SIMPOL.1 (Pankow and Asher, 2008) and divided by 3 (Leungsakul et al., 2005; Fry et al., 2009; Fry et al., 2011).

Parent Compound	Corrected Vapor Pressure (atm)	% Gas–Phase Condensing onto Aerosol Particle	% Contribution to Calculated $\Sigma ANs_{(p)}$
Alkenes			
Ethene	7.8×10^{-8}	< 1	< 1
Isoprene 1st Generation	4.4×10^{-10}	< 1	< 1
Isoprene 2nd Generation	3.7×10^{-16}	100	9
α-Pinene 2 Rings	3.9×10^{-11}	6	26
α-Pinene 1 Ring	1.8×10^{-12}	100	3
OVOCs			
Acetone	2.2×10^{-6}	< 1	< 1
MVK	4.1×10^{-7}	< 1	< 1
MACR	4.1×10^{-7}	< 1	< 1
Aromatics			
Benzene	2.9×10^{-8}	< 1	< 1
Toluene	3.7×10^{-9}	< 1	< 1
C8 Aromatics	6.7×10^{-10}	< 1	< 1

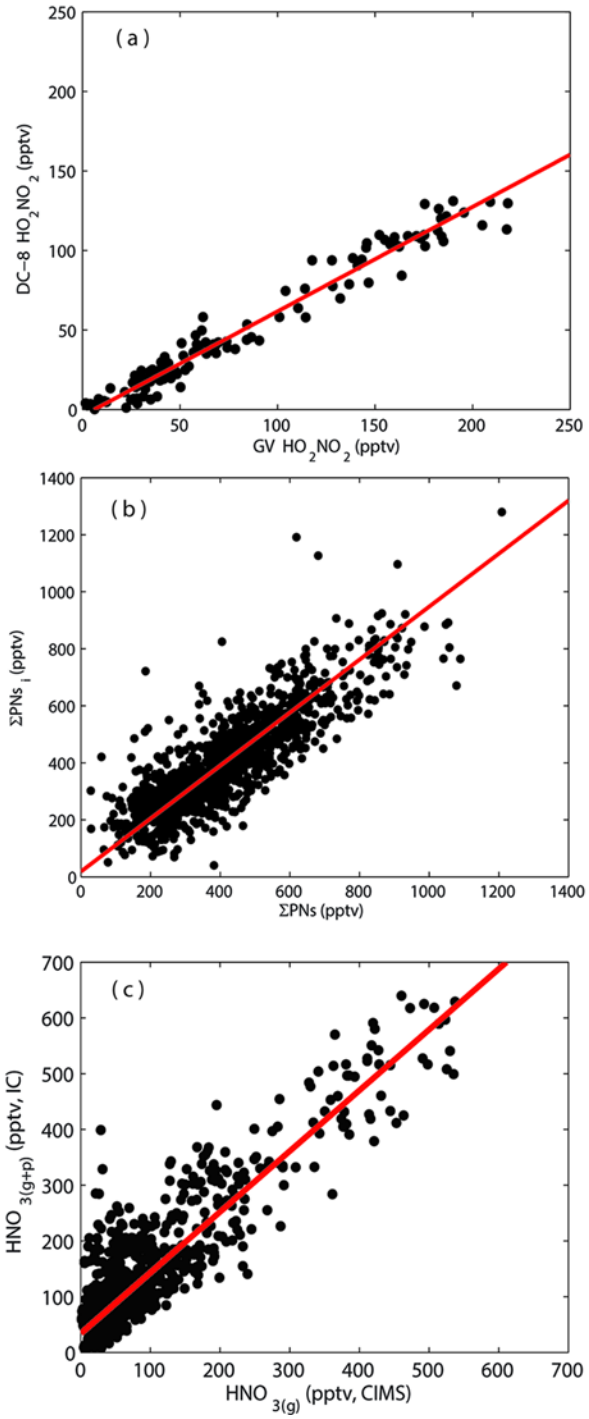

Figure A1. Intercomparison of **(a)** DC-8 versus GV HO_2NO_2, **(b)** ΣPNs_i (ΣPNs_i = $CH_3O_2NO_2$ + HO_2NO_2 + PAN + PPN) versus ΣPNs, and **(c)** IC $HNO_{3(p+g)}$ versus CIMS $HNO_{3(g)}$. The slopes (±1σ), intercepts (±1σ), and R^2 values are **(a)** 0.66(±0.01), −3(±1), and 0.96, **(b)** 0.96(±0.02), 7(±9), and 0.68, and **(c)** 1.09(±0.02), 34(±2), and 0.81.

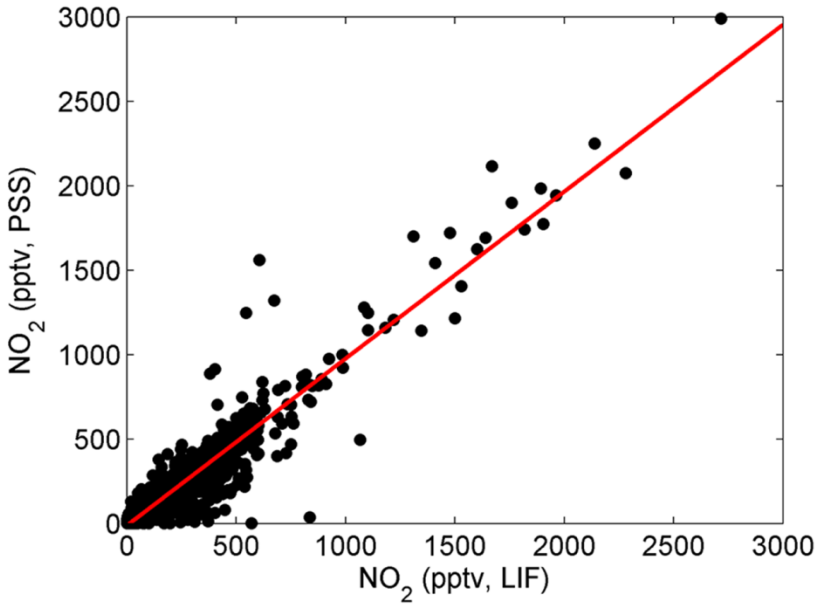

Figure A2. Intercomparison of photostationary steady state (PSS) NO_2 versus measured NO_2. The slope (±1σ), intercept (±1σ), and R^2 is 0.99(±0.01), −12(±2), and 0.89.

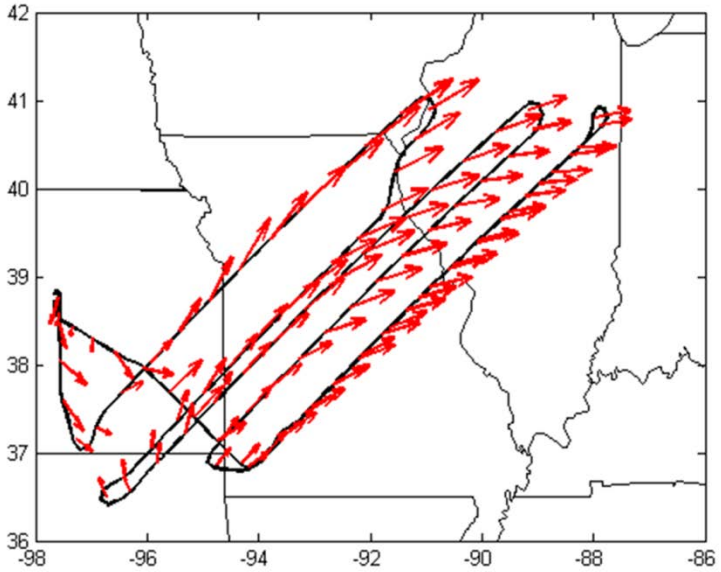

Figure A3. The full flight path of the NASA DC-8 is shown in black for the entire 21 June 2012 experiment. Wind direction and relative speed observed on the DC-8 is shown by the red arrows.

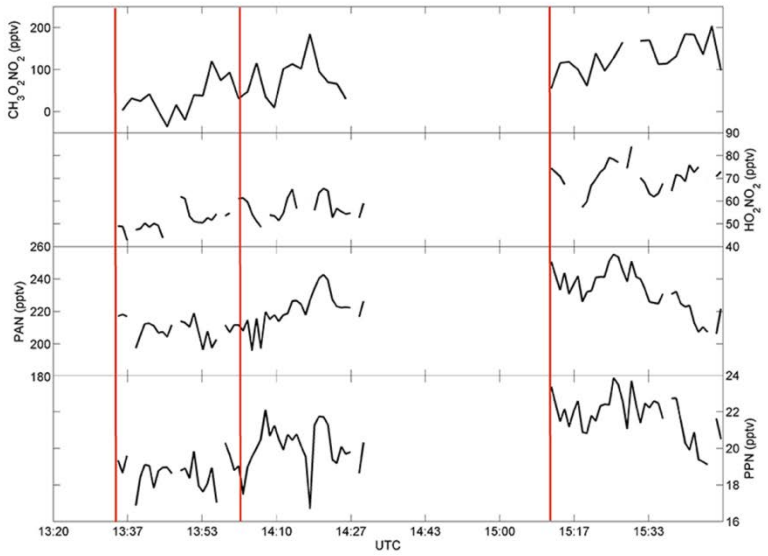

Figure A4. Time series of **(a)** $CH_3O_2NO_2$, **(b)** HO_2NO_2, **(c)** PAN, and **(d)** PPN. The red vertical lines indicate the start of legs 1, 2, and 3, respectively in Fig. 3.2. The $CH_3O_2NO_2$ observations are three minute averages and the values.

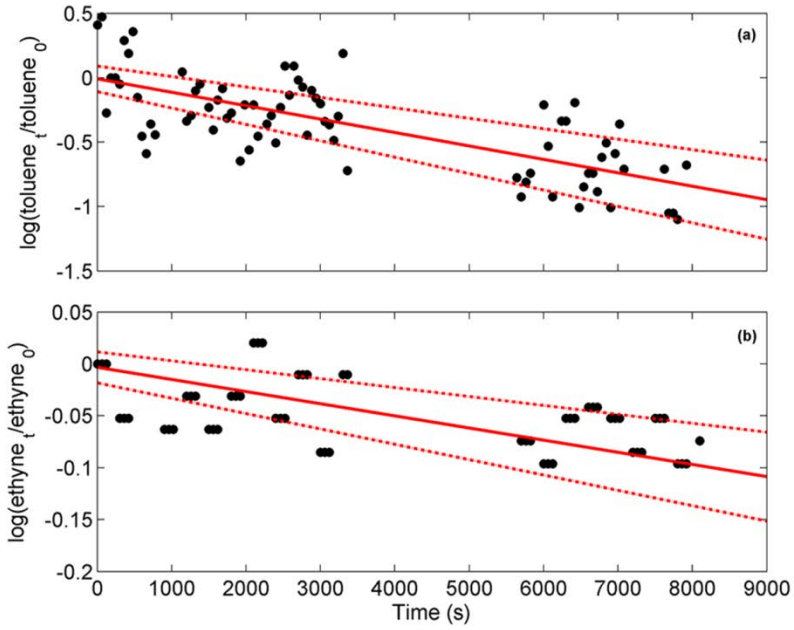

Figure A5. First order loss rate of **(a)** toluene and **(b)** ethyne. The solid red line is the slope (-1.01×10^{-4} and -5.9×10^{-6} s^{-1} for toluene and ethyne, respectively) and the dashed-dot red line is the 2σ uncertainty ($\pm2.3\times10^{-5}$ and $\pm2.6\times10^{-6}$ s^{-1} for toluene and ethyne, respectively).